DYNAMICS OF INTERACTING ULTRACOLD ATOMS AND EMERGENT QUANTUM STATES

by

Changyuan Lyu

A Dissertation

Submitted to the Faculty of Purdue University

In Partial Fulfillment of the Requirements for the degree of

Doctor of Philosophy

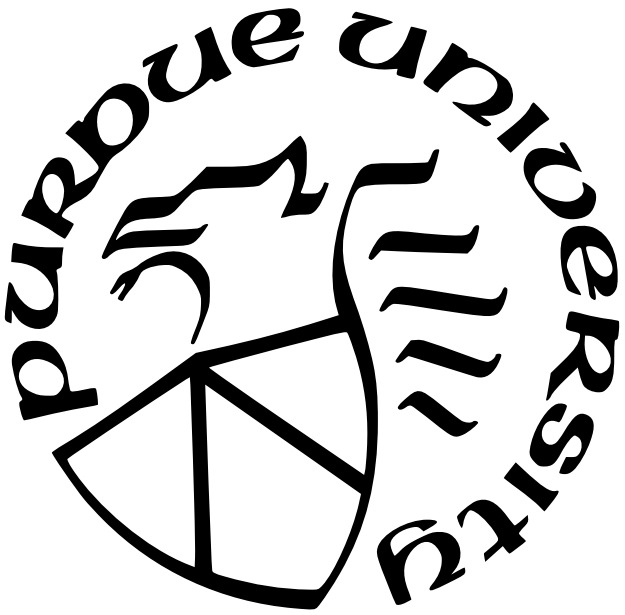

Department of Physics and Astronomy

West Lafayette, Indiana

May 2021

THE PURDUE UNIVERSITY GRADUATE SCHOOL
STATEMENT OF COMMITTEE APPROVAL

Dr. Qi Zhou, Chair

Department of Physics and Astronomy

Dr. Christopher H. Greene

Department of Physics and Astronomy

Dr. Chen-Lung Hung

Department of Physics and Astronomy

Dr. Sergei Khlebnikov

Department of Physics and Astronomy

Approved by:

Dr. John P. Finly

To my dear aunt, Lanfang Lyu

ACKNOWLEDGMENTS

I would like to express my deepest gratitude to my advisor, Professor Qi Zhou, for his guidance on both my Ph.D. studies and career development. He taught me physics knowledge patiently and provided me with rich opportunities for attending workshops and interacting with other researchers. More importantly, the wisdom I learned from him, including the method for understanding a new thing and the strategy for attacking a difficult problem, will benefit me for a lifetime. Even in the future after I have left physics research, I will still remember his words, "take one step back", whenever I do not know how to proceed with a hard task.

My appreciation also goes to the committee members, Professor Chris Greene, Professor Chen-Lung Hung, and Professor Sergei Khlebnikov, for the fruitful discussions and their instructions on physics courses, which are indispensable for me to complete the thesis.

Thank you to my amazing colleagues, Chenwei Lv, Yangqian Yan, and Sayan Choudhury, as well as Professor Ren Zhang. The collaborations with them deepened my understandings of many sub-fields of physics and math. Their valuable feedback during my group meeting presentations helped me increase communication skills. The lively office conversations also made me relaxed and accompanied.

Thanks to my parents for their supports and understandings during the years. Thanks to my warm-hearted friends, Xiao Wang, Zhujing Xu, Lingyi Dong, Troy Seberson, Guo Li, Tobi Busari, Zixun Yu, Tianyu Li, Chao Guo, and Tianyu Wang, who make me feel no longer lonely in this journey. Thanks to Purdue University and the Department of Physics and Astronomy for offering me the opportunity to pursue my Ph.D. degree.

Research projects in this thesis are financially supported by Purdue Research Foundation, Purdue Quantum Science and Engineering Institute, W. M. Keck Foundation, F. N. Andrews Fellowship from Purdue University Graduate School, U.S. DOE Grant No. DE-SC0019202, and NSF Grant No. 1806796.

TABLE OF CONTENTS

LIST OF TABLES

LIST OF FIGURES

ABBREVIATIONS

BEC	Bose-Einstein condensate
DQPT	dynamical quantum phase transition
DTC	discrete time crystal
OTOC	out-of-time-order correlator
MBL	many body localization
FWHM	full width at half maximum

ABSTRACT

The development of ultracold atom physics enables people to study fundamental questions in quantum mechanics within this highly-tunable platform. This dissertation focuses on several topics of the dynamical evolution of quantum systems.

Chapter 2 and 3 talk about Loschmidt echo, a simple quantity that reveals many hidden properties of a system's time evolution. Chapter 2 looks for vanishing Loschmidt echo in the complex plane of time and the corresponding dynamical quantum phase transitions (DQPT) in the thermodynamic limit. For a two-site Bose-Hubbard model consisting of weakly interacting particles, DQPTs reside at the time scale inversely proportional to the interaction, where highly entangled pair condensates also show up. Chapter 3 discusses the revival of Loschmidt echo in a discrete time crystal, a Floquet system whose discrete temporal transition symmetry is spontaneously broken. We propose a new design and demonstrate its robustness against the fluctuations in the driving field. It can also be used in precision measurement to go beyond the Heisenberg limit. Experimental schemes are presented.

Out-of-time-order correlator (OTOC) is a more complicated variant of Loschmidt echo. Experimentally it requires reversing the time evolution. In Chapter 4, by exploiting the SU(1,1) symmetry of a weakly interacting BEC and connecting its quantum dynamics to a hyperbolic space, we obtain a geometric framework that enables experimentalists to manipulate the evolution with great freedom. Backward evolution is then realized effectively to measure OTOC of such SU(1,1) systems.

Chapter 5 discusses the decoherence of a spin impurity immersed in a spinor BEC. Our calculations show that by looking at the dynamics of the impurity's reduced density matrix, the phase of the spinor BEC can be detected.

1. INTRODUCTION

In non-relativistic quantum mechanics, Schrödinger's equation determines the dynamical evolution of a physical system. For a closed system, the system's Hamiltonian is time-independent. The initial state of a system can be eigen-decomposed to linear superposition of eigenstates of the Hamiltonian. As time goes on, every component gets a phase factor. Namely, for any initial state $|\psi_0\rangle$, it evolves as

$$|\psi(t)\rangle = \sum_n c_n e^{-iE_n t} |\varphi_n\rangle \,, \tag{1.1}$$

where E_n and $|\varphi_n\rangle$ are eigenvalues and eigenstates of the Hamiltonian respectively and $c_n = \langle\varphi_n|\psi_0\rangle$. Although this basic law looks simple, it is much more complicated to theoretically predict the behaviors of realistic physical systems' quantum dynamics. The first challenge is to have an appropriate model to write down the Hamiltonian. The interactions between different constituents make the calculations more difficult. The dimension of the total Hilbert space grows exponentially as the number of particles in a system increases, which makes brute-force numerical simulations impractical.

Ultracold atoms uploaded into optical lattices have provided a quantum simulator for physicists to solve the problem. The periodic potential created by lasers is clean and free of defects. Its single-atom energy spectrum can be computed exactly. Also, the inter-atom interaction, characterized by the scattering length a_s, can be measured accurately and tuned with great freedom by Feshbach resonance [1]. Experimentalists can change the intensity, the frequency, and the spatial layout of the laser beams. Thus it is possible to realize a lot of models from bottom to top. Technique advances, such as optical tweezers [2–4] and single-site fluorescence imaging [5, 6], also make manipulating and tracking single atoms feasible. This dissertation is a theoretical study of several models that are within the current ultracold atom experiments' reach. The following sections give a brief background of these topics.

1.1 Bose-Einstein Condensates

For a non-interacting Bose gas in a uniform 3D space with total particle number N, volume V, and single particle mass M, once the temperature is below a critical value T_0,

$$T_0 = \frac{2\pi\hbar^2}{k_B\zeta(\frac{3}{2})^{\frac{2}{3}}M}\left(\frac{N}{V}\right)^{\frac{2}{3}}, \tag{1.2}$$

where ζ is the Riemann zeta function, a fraction of bosons

$$\frac{N_0}{N} = 1 - \left(\frac{T}{T_0}\right)^{\frac{3}{2}} \tag{1.3}$$

will be condensed to the ground state. This state of matter is called Bose-Einstein condensate (BEC), first predicted by A. Einstein in 1924 following the Bose statistics proposed by S. N. Bose.

For non-interacting Bose gases, BECs show up when a macroscopic number (proportional to the total particle number) of bosons occupy the lowest single particle energy level, which is not well defined when interactions present. Generally a BEC is identified through the reduced single-particle density matrix ρ_1 [7], whose element at row i and column j is

$$\rho_{1,ij} = \mathrm{Tr}\Big(\rho a_i^\dagger a_j\Big), \tag{1.4}$$

where ρ is the total density matrix and $a_i^\dagger$ and a_i are the creation and annihilation operators of single particle basis state i. Its off-diagonal term $\rho_{1,i\neq j}$ is called the one body correlation function. A state is a BEC if its reduced single-particle density matrix has one or more eigenvalues that are of the order of the total particle number. As an example, Let us consider a two-level system containing N bosons. The ground and excited states are labeled by g and e with energy 0 and ϵ respectively. A Fock state with n excited particles is $|N-n, n\rangle$. For a Fock state $|N, 0\rangle$, its reduced single-particle density matrix is

$$\rho_1 = \begin{bmatrix} \langle a_g^\dagger a_g\rangle & \langle a_g^\dagger a_e\rangle \\ \langle a_e^\dagger a_g\rangle & \langle a_e^\dagger a_e\rangle \end{bmatrix} = \begin{bmatrix} N & 0 \\ 0 & 0 \end{bmatrix}. \tag{1.5}$$

It has one eigenvalue N, thus $|N, 0\rangle$ is a condensate.

If the reduced single-particle density matrix has two or more eigenvalues of the order N, the state is a fragmented condensate [8]. In the example above, both $\left|\frac{N}{2}, \frac{N}{2}\right\rangle$ and $\frac{1}{\sqrt{2}}(|N, 0\rangle + |0, N\rangle)$ are fragmented condensates, since their reduced single-particle density matrix is

$$\rho_1 = \begin{bmatrix} \frac{N}{2} & 0 \\ 0 & \frac{N}{2} \end{bmatrix}, \tag{1.6}$$

which has two eigenvalues proportional to N.

Reduced m-particle density matrix ρ_m can be defined similarly

$$\rho_{m,ij} = \mathrm{Tr}\Big(\rho a_i^{\dagger m} a_j^m\Big), \tag{1.7}$$

and their off-diagonal terms can be used to distinguish the states $\left|\frac{N}{2},\frac{N}{2}\right\rangle$ and $\frac{1}{\sqrt{2}}(|N,0\rangle + |0,N\rangle)$ above. The former has vanishing m-body correlation functions $\rho_{m,i\neq j}$ for any m, while the N-body correlation function of the latter is proportional to $N!$. A state with a vanishing one-body correlation function and a two-body correlation function proportional to N^2 is called a pair condensate [9–11]. In Chapter 2, we study the states with prevailing higher order correlation functions emergent in the quantum dynamics.

In experiments, many kinds of bosons forming BECs have internal degrees of freedom. For example, ^{23}Na, ^{39}K, and ^{87}Rb have hyperfine spin $f = 1$. A conventional magnetic trap will align the spins of atoms and thus freeze their internal degrees of freedom. Scalar field operators are enough to describe them [12]. On the other hand, the potential seen by an atom in an optical trap does not depend on its internal state. The internal degrees of freedom are therefore liberated and such a condensate is called a spinor Bose-Einstein condensate [13]. Because of the complex structure of mutual interactions when spins are involved, spinor BECs host more quantum phenomena. For instance, depending on the competition between interaction strengths of different total spin channels of two-body scattering, the ground state of a spin-1 BEC might be a polar state or a ferromagnetic state as a mean field result [14]. Chapter 5 presents an example of different ground states of a spin-1 BEC interacting with a spin-1/2 impurity immersed in it.

1.2 Disappearance and Revival of Loschmidt Echo

The Loschmidt echo describes the overlap of two final states coming from the same initial state $|\psi_0\rangle$ with two different Hamiltonians. It is defined as

$$M(t) = |\langle\psi_0| e^{iH_2 t} e^{-iH_1 t} |\psi_0\rangle|^2. \tag{1.8}$$

It can also be understood as using Hamiltonian H_2 to reverse the evolution caused by H_1 and measuring how perfect the reversion is. Loschmidt echo has been studied in many different scientific fields including quantum phase transitions, quantum chaos, and quantum chemistry. Loschmidt echo is also related to quantum Fisher information [15], which is defined as

$$I_\epsilon(t) = \lim_{\epsilon\to 0} \frac{1 - |\langle\psi_0| e^{iH(\alpha+\epsilon)} e^{-iH(\alpha)t} |\psi_0\rangle|^2}{\epsilon^2}. \tag{1.9}$$

Quantum Fisher information describes the sensitivity of the quantum evolution to the tunning parameter α of the Hamiltonian.

One particular type of Loschmidt echo is

$$M_G(t) = |\langle\psi_0| e^{-iHt} |\psi_0\rangle|^2, \tag{1.10}$$

where the bra $\langle\psi_0|$ does not evolve. It describes a system's memory of its initial state after it has evolved for time t. $M_G(t) = 0$ and $M_G(t) = 1$ are of great interests. The former means at some time the system completely forgets its initial state, and in the latter case, the system comes back to its initial state exactly after a finite time interval.

1.2.1 Lee-Yang zeros and dynamical quantum phase transitions

We first focus on $M_G(t) = 0$. Before discussing $M_G(t)$, let us first review the partition function $\mathcal{Z}(T, X)$ in thermodynamics, which will be shown related to the Loschmidt echo later. The partition function is defined as

$$\mathcal{Z}(T, X) = \sum_l \omega_l(X) e^{-\beta E_l(X)} \tag{1.11}$$

where $\beta = \frac{1}{k_B T}$, $E_l(X)$ is the energy level, $\omega_l(X)$ is the level degeneracy, and X represents parameters in the Hamiltonian, such as a magnetic filed. The partition function gives all information about a system at equilibrium. For example, the free energy F is given by

$$F = -\frac{\ln \mathcal{Z}(T, X)}{\beta} \tag{1.12}$$

For any finite-sized system, the partition function $\mathcal{Z}(T, X)$ is a positive and continuous function of the temperature T and other parameters X, therefore the free energy should also be a continuous and analytical function. However, in the thermodynamic limit, where the number of particles N of a system goes to infinity, experimentalists may observe phase transitions, where the free energy F shows non-analytical behaviors, such as a sudden jump or a sharp kink, as the parameters change.

Mathematically, the free energy in the thermodynamic limit should be expressed by

$$F = -\lim_{N\to\infty} \frac{1}{\beta} \ln\left(\sum_{l=0}^{\infty} \omega_l e^{-\beta E_l}\right) \tag{1.13}$$

The appearance of the non-analytical behaviors is a result of the fact that the order of the limit $N \to \infty$ and the summation cannot be switched. Lee and Yang gave another

interpretation [16]. They extended physical quantities, which should be real numbers, to the complex domain, and found that the partition function $\mathcal{Z}$ vanishes at some places of the complex plane. These zeros (called Lee-Yang zeros) correspond to the non-analytical behaviors of the free energy. Without taking thermodynamic limit, all zeros of the partition function are located away from the real axis, indicating that in a finite-sized system, physical quantities are continuous and analytical. As the number of particles N goes to infinity, those zeros gradually approach the real axis and trigger phase transitions. Lee-Yang zeros have been observed experimentally in a system where a probe spin is coupled to an Ising-type spin bath [17, 18].

Now if we write down the Loschmidt echo $M_G(t)$ using eigenstates of H,

$$M_G(t) = \left| \sum_n |c_n|^2 e^{-itE_n} \right|^2 , \tag{1.14}$$

we can see the similarity between $M_G(t)$ and $\mathcal{Z}(T, X)$: $M_G(t)$ is the partition function with an imaginary temperature $\beta = it$ if the initial state is an equal superposition of all the eigenstates. This inspires people to study the Loschmidt echo in the complex plane of time. Analogously, the zeros of Loschmidt echo result in the non-analytical properties of the so-called dynamical free energy,

$$\lambda(t) = -\frac{1}{N} \ln M_G(t). \tag{1.15}$$

The dynamical free energy is the probability rate for the system to return to its initial state. Consequently these zeros define dynamical quantum phase transitions (DQPT) [19, 20]. Dynamical quantum phase transitions have been studied in many system and it is a new method to study non-equilibrium quantum dynamics. It also has deep connections with equilibrium quantum phase transitions [21]. In Chapter 2, we will use dynamical quantum phase transition to study the emergence of highly entangled states in the dynamics of a two-site Bose-Hubbard model.

1.2.2 Revival of initial states and time crystals

While a vanishing Loschmidt echo defines DQPT, a Loschmidt echo periodically coming back to 1 introduces the concept of time crystals. Let us first review common crystals. It is well known that, a crystal is an array of atoms that are invariant only under translations by a linear combination of its lattice vectors. Thus its ground state only has discrete trans-

lation symmetry, albeit it lives in a space with continuous translation symmetry. We then conclude that a crystal breaks the continuous spatial translation symmetry spontaneously. Similarly, in 2012, F. Wilczek proposed the idea of a time crystal, a system breaking the temporal translation symmetry spontaneously [22, 23]. A trivial example of broken continuous temporal translation symmetry is a spinning object, which only gets back to the initial orientation after one period. However, if we want to say "spontaneously", we have to consider ground states. Apparently a spinning object is not having the lowest energy. Its lowest energy state has zero angular momentum and the continuous temporal translation symmetry thus survives. Therefore the idea of time crystals results in a lot of debates [24–28]. In 2015, H. Watanabe and M. Oshikawa proved a no-go theorem ruling out the possibility of a time crystal breaking the continuous time translation symmetry spontaneously in the ground state or at thermal equilibrium [29].

The no-go theorem inspires people to switch to open quantum systems and discrete temporal translation symmetries [29–41]. Consider a system under periodic drivings, which means its Hamiltonian is time dependent and has period T: $H(t+T) = H(t)$. In this case the Hamiltonian has discrete temporal translation symmetry. People want to explore whether the system dynamics can break this symmetry of the Hamiltonian. From Floquet theorem we know the system has Floquet eigenstates $|\psi_n\rangle$ and eigenenergies E_n satisfying

$$\mathcal{U}(T)\,|\psi_n\rangle = e^{-iE_nT}\,|\psi_n\rangle \tag{1.16}$$

where $\mathcal{U}(T)$ is the time evolution operator for one period. If the system initially is prepared in any Floquet eigenstates, the wavefunction $|\Psi(t)\rangle$ of the system has period T (the overall phase factor is ignored). Thus the discrete temporal translation symmetry remains. If a Floquet eigenstate is a superposition of two macroscopically different states, for instance, Floquet eigenstates $|F_\pm\rangle = \frac{1}{\sqrt{2}}(|M_1\rangle \pm |M_2\rangle)$ with Floquet eigenenergies $E_\pm$ and $|M_{1,2}\rangle$ are very different from each other, it is not hard to imagine that under any infinitesimal perturbation, the states $|F_\pm\rangle$ will collapse to one of the two states, say $|M_1\rangle$. The system turns into a superposition of two Floquet eigenstates, $|M_1\rangle = \frac{1}{\sqrt{2}}(|F_+\rangle + |F_-\rangle)$, and as time goes on, the wavefunction at the end of the m-th period is

$$|\Psi(t=mT)\rangle = \frac{1}{\sqrt{2}}\left(|F_+\rangle + e^{i(E_+-E_-)mT}\,|F_-\rangle\right). \tag{1.17}$$

Depending on the values of $E_\pm$, it is possible that only for some $m > 1$ can $(E_+ - E_-)mT$

become a multiple of 2π. That means the dynamics of the system and correspondingly, some physical observables, show a period of mT, $m > 1$. Because the response of the observable does not have the same period as the driving field, we can conclude that such a system spontaneously breaks the discrete temporal translation symmetry and is eligible to be called a discrete time crystal (DTC).

The idea of DTC above has been realized in a disordered spin model with many body localization [33–35]. While many researches have demonstrated the stability of such realizations against a few sources of imperfections, the spatial fluctuations of the driving filed are completely ignored. In Chapter 3, we present a clean DTC model without disorder. Stabilized by all-to-all interactions, it is robust against the imperfections from the driving field.

1.3 Out-of-Time-Order Correlators and Backward Evolution

Recently the out-of-time-order correlators (OTOC) [42–50] has attracted attentions from both the community of condensed matter physics and high energy physics. According to Ref. [43, 45], the OTOC is defined as

$$C(t) = -\langle [W(t), V]^2 \rangle_\beta \tag{1.18}$$

where $\langle \cdot \rangle_\beta$ denotes thermal average, and W and V are Hermitian operators. Such an OTOC can be regarded as a quantum version of the Lyapunov exponent. In classical mechanics, the Lyapunov exponent λ is defined as

$$\lambda = \lim_{t\to\infty} \lim_{|\delta x(0)|\to 0} \frac{1}{t} \ln \frac{|\delta x(t)|}{|\delta x(0)|}, \tag{1.19}$$

which indicates $\frac{\delta x(t)}{\delta x(0)} \sim e^{\lambda t}$. It describes the sensitivity of a system's coordinate x to the initial condition $x(0)$ after an infinite evolution time. For a classically chaotic system, the position's deviation is expected to grow exponentially. $\frac{\delta x(t)}{\delta x(0)}$ is also equal to the Poisson bracket $\{x(t), p(0)\}$. Thus $\{x(t), p(0)\} \sim e^{\lambda t}$. From classical mechanics to quantum mechanics, we replace Poisson brackets $\{,\}$ by operator commutators $\frac{1}{i\hbar}[,]$. Formally we can define the Lyapunov exponent from quantum position operator $\hat{x}(t)$ and momentum operator $\hat{p}(0)$,

$$\left\langle \left(\frac{1}{i\hbar} [\hat{x}(t), \hat{p}(0)] \right)^2 \right\rangle = -\frac{1}{\hbar^2} \langle [\hat{x}(t), \hat{p}(0)]^2 \rangle \sim e^{2\lambda t}, \tag{1.20}$$

where $\langle\cdot\rangle$ represents the expectation value for some quantum state. On the other hand, the OTOC of position operator $\hat{x}$ and momentum operator $\hat{p}$ is $C(t) = -\langle[\hat{x}(t), p]^2\rangle$, which is just the quantity in Eq. (1.20). Further, reachers extend this definition to the OTOC of any two Hermitian operators W and V and calculate the Lyapunov exponent through $\hbar^2 e^{2\lambda t} = C(t) = -\langle[\hat{W}(t), V]^2\rangle$.

There is also literature defining OTOC as

$$F(t) = \langle\Psi| A(t)^\dagger B^\dagger A(t) B |\Psi\rangle , \tag{1.21}$$

where A and B can be either unitary operators [44, 45, 50] or Hermitian operators [46, 48]. This definition can be understood in the following way,

$$|\psi_1\rangle = A(t)B|\Psi\rangle = e^{iHt} A e^{-iHt} B |\Psi\rangle , \tag{1.22}$$

$$|\psi_2\rangle = BA(t)|\Psi\rangle = B e^{iHt} A e^{-iHt} |\Psi\rangle . \tag{1.23}$$

$|\psi_1\rangle$ is obtained by first applying B on the initial state $|\Psi\rangle$, evolving for t, applying A, and back-evolving for t, and $|\psi_2\rangle$ is obtained by first evolving for t, applying A, back-evolving for t, and applying B. $F(t)$ is the overlap between the two final states. Therefore it can be regarded as a more complicated Loschmidt echo and it describes the way A and B inhibit the cancellation between forward e^{-iHt} and backward e^{iHt} evolution. For unitary operators A and B,

$$2(1 - \mathrm{Re}\, F(t)) = \langle|[A(t), B]|^2\rangle. \tag{1.24}$$

In a many-body system, if A and B are two local operators far away from each other, initially $[A(0), B(0)] = 0$. If A and B does not commute with the Hamiltonian and the Hamiltonian is time-independent, the decrease of $\mathrm{Re}\, F(t)$ tells how $A(t)$ gradually become spatially extensive such that it eventually does not commute with B anymore. Therefore $F(t)$ can also be used to study the information spreading in quantum system evolution [43, 44, 49, 50].

No matter which specific definition is going to be used, experimentally, to measure OTOC, an indispensable step to realize backward evolution e^{iHt}. Generally, it is hard to completely reverse the sign of a Hamiltonian since the kinetic energy is not as easy as the potential energy to be reversed. In Chapter 4, we demonstrate a concrete example where we can use a series of evolution to create an equivalent $-H$. It is similar to the traditional spin echo [51],

but it applies to systems with SU(1,1) symmetry instead of SU(2).

1.4 Decoherence of a System Interacting with the Environment

Up to now we have been focusing on isolated systems. A wave function provides a complete description of a physical system [52]. Whereas a measurement on this system may still give us probability results, the probability comes from Heisenberg's uncertainty principle, which is a fundamental rule of the nature. On the other hand, in classical mechanics, the concept "ensemble" describes a system in a few possible states with probabilities p_i ($\sum p_i = 1$). Here the probability, however, comes from our lack of information, which means the system in fact is in some specific state, but the observer simply does not know which state it is. If we are allowed to do enough measurements, we shall get enough information to determine the system's actual state. To describe an ensemble consisting of quantum states $|\psi_i\rangle$, we use a density matrix $\rho = \sum_i p_i |\psi_i\rangle \langle\psi_i|$. For instance, a canonical ensemble of temperature $T = 1/k_B\beta$ is

$$\rho_c = \sum_i p_i |E_i\rangle \langle E_i| , \; p_i = \frac{e^{-\beta E_i}}{\mathcal{Z}}. \tag{1.25}$$

We shall be careful that ρ_c is different from a superposition of energy eigenstates

$$|\Psi\rangle = \sum_i \sqrt{p_i} |E_i\rangle , \tag{1.26}$$

which can be expressed by another density matrix

$$\rho_s = |\Psi\rangle \langle\Psi| = \sum_i p_i |E_i\rangle \langle E_i| + \sum_{i\neq j} \sqrt{p_i p_j} |E_i\rangle \langle E_j| . \tag{1.27}$$

All the off-diagonal terms ($i \neq j$) are not present in ρ_c. If we measure an observable O of the two states, for ρ_c, the averaged value is time independent $\langle O\rangle_c = \sum_i p_i \langle E_i| O |E_i\rangle$, while for ρ_s,

$$\langle O\rangle_s = \sum_i p_i \langle E_i| O |E_i\rangle + \sum_{i\neq j} \sqrt{p_i p_j} \langle E_i| O |E_j\rangle \cos((E_i - E_j)t). \tag{1.28}$$

We then say that in the classical ensemble, there are no definite phase coherence between states.

For a system S interacting with the environment E, although the system S plus the environment E can be viewed as a big isolated system, an observer may not have the ability

to include the whole environment into her measurements. In this case, from the view of the observer, the system is described by a reduced density matrix

$$\rho_S = \mathrm{Tr}_E \left|\Psi\right\rangle \left\langle\Psi\right|, \tag{1.29}$$

where $|\Psi\rangle$ is the total wave function for the system plus the environment. ρ_S is obtained from the partial trace of the total density matrix $|\Psi\rangle\langle\Psi|$ with respect to the environment. Let us consider a simple example. If we have a spin-1/2 as the system interacting with another spin-1/2 as the environment and the total Hamiltonian is

$$H = \sigma_{z1} + \sigma_{z2} + \sigma_{z1} \otimes \sigma_{z2}. \tag{1.30}$$

For the total initial state,

$$|\Psi(0)\rangle = \frac{1}{\sqrt{2}} \left(|\uparrow\rangle_1 + |\downarrow\rangle_1\right) \otimes \frac{1}{\sqrt{2}} \left(|\uparrow\rangle_2 + |\downarrow\rangle_2\right), \tag{1.31}$$

the reduced density matrix of the first spin is

$$\rho_1(0) = \frac{1}{2}(|\uparrow\rangle\langle\uparrow| + |\downarrow\rangle\langle\downarrow|) + \frac{1}{2}(|\uparrow\rangle\langle\downarrow| + |\downarrow\rangle\langle\uparrow|). \tag{1.32}$$

At time $\tau = \frac{\pi}{4}$ (We set $\hbar = 1$ in this subsection), the total wave function becomes

$$|\Psi(\tau)\rangle = \frac{1}{2}|\uparrow\rangle_1 \otimes (e^{-i\frac{3}{4}\pi}|\uparrow\rangle_2 + e^{i\frac{\pi}{4}}|\downarrow\rangle_2) + \frac{1}{2}|\downarrow\rangle_1 \otimes (e^{i\frac{\pi}{4}}|\uparrow\rangle_2 + e^{i\frac{\pi}{4}}|\downarrow\rangle_2), \tag{1.33}$$

and the reduced density matrix of the first spin is

$$\rho_1(\tau) = \frac{1}{2}(|\uparrow\rangle\langle\uparrow| + |\downarrow\rangle\langle\downarrow|). \tag{1.34}$$

The off-diagonal terms disappears and the coherence are lost from the view of the observer. The reason is apparent. Because of the interaction, the two states of the first spin, $|\uparrow\rangle_1$ and $|\downarrow\rangle_1$, are coupled to two orthogonal states of the environment at τ such that the off-diagonal terms vanishes after we do the partial trace.

For the example above, the off-diagonal terms only completely vanish at $t = \frac{\pi}{4}(1+2k), k \in \mathbb{Z}$. In reality, an environment is much more complex and contains more degrees of freedom. It is not hard to imagine that, the two states of the system spin will be coupled to orthogonal environment states as time goes on. Further, in a relatively long time scale, while the environment states evolve, they keep orthogonal to each other. To be more precise, the overlaps between those environment states are scaled down exponentially as the size of the environment increases [53, 54]. As a result, an observer only sees a density matrix without

off-diagonal terms for during this long time scale. This process is called decoherence. Decoherence does not mean coherence disappears. Actually the coherence of the small subsystem "flows" into the larger system including the environment, but because of the lack of the information about the environment, an observer cannot see the coherence.

Ultracold atom experiments provide a good platform for studying coherence, because the cold atom system usually has little interactions with the environment and maintains coherence for a relatively long time. Experimentalists thus can create an nearly isolated system and take a small part as the subsystem and the remaining part as the environment. In Chapter 5, we study an spin impurity interacting with a BEC. By looking at the decoherence of this spin, we are able to infer the state of the environment BEC.

2. DYNAMICAL QUANTUM PHASE TRANSITIONS IN INTERACTING ATOMIC INTERFEROMETERS

This chapter is based on the published article [55] by C. Lyu and Q. Zhou, Dynamical quantum phase transitions in interacting atomic interferometers, Phys. Rev. A ***101****, 043605 (2020). Copyright (2020) by the American Physical Society.*

Applications of atomic interferometers span a wide spectrum of problems, ranging from measuring the gravitational acceleration [56, 57] and the fine-structure constant [58] to detecting gravitational waves [59, 60]. Ultracold atoms prompt a precise control of atomic interferometers, including realizing highly tunable atomic beam splitters [61–65] and accessing an atomic Hong-Ou-Mandel interferometer using optical tweezers [3, 4, 66, 67]. Whereas mutual interactions between particles may induce the decoherence of a subsystem [68–70], they could also generate squeezing and multi-particle correlations unattainable in linear interferometers [71].

Dynamical quantum phase transition has recently invoked enthusiasm in multiple disciplines [19–21, 72–79]. A particular type of Loschmidt echo,

$$|G(t)|^2 = |\langle\psi(0)|\, e^{-\frac{i}{\hbar}\hat{H}t}\, |\psi(0)\rangle\,|^2,$$

where $|\psi(0)\rangle$ is the initial state, is considered as the temporal analog of the partition function. When $|\psi(0)\rangle$ is an equal superposition of all energy eigenstates, $|G(t)|^2$ is exactly the partition function with an imaginary temperature $T = \frac{1}{ik_B t}$. t is therefore identified as the tuning parameter as analogous to the temperature in phase transitions at equilibrium. When $G(t) = 0$, the dynamical free energy $\lambda(t) = -\frac{1}{N}\ln|G(t)|^2$, which is the rate function of the probability for the system to return to its initial state, manifests nonanalyticities and defines a critical time t_c. N is the number of degrees of freedom. Similar to conventional phase transitions triggered by Lee-Yang zeros or Fisher zeros in the complex plane of certain parameters or the temperature [16, 80], DQPTs can also be understood from zeros of $G(t)$ in the complex plane by extending the real time t to the complex domain, $t \to z \equiv t + i\tau$. With increasing N, discrete zeros merge to continuous manifolds and eventually touch the real t axis, making physical observables nonanalytic. Whereas observations of DQPTs have been reported in certain spin systems, showing deep connections with equilibrium quantum phase transition and order-parameter dynamics [21, 72, 74, 76, 77, 79], such novel concept well deserves both theoretical and experimental studies in a much broader range of systems.

This chapter shows that interacting interferometers host DQPTs between highly entangled quantum states. Starting from a Fock state, pair condensates, which are featured with vanishing one-body correlation and prevailing two-body correlations [9–11], arise in non-equilibrium quantum dynamics. In the large N limit, their appearance at critical times, t_c, is triggered by zeros of $G(z)$ in the complex time plane that approach the real axis, signifying DQPTs at which the many-body wave function becomes orthogonal to the initial state. t_c also characterizes transitions between NOON states, a particular type of Schrödinger's cat states formed by two Fock states. Such dynamically generated NOON states are much more stable than those at equilibrium. The energy mismatch between the two single-particle states only needs to be suppressed as a power-law of N, unlike the equilibrium case where the energy mismatch has to be exponentially small.

Moreover, NOON states arise from an intriguing interplay between interactions and the symmetry. When the Hamiltonian remains unchanged after swapping the two single-particle states, the dynamical phase induced by interactions directly leads to a superposition of the initial state and its counterpart created by the symmetry operator, say $|N,0\rangle$ and $|0,N\rangle$. Therefore, the NOON states are protected by the symmetry in the sense that any perturbations respecting this symmetry are no longer important. For instance, adding weak multi-particle interactions to the ordinary two-particle interactions does not affect any qualitative results. Thus, our scheme applies to a large class of models and suggests a new mechanism to access highly entangled states, which could be used to beat the standard quantum limit and improve quantum sensing [81–84].

2.1 Loschmidt Echo of Two-Site Bose-Hubbard Model

We consider N bosonic atoms in an interferometer consisting of two quantum states. The Hamiltonian, known as the two-site Bose-Hubbard model, reads

$$\hat{H} = -J(\hat{a}_1^\dagger \hat{a}_2 + \hat{a}_2^\dagger \hat{a}_1) + g(\hat{n}_1^2 + \hat{n}_2^2) + 2g_{12}\hat{n}_1\hat{n}_2, \tag{2.1}$$

where $J > 0$ is the the coupling strength between the two quantum states, $\hat{a}_i^\dagger$ is the creation operator in the ith state, and $\hat{n}_i = \hat{a}_i^\dagger \hat{a}_i$. g and g_{12} are the intra- and inter-state interactions, respectively. This Hamiltonian remains unchanged with two modes swapped. If we consider two spatial modes, this is the inversion symmetry. Though our results apply to generic models respecting this symmetry, we focus on two-particle interactions to concretize discussions.

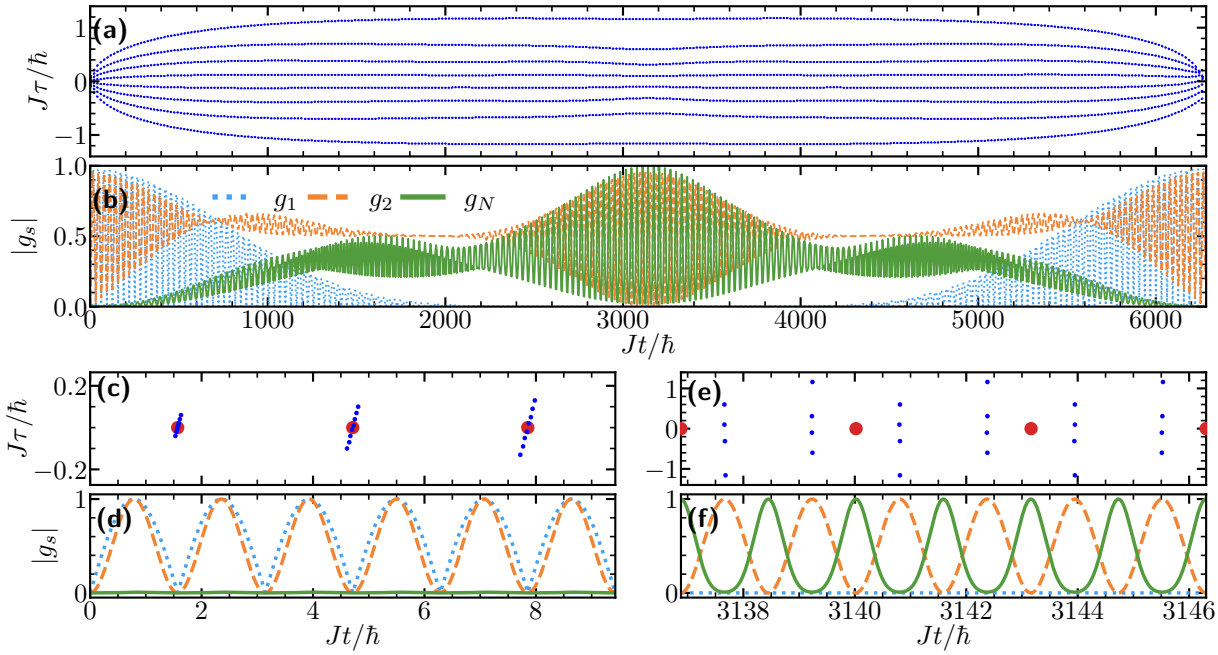

Figure 2.1: Dynamics of 8 bosons for $U/J = 0.001$. (a) Each blue dot represents a simple zero of $G(z)$ in the complex plane, where z is the complex time $z = t + i\tau$. (b) Normalized s-body correlation $\frac{2|g_1|}{N}, \frac{4|g_2|}{N(N-1)}, \frac{2|g_N|}{N!}$ along the real time axis of (a). (c,d) and (e, f): Enlarged regimes of of (a,b) near $t = 0$ and t^*, respectively. Each red dot in (c,e) is a zero of $G(z)$ of the non-interacting systems described by $z = (k + 1/2)T, k \in \mathbb{Z}$. Each of them has multiplicity 8.

Multi-particle interactions, which may arise from multi-band effects [85], are discussed in Sec. 2.4.

The Hamiltonian can be rewritten as

$$\hat{H} = -J(\hat{a}_1^\dagger \hat{a}_2 + \hat{a}_2^\dagger \hat{a}_1) + \frac{\bar{U}}{2}(\hat{n}_1 + \hat{n}_2)^2 + \frac{U}{4}(\hat{n}_1 - \hat{n}_2)^2, \tag{2.2}$$

where $\bar{U} = g + g_{12}$, $U = 2(g - g_{12})$. Due to the conservation of the total particle number $N = n_1 + n_2$, $\bar{U}$ only contributes a trivial total phase of the wave function in the dynamics. We thus focus on interaction effects caused by U. Though this Hamiltonian has been well studied [68, 71, 86–90], our results, including zeros of $G(z)$ in the complex time plane, DQPTs, symmetry protected pair condensates, elude the literature. We solidify the discussion for repulsive interactions, $U > 0$. Attractive interactions lead to similar results, see Appendix 2.6.3.

We consider an initial state, $|\psi(0)\rangle = |N, 0\rangle = \frac{1}{\sqrt{N!}}\hat{a}_1^{\dagger N}|0\rangle$. The dynamical evolution, $|\psi(t)\rangle = e^{-\frac{i}{\hbar}\hat{H}t}|\psi(0)\rangle$, is computed by expanding $|\psi(0)\rangle$ using exact eigenstates of $\hat{H}$. Whereas this can be done for any parameters, we consider $UN^2 \ll J$. Such energy scale separation leads to a time scale separation,

$$T \equiv \frac{\pi\hbar}{J} \ll t^* \equiv \frac{\pi\hbar}{U}, \tag{2.3}$$

which allows us to access quantum dynamical evolution exhibiting extraordinary features. When U vanishes, the quantum dynamics is governed by

$$\hat{a}_1^\dagger \to \cos\frac{Jt}{\hbar}\hat{a}_1^\dagger + i\sin\frac{Jt}{\hbar}\hat{a}_2^\dagger, \tag{2.4a}$$

$$\hat{a}_2^\dagger \to i\sin\frac{Jt}{\hbar}\hat{a}_1^\dagger + \cos\frac{Jt}{\hbar}\hat{a}_2^\dagger. \tag{2.4b}$$

Thus, $|\psi^o(t)\rangle = \frac{1}{\sqrt{N!}}(\cos(Jt/\hbar)\hat{a}_1^\dagger + i\sin(Jt/\hbar)\hat{a}_2^\dagger)^N|0\rangle$, where the superscript o represents the result of a non-interacting system. Extending t to the complex plane, we find that all zeros of $G(z)$ are located on the real axis with multiplicity N. When $z = t_k^o \equiv (k + 1/2)T$, where k is an integer, the quantum state becomes $|0, N\rangle = \frac{1}{\sqrt{N!}}\hat{a}_2^{\dagger N}|0\rangle$, and $G(t_k^o) = 0$. One can view each identical boson as a spin-1/2. All spin-1/2s initially at the north pole of the Bloch sphere move to the south pole at the same times t_k^o, leading to a vanishing $G(z)$.

As shown in Fig. 2.1(c), a weak interaction satisfying $UN^2 \ll J$ has negligible effects at small times. A given multiple zero with multiplicity N now splits into N simple zeros, all of which are close to zeros of non-interacting systems. Indeed, $|\psi(t)\rangle$ is very similar to that of a non-interacting case, as shown in Fig. 2.2(a-d). For instance, at time $t = t^o \pm T/4$,

$|\psi(t)\rangle$ is well represented by $\frac{1}{\sqrt{2^N N!}}(\hat{a}_1^\dagger \pm i\hat{a}_2^\dagger)^N|0\rangle$, corresponding to a binomial distribution when expanded by Fock states $|l\rangle \equiv |N/2+l, N/2-l\rangle$. To simplify notations, we consider even N here. See Appendix 2.6.3 for results of odd N. However, at large times, even a weak interaction has profound effects. As shown in Fig. 2.1(a), the separation between different zeros of $G(z)$ gets amplified greatly. Near t^*, these zeros deviate largely from those of non-interacting systems. Whereas such zeros have finite imaginary parts, they intrinsically affect physical observables in the real time axis, as shown later.

2.2 Dynamically Generated Entangled States

We evaluate generic s-body correlation functions in the real time axis,

$$g_s = \langle\psi(t)|\,\hat{a}_1^{\dagger s}\hat{a}_2^s\,|\psi(t)\rangle\,, s\in\mathbb{Z}^+.$$

At $t=0$, the Fock state has vanishing g_s for any s. As time goes on, g_s increases as a result of tunnelings between the two quantum states. When $U=0$, the dynamics is fully captured by Rabi oscillations. When $U\neq 0$, Fig. 2.1(b) shows that one-body correlation function, $g_1(t)$, decays due to interaction induced decoherence. However, higher order correlation functions have distinct behaviors. Normalized two-body and N-body correlation functions, $\frac{4g_2(t)}{N(N-1)}$ and $\frac{2g_N(t)}{N!}$, reach their maxima around $t=t^*$. In the vicinity of t^*, both $|g_2|$ and $|g_N|$ oscillate with a period $T/2$. This indicates the rise of highly entangled states with multi-particle correlations. As shown in Fig. 2.2(e-h), the four states showing up alternatively near t^* are well captured by

$$\begin{aligned}
\tilde{t}_0 &= kT, & |C_-\rangle &= \frac{\hat{a}_1^{\dagger N} - i\hat{a}_2^{\dagger N}}{\sqrt{2N!}}\,|0\rangle\,,\\
\tilde{t}_1 &= kT+\frac{T}{4}, & |P_-\rangle &= \sum_{n=0}^{N}\frac{i^{N-n}-i^{n+1}}{n!(N-n)!\sqrt{\frac{2^{N+1}}{N!}}}\hat{a}_1^{\dagger n}\hat{a}_2^{\dagger N-n}\,|0\rangle\,,\\
\tilde{t}_2 &= kT+\frac{2T}{4}, & |C_+\rangle &= \frac{\hat{a}_1^{\dagger N} + i\hat{a}_2^{\dagger N}}{i^{1-N}\sqrt{2N!}}\,|0\rangle\,,\\
\tilde{t}_3 &= kT+\frac{3T}{4}, & |P_+\rangle &= \sum_{n=0}^{N}\frac{i^{N-n}+i^{n+1}}{i^{1-N}n!(N-n)!\sqrt{\frac{2^{N+1}}{N!}}}\hat{a}_1^{\dagger n}\hat{a}_2^{\dagger N-n}\,|0\rangle\,,
\end{aligned} \tag{2.5}$$

where $\tilde{t}=t-t^*$. $|C_\pm\rangle$ are NOON states with vanishing $g_{s<N}$ and $|g_N| = N!/2$. We have verified that any $g_{s<N}$ does vanish when NOON states arise. For clarity of the plots, $g_{2<s<N}$

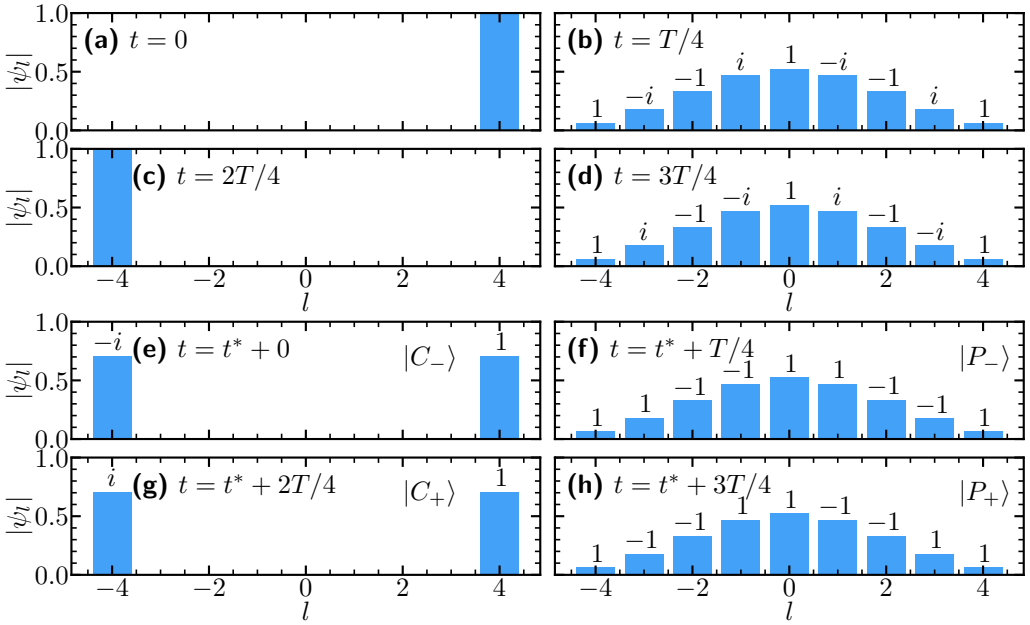

Figure 2.2: (a-d) depicts the wave function $|\psi(t)\rangle = \sum \psi_l \left|\frac{N}{2}+l, \frac{N}{2}-l\right\rangle$ expanded by Fock states at four small times $t = 0, T/4, 2T/4, 3T/4$. (e-h) are the results at four times near t^*. Numbers on top of bars represent relative phases of ψ_l. All parameters are identical to those in Fig. 2.1.

are not shown in Fig. 2.1.

States $|P_\pm\rangle$ are called pair condensates, since their one-body correction function g_1 vanishes, and their two-body correlation function g_2 is of the order of N^2. Correspondingly, their two-body reduced density matrix, $\langle a_i^{\dagger 2} a_j^2 \rangle$, has only one macroscopic eigenvalue proportional to N^2. Therefore, $|P_\pm\rangle$ and $|C_\pm\rangle$ have distinct properties. Eq. (2.4), which can be regarded as a rotation of the quantization of axis, swaps $|P_\pm\rangle$ and $|C_\pm\rangle$. There are always two types of such different entangled states in any reference frames. As shown later, when studying $|G(t)|^2 = |\langle\psi(0)| e^{-\frac{i}{\hbar}\hat{H}t} |\psi(0)\rangle|^2$ that characterizes the quantum memory of the initial state, the chosen $|\psi(0)\rangle$ fixes the quantization axis such that $|P_\pm\rangle$ in Eq. (2.5) becomes orthogonal to $|\psi(0)\rangle$ when $N \to \infty$.

The energy spectrum in the limit $UN^2 \ll J$ (Appendix 2.6.1), which is written as

$$E_n = An + Bn^2, \ n = 0, 1, .., N, \tag{2.6}$$

$$B = -\frac{U}{2}, \quad A = \frac{UN}{2} + 2J, \quad r \equiv \frac{A}{B}. \tag{2.7}$$

For any initial state $|\psi(0)\rangle = \sum_{n=0}^{N} c_n |E_n\rangle$, the wave function at a later time is given by $|\psi(t)\rangle = \sum_{n=0}^{N} c_n e^{-\frac{i}{\hbar}E_n t} |E_n\rangle$. Tuning J and U, when $r = r_m$ is satisfied, where $r_m = 4m + 2$

or $4m$, $m \in \mathbb{Z}$, $|C_\pm\rangle$ can be easily identified. If $r = 4m$, we obtain

$$|\Psi(t^*)\rangle = \sum_{n=0}^{N} c_n e^{-\frac{i}{\hbar}E_n t^*} |E_n\rangle = \sum_{n=0}^{N} c_n \frac{1 - i(-1)^n}{\sqrt{2}} |E_n\rangle . \tag{2.8}$$

Because of the aforementioned symmetry of H in Eq. (2.2), the energy eigenstates have well defined parity,

$$\hat{P} |E_n\rangle = (-1)^n |E_n\rangle , \tag{2.9}$$

where $\hat{P}$ is the inversion operator, $\hat{P}|n_1, n_2\rangle = |n_2, n_1\rangle$ and $[\hat{H}, \hat{P}] = 0$. Using Eq. (2.8) and (2.9), we conclude that $|\psi(t^*)\rangle = (|\psi(0)\rangle - i\hat{P}|\psi(0)\rangle)/\sqrt{2}$. Whereas this result is valid for any initial state, the initial state we chose gives rise to $|C_-\rangle$ emerging at $t = t^*$. Meanwhile, interaction effects are negligible in a short time scale of a few Ts. The time evolution in such time scale is well captured by Eq. (2.4) if we replace t by $t - t^*$. Applying such transformation to $|C_-\rangle$, it is straightforward to prove that the other three states in Eq. (2.5) show up in corresponding times. If $r = 4m + 2$, the same discussions apply and the four states, $|C_+\rangle$, $|P_+\rangle$, $|C_-\rangle$ and $|P_-\rangle$, show up at times $\tilde{t}_0, \tilde{t}_1, \tilde{t}_2, \tilde{t}_3$ in Eq. (2.5). It is also worth mentioning that, for odd particle numbers, the pair condensates are described by another type of wave functions $\sim \sum_l \psi'_l \hat{a}_1^{\dagger 2l} \hat{a}_2^{\dagger N-2l} |0\rangle$ (Appendix 2.6.3).

When $r \neq r_m$, Eq. (2.8) can not be satisfied. Nevertheless, the states near $t = t^*$ are well approximated by NOON states in the weakly interacting regime. We calculate the fidelity,

$$Q(t) = \max(|\langle C_+|\psi(t)\rangle|^2, |\langle C_-|\psi(t)\rangle|^2). \tag{2.10}$$

Near t^*, we obtain (Appendix 2.6.2)

$$Q(t) \approx \sqrt{\frac{1}{1 + \frac{N^2}{4}(\frac{\pi}{2} - \frac{U}{2\hbar}t)^2}} \sum_k \left| \exp\left(-\frac{1}{\frac{2}{N} + i\left(\frac{\pi}{2} - \frac{U}{2\hbar}t\right)} \left(\frac{k\pi}{2} - \frac{\pi N}{4} - \frac{Jt}{\hbar} \right)^2 \right) \right|^2 . \tag{2.11}$$

$Q(t)$ consists of multiple gaussian peaks centered at a series of discrete times with a separation $T/2$. Since the width of those peaks is about $\frac{\hbar}{\sqrt{N}J}$, only one peak contributes to $Q(t)$ significantly at any t in the large N limit. $Q(t)$ reaches its maximum at $t^{*\prime} = \frac{k_0 \pi \hbar}{2J} - \frac{\pi N \hbar}{4J}$, and

$$\max[Q(t)] = \left(1 + \left(\frac{N\pi U d}{8J} \right)^2 \right)^{-1/2} , \tag{2.12}$$

where k_0 is the integer nearest to $\frac{2J}{U} + \frac{N}{2}$, $k_0 \equiv \mathrm{Int}(\frac{2J}{U} + \frac{N}{2})$, and $d \equiv |\frac{2J}{U} + \frac{N}{2} - k_0| \leqslant \frac{1}{2}$. When

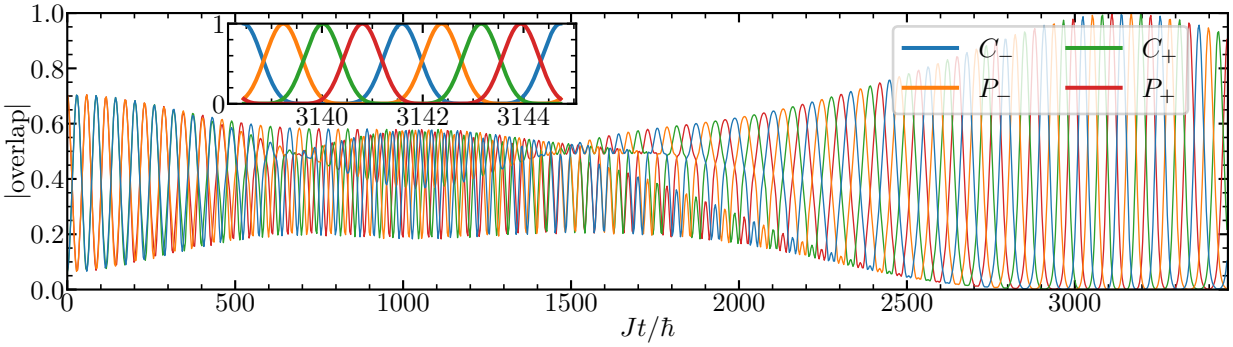

Figure 2.3: The overlaps between the state $|\psi_t\rangle$ and four entangled states defined in Eq. (2.5) as a function of time. We have used $N = 8$ bosons and $U/J = 0.001$. The inset zooms in to $t = t^*$.

$r = r_m$, previous results are recovered because $\frac{2J}{U} + \frac{N}{2} = -\frac{r_m}{2}$ is an integer and $\max[Q(t)] = 1$. For generic $r \neq r_m$, the lower bound of $\max[Q(t)]$ is written as $(1 + (\frac{\pi NU}{16J})^2)^{-1/2}$. Thus, in the weakly interacting limit, NOON states well represent $|\psi(t^{*\prime})\rangle$.

Away from t^*, there is no simple analytical expression for the overlap between $|\psi(t)\rangle$ and the NOON states or pair condensates in Eq. (2.5). We thus evaluate such overlaps numerically, as shown in Fig. 2.3. Around $t^* = \frac{\pi\hbar}{U}$, the four states defined in Eq. (2.5) show up alternatively. The overlaps reach maxima near t^*.

When $r = r_m$ is satisfied, since at $t = t^*$, $|\psi(0)\rangle$ becomes $|\psi(t^*)\rangle = \frac{1}{\sqrt{2}}(|\psi(0)\rangle - i\hat{P}|\psi(0)\rangle)$, we can expect that another initial state $\hat{P}|\psi(0)\rangle$ becomes $\frac{1}{\sqrt{2}}(\hat{P}|\psi(0)\rangle - i|\psi(0)\rangle)$ at $t = t^*$. Combining these together, we conclude that the original initial state $|\psi(0)\rangle$ becomes $-i\hat{P}|\psi(0)\rangle$ at $t = 2t^*$. Further, $|\psi(4t^*)\rangle = -|\psi(0)\rangle$. Therefore after $4t^*$, we see a revival of the initial state. This is also referred as the revival of rotational wave packets [91, 92].

2.3 DQPT in the Large Particle Number Limit

In a short time scale of a few Ts, the dynamics near t^* is well captured by Eq. (2.4) with the substitution $\tilde{t} = t - t^*$. Zeros of $G(z)$ are obtained analytically. For instance, when $r = 4m$,

$$G(z) = \frac{1}{\sqrt{2}}\left(\left(\cos\frac{J(z-t^*)}{\hbar}\right)^N - i\left(i\sin\frac{J(z-t^*)}{\hbar}\right)^N\right). \tag{2.13}$$

Fig. 2.4(a) shows that real parts of these zeros are given by $\mathrm{Re}\, z = t^* + (\frac{\pi}{4} + \frac{m}{2}\pi)\frac{\hbar}{J}, m \in \mathbb{Z}$, i.e., they are aligned in vertical lines in the complex plane. When N is odd, some zeros reside on the real axis (Appendix 2.6.3). However, for a generic finite N, all zeros are away

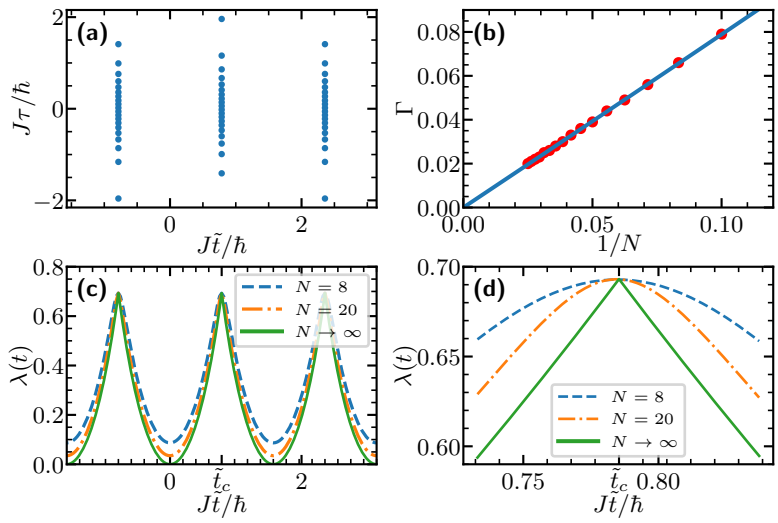

Figure 2.4: (a) Zeros of $G(z)$ near t^* for $N = 40$ particles ($\tilde{t} \equiv t - t^*$). (b) Distances between the real time axis and the nearest zeros around t^* as a function of $1/N$. The blue line is the analytical result from Eq. (2.14) and the red dots are numerical results. (c) The rate function $\lambda(t)$. (d) $\lambda(t)$ near $\tilde{t}_c$. $UN^2/J = 0.01$ has been used.

from the real axis. With increasing N, zeros become denser and gradually approach the real axis. The distance between the real axis and the nearest zero is bounded by

$$\Gamma = \frac{1}{2} \operatorname{arcosh} \frac{1}{|\cos \frac{\pi}{2N}|}. \tag{2.14}$$

In the large N limit, $\Gamma \approx \frac{\pi}{4N}$. Such scaling behavior is verified by numerical calculations in Fig. 2.4(b). When $N \to \infty$, straight lines formed by continuous zeros intersect with the real axis and lead to a vanishing $G(z)$ in the real axis. Correspondingly, $\lambda(t)$ becomes nonanalytic, signifying DQPTs. As shown in Fig. 2.4(c,d), near the transition point, $\lambda(t) = \ln 2 - 2\frac{J}{\hbar}|\tilde{t} - \tilde{t}_c|$ when $N \to \infty$, where $\tilde{t}_c = (\frac{\pi}{4} + \frac{m}{2}\pi)\frac{\hbar}{J}$. Comparing DQPT points and the times given in Eq. (2.5), we conclude that pair condensates, $|P_\pm\rangle$, reside at DQPT points and characterize the DQPT between two different types of NOON states, $|C_\pm\rangle$. This can also been seen from Fig. 2.1(e,f). Zeros of $G(z)$ near t^* are aligned in vertical lines, directly corresponding to maximized g_2's.

2.4 Effects of Perturbations

Whereas essentially all parameters in Eq. (2.2) can be fine tuned, it is useful to consider effects of perturbations. We consider two types of important perturbations. (a) With increasing U, Eq. (2.6) includes high order terms $n^{s>2}$. (b) An energy mismatch $\Delta(n_1 - n_2)$

breaks the inversion symmetry.

Consider (a), the lowest order contribution is a cubic term and we have $E_n = An + Bn^2 + Cn^3$, where $Cn^3 = -n^3U^2/(8J)$ (see Eq. (2.24)). The wave function is written as

$$|\Psi(t)\rangle = \sum_{n=0}^{n} c_n e^{-\frac{i}{\hbar}(An+Bn^2-\frac{U^2}{8J}n^3)t}, \tag{2.15}$$

where $c_n = (\frac{2}{\pi N})^{\frac{1}{4}} e^{-\frac{1}{N}(n-\frac{N}{2}-\frac{U}{16J}N^2)^2}$. If $\frac{U^2}{8J}n^3t^* \ll 1$ is satisfied, the extra phase introduced by the cubic term is negligible within the time scale that is relevant to the emergent NOON states and DQPTs. Since c_n is a Gaussian with a width $\sqrt{N}$, which provides a natural cutoff of n in the sum in Eq. (2.15), we replace n in the above inequality by $\sqrt{N}$ and obtain $UN^{\frac{3}{2}} \ll J$. Thus, when $UN^2 \ll J$ is satisfied, all these corrections are negligible.

Similar conclusions apply to $n^{s>2}$ caused by multi-body interactions. Interaction induced inter-band couplings may lead to virtual transitions of particles from the lowest energy band to higher bands [85]. When the band gap is small compared to the interaction strength, there exist effective multi-body interactions. As for the three body interaction, $U_3(n_1^3 + n_2^3)$, it can be rewritten as $U_3(n_1 + n_2)^3 - 3U_3n_1n_2(n_1 + n_2)$. Because of the conservation of the total particle number, the first term is not relevant to the dynamics. The second term turns the two-body interaction, U of Eq. (2.2), into $U \to U + 3U_3N$. So it does not change any qualitative results. Other multi-body interactions do not change our results neither, provided that they respect the inversion symmetry. As discussed in Sec. 2.2, NOON states emergent in the dynamics are protected by the inversion symmetry. Any multi-body interactions, $U_{s>2}(n_1^s + n_2^s)$, still respect this symmetry. Thus, the only effect that they have on the dynamics is to add corrections, $n^{s>2}$, to the energy spectrum in Eq. (2.6). Any such small corrections would not affect the qualitative results of the dynamics in short times.

For symmetry-breaking terms in (b), our calculation shows that a finite Δ suppresses g_N by a factor,

$$\frac{g_N}{g_N^0} = 1 - \left(\frac{\Delta^2 N}{2J^2} + \frac{U\Delta N(N-1)}{16J^2}\right), \tag{2.16}$$

where $g_N^0 = N!/2$ is the N-body correlation function of a NOON state. Thus, when

$$8\Delta^2 N + \Delta UN(N-1) \ll 16J^2, \tag{2.17}$$

all characteristic features of NOON states retain.

We compare Eq. (2.17) to the criterion for a stable NOON state at equilibrium [93], where

a finite Δ strongly suppresses the superposition of $|N,0\rangle$ and $|0,N\rangle$, as a large N amplifies the energy penalty. Meanwhile, the effective tunneling between $|N,0\rangle$ and $|0,N\rangle$ is exponentially small, as it requires N steps of single-particle tunneling to couple them. $\Delta N \ll Je^{-N}$ is then required, i.e., an exponentially small Δ with increasing N. Here, such a constraint does not apply in non-equilibrium dynamics. Eq. (2.17) shows that, with increasing N, Δ only needs to be suppressed as a power law. The dynamically generated NOON states are much more stable than their counterparts at equilibrium. Thus, our results suggest a new route to access NOON states that can be potentially used in precision measurements.

2.5 Experimental Realizations and Conclusions

Whereas our results apply to generic atomic interferometers with any particle number, we comment on possible sceneries directly related to current experiments. Two coupled optical tweezers have been used to create an atomic Hong-Ou-Mandel interferometer [3, 4]. Each single tweezer corresponds to a quantum state in Eq. (2.2), and both the interaction U and tunneling J can be tuned. Starting from an initial state, $|2,0\rangle$, i.e., two bosons occupy the same optical tweezer, the time evolution of the correlation functions can be calculated analytically,

$$g_1 = -\frac{2U}{\sqrt{16J^2+U^2}}\alpha\beta\sin^2\frac{\sqrt{16J^2+U^2}t}{2\hbar} + i2\alpha\beta\sin\frac{\sqrt{16J^2+U^2}t}{2\hbar}\cos\frac{Ut}{2\hbar} \tag{2.18}$$

$$g_2 = \frac{\alpha^4+\beta^4-1}{2} + \alpha^2\beta^2\cos\frac{\sqrt{16J^2+U^2}t}{\hbar} + i\left(\sin\frac{Ut}{2\hbar}\cos\frac{\sqrt{16J^2+U^2}t}{2\hbar} - \frac{U}{\sqrt{16J^2+U^2}}\cos\frac{Ut}{2\hbar}\sin\frac{\sqrt{16J^2+U^2}t}{2\hbar}\right), \tag{2.19}$$

$$\alpha = \frac{1}{\sqrt{2}}\sqrt{1-\frac{U}{\sqrt{16J^2+U^2}}},\ \beta = \frac{1}{\sqrt{2}}\sqrt{1+\frac{U}{\sqrt{16J^2+U^2}}}. \tag{2.20}$$

If the parameters are fine tuned such that $\frac{\sqrt{16J^2+U^2}}{U} = 2k, k\in\mathbb{Z}$, we obtain, $g_1 = 0, g_2 = i(-1)^k$, and a small NOON state $\frac{|2,0\rangle+i(-1)^k|0,2\rangle}{\sqrt{2}}$ at $t = \frac{\pi\hbar}{U}$. Using realistic experimental parameters in Ref. [4], $J/2\pi = 262(4)$Hz and $U/J = 0.22(2)$, the correlation functions and the zeros of $G(z)$ are displayed in Fig. 2.5. When $U \ll J$, $\frac{\sqrt{16J^2+U^2}}{U} = 2k$ corresponds to the condition $r = r_m$ in Sec. 2.2. Without fine tuning experimental parameters, there are corrections to the small NOON state at t^*, similar to the results discussed in the previous sections. It is worth mentioning that, starting from $|1,1\rangle$, the current experiment has shown

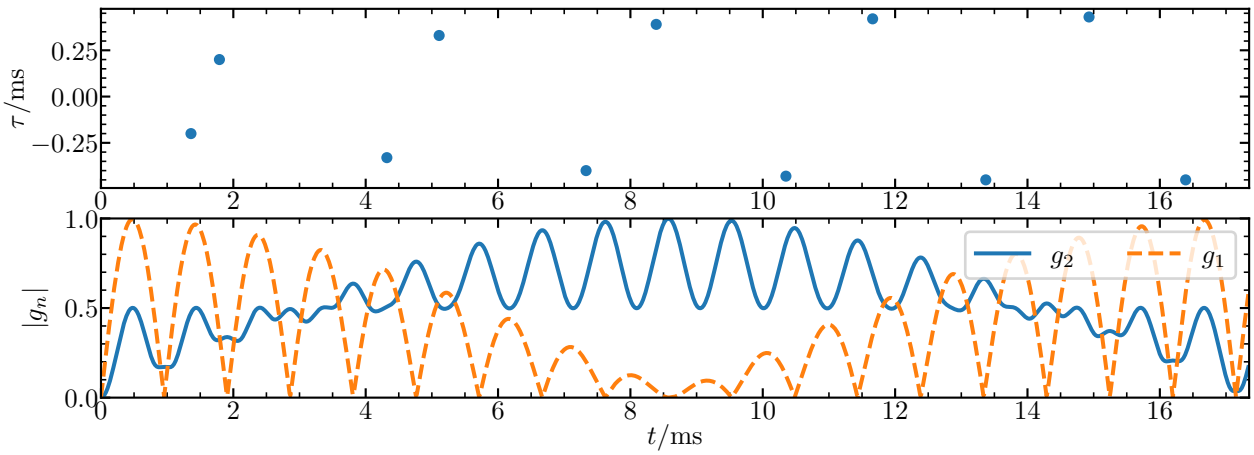

Figure 2.5: Zeros of $G(z)$ in the complex plane and normalized correlation functions for 2 particles in optical tweezers. $U/J = 0.22$ and $J/2\pi = 262$Hz.

that a small NOON state can be produced in a Hong-Ou-Mandel interferometer. However, this is only true when interactions are ignored. We have verified that, in the presence of interactions, $|1,1\rangle$ cannot produce an exact small NOON state. Instead, $|2,0\rangle$ should be used, as shown by the previous discussions.

It is possible that optical tweezers could trap multiple particles [2, 94]. For 8 particles, $UN^2 \ll J$ is no longer satisfied if $U/J = 0.22(2)$. Nevertheless, qualitative results remain unchanged. As shown in Fig. 2.6, g_8 is maximized near t^* while other correlation functions are suppressed. With U/J decreased down to 0.022, all results in the previous sections are recovered and the predicted NOON states and DQPTs can be observed around $t = 86$ms.

Beside optical tweezers, other systems ranging from double-well optical lattices to mesoscopic traps [95–98], in which the total particle number can be controlled precisely, are also suitable for testing our theoretical results. In addition, H in Eq. (2.2) can be mapped to a spin-1/2 model with all-to-all interactions [37], which offers another realization of our schemes in spin systems.

Conclusions. We have studied DQPTs in interacting atomic interferometers and shown that dynamically generated entangled states have deep connections with zeros of Loschmidt echo in the complex plane. DQPTs provide us with a new angle to understand non-equilibrium dynamics. We hope that our work will stimulate more interests of using interacting interferometers to explore DQPTs and to produce novel entangled quantum states.

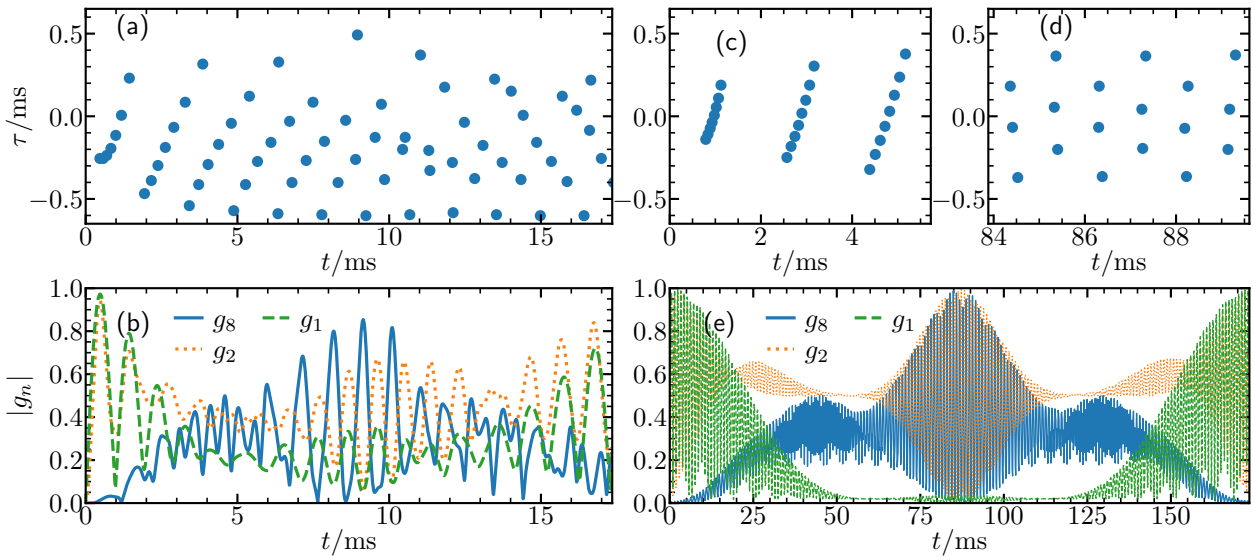

Figure 2.6: Zeros of $G(z)$ in the complex plane and normalized correlation functions for 8 particles in optical tweezers. $J/2\pi = 262$Hz. (a,b): $U/J = 0.22$. (c-e): $U/J = 0.022$.

2.6 Appendix

2.6.1 Eigenstates and energy spectrum of the Hamiltonian

We consider the Hamiltonian

$$\hat{H} = -J(\hat{a}_1^\dagger \hat{a}_2 + \hat{a}_2^\dagger \hat{a}_1) + \frac{\bar{U}}{2}(\hat{n}_1 + \hat{n}_2)^2 + \frac{U}{4}(\hat{n}_1 - \hat{n}_2)^2 + \Delta(\hat{n}_1 - \hat{n}_2).$$

When $U = \Delta = 0$, the eigenenergies E_n^0 and eigenstates $|E_n^0\rangle$ are

$$E_n^0 = 2J(n - \frac{N}{2}), \tag{2.21}$$

$$\left|E_n^0\right\rangle = \frac{1}{\sqrt{n!(N-n)!}}(\frac{\hat{a}_1^\dagger + \hat{a}_2^\dagger}{\sqrt{2}})^{N-n}(\frac{\hat{a}_1^\dagger - \hat{a}_2^\dagger}{\sqrt{2}})^n \left|0\right\rangle . \tag{2.22}$$

When $U, \Delta \ll J$, the first and second order corrections to the eigenenergies are

$$E_n^1 = \frac{U}{4}(2nN - 2n^2 + N), \tag{2.23}$$

$$E_n^2 = \frac{U^2}{32J}(2n - N)(N - 1 + 2Nn - 2n^2) + \frac{\Delta^2}{2J}(2n - N). \tag{2.24}$$

The eigenstates are

$$
\begin{aligned}
|E_n\rangle = &\left|E_n^0\right\rangle - \frac{\Delta}{2J}\sqrt{(n+1)(N-n)}\left|E_{n+1}^0\right\rangle + \frac{\Delta}{2J}\sqrt{n(N-n+1)}\left|E_{n-1}^0\right\rangle \\
&- \frac{U}{4}\frac{\sqrt{(N-n)(N-n-1)(n+1)(n+2)}}{4J}\left|E_{n+2}^0\right\rangle \\
&+ \frac{U}{4}\frac{\sqrt{(n-1)n(N-n+1)(N-n+2)}}{4J}\left|E_{n-2}^0\right\rangle .
\end{aligned}
\tag{2.25}
$$

2.6.2 Analyses of perturbations

When $\Delta = 0$, the initial state $|N,0\rangle$ can be expanded by energy eigenstates and the coefficients c_n are

$$
\begin{aligned}
|c_n|^2 = |\langle E_n|N,0\rangle|^2 &= \left|\frac{1}{2^{N/2}}\sqrt{\frac{N!}{n!(N-n)!}}\left(1-(N-2n)\frac{U(N-1)}{16J}\right)\right|^2 \\
&\approx \sqrt{\frac{2}{\pi N}}e^{-\frac{2}{N}\left(n-\frac{N}{2}-\frac{UN(N-1)}{16J}\right)^2}.
\end{aligned}
\tag{2.26}
$$

Assuming $E_n = Cn^3 + Bn^2 + An$ and $B < 0$, the overlap between $|\psi_t\rangle$ and the NOON state $(|N,0\rangle + i\,|0,N\rangle)/\sqrt{2}$ is

$$
\begin{aligned}
\langle C_+|\psi(t)\rangle &= \sum_{n=0}^{N}|c_n|^2 e^{-i(\frac{\pi}{2}n^2+n\pi)}e^{-\frac{i}{\hbar}E_n t} \\
&= \sum_m \sqrt{\frac{2}{\pi N}}e^{-\frac{2}{N}m^2-\frac{iCt}{\hbar}m^3-i(\frac{\pi}{2}-H_2 t)m^2+i(G_1-\pi-H_1 t)m},
\end{aligned}
\tag{2.27}
$$

where $m = n - \frac{N}{2} + \frac{UN^2}{16J}$ and

$$
H_2 = \frac{|B|}{\hbar} - \frac{3CN^2U}{16\hbar J} - \frac{3CN}{2\hbar}, \tag{2.28}
$$

$$
H_1 = \frac{A}{\hbar} - \frac{|B|N^2U}{8\hbar J} - \frac{|B|N}{\hbar} + \frac{3CN^4U^2}{256\hbar J^2} + \frac{3CN^3U}{16\hbar J} + \frac{3CN^2}{4\hbar}, \tag{2.29}
$$

$$
G_1 = -\frac{\pi N^2 U}{16J} - \frac{\pi N}{2}. \tag{2.30}
$$

What is required is that the phase contributed by the cubic term is negligible when $t \sim \frac{\pi\hbar}{U}$. Since the width of the gaussian factor is $\sqrt{N}$, we require

$$
\left|\frac{Ct}{\hbar}m^3\right| = \left|\frac{U^2}{8J}\frac{\pi}{U}N^{3/2}\right| \ll 1 \Rightarrow \left|\frac{UN^{3/2}}{J}\right| \ll 1, \tag{2.31}
$$

where we have used the energy spectrum obtained from second order perturbation. The cubic term is then dropped and we employ Poisson summation formula to obtain

$$\langle C_+|\psi(t)\rangle = \sum_k \sqrt{\frac{1}{1+i\frac{N}{2}(G_2-H_2t)}}\exp\left(-\frac{1}{\frac{2}{N}+i(G_2-H_2t)}\left(\frac{(2k-1)\pi+G_1}{H_1}-t\right)^2\frac{H_1^2}{4}\right). \tag{2.32}$$

Similarly, we obtain

$$\langle C_-|\psi(t)\rangle = \sum_k \sqrt{\frac{1}{1+i\frac{N}{2}(G_2-H_2t)}}\exp\left(-\frac{1}{\frac{2}{N}+i(G_2-H_2t)}\left(\frac{(2k)\pi+G_1}{H_1}-t\right)^2\frac{H_1^2}{4}\right). \tag{2.33}$$

When Eq. (2.31) is satisfied, $H_2 \approx \frac{|B|}{\hbar} \approx \frac{U}{2\hbar}$, $H_1 \approx \frac{A}{\hbar} \approx \frac{2J}{\hbar}$, and $G_1 \approx -\frac{\pi N}{2}$. We define the probability of finding a NOON state as $Q(t) = \max(|\langle C_+|\psi(t)\rangle|^2, |\langle C_-|\psi(t)\rangle|^2)$. Near $t = \frac{G_2}{H_2}$, $Q(t)$ can be written as

$$Q(t) \approx \sqrt{\frac{1}{1+\frac{N^2}{4}(\frac{\pi}{2}-\frac{U}{2\hbar}t)^2}}\sum_k \left|\exp\left(-\frac{1}{\frac{2}{N}+i(\frac{\pi}{2}-\frac{U}{2\hbar}t)}\left(\frac{k\pi\hbar}{2J}-\frac{\pi N\hbar}{4J}-t\right)^2\frac{J^2}{\hbar^2}\right)\right|^2. \tag{2.34}$$

$Q(t)$ consists of multiple gaussian functions whose peaks are located at $t = \frac{k\pi\hbar}{2J} - \frac{\pi N\hbar}{4J}, k \in \mathbb{Z}$, and their separation is $\frac{\pi\hbar}{2J}$. There is also a factor $(1+\frac{N^2}{4}(\frac{\pi}{2}-\frac{U}{2\hbar}t)^2)^{-1/2}$, which suppresses peak heights. If the parameters are fine tuned such that an integer k_0 satisfies $\frac{\pi}{2}-\frac{U}{2\hbar}(\frac{k_0\pi\hbar}{2J}-\frac{\pi N\hbar}{4J}) = 0$, then $Q(t) = 1$ at $t = \frac{k_0\pi\hbar}{2J} - \frac{\pi N\hbar}{4J}$. We thus obtain a perfect NOON state. Without fine tuning the parameters, we consider $t = \frac{\pi\hbar}{U}$ that lies in the middle of two peaks. The two peaks get a suppression of $(1+(\frac{\pi NU}{16J})^2)^{-1/2}$. Again, because of Eq. (2.31), this factor is negligible when N is large.

If the energy mismatch Δ is finite, we separate the eigenstates into two parts according to their spatial parity,

$$|E_n\rangle = \alpha_n |E_n\rangle_s + \beta_n |E_n\rangle_a, \tag{2.35}$$

$$\hat{P}|E_m\rangle = \alpha_n(-1)^n |E_n\rangle_s + \beta_n(-1)^{n+1}|E_n\rangle_a. \tag{2.36}$$

The time evolution of the wave function is written as

$$|N,0\rangle \to |\psi_t\rangle = \sum_{n=0}^{N} c_n\alpha_n e^{-iE_nt}|E_n\rangle_s + c_n\beta_n e^{-iE_nt}|E_n\rangle_a.$$

From Eq. (2.24), we see that, up to the second order of Δ, the quadratic term in E_n remains

unchanged. Thus, when $t^* = \frac{\pi\hbar}{U}$, $e^{-iE_n t^*} = \frac{1+i(-1)^n}{\sqrt{2}}$ is satisfied, and we obtain

$$|\psi(t^*)\rangle = \sum_{n=0}^{N} \alpha_n c_n \frac{1+i(-1)^n}{\sqrt{2}} |E_n\rangle_s + \beta_n c_n \frac{1+i(-1)^n}{\sqrt{2}} |E_n\rangle_a = |\text{cat}\rangle + |\text{err}\rangle\,, \tag{2.37}$$

where $|\text{err}\rangle = \sum_{n=0}^{N} i\sqrt{2}(-1)^n c_n \beta_n |E_n\rangle_a$ is the correction to the NOON state at t^*, and

$$g_N = \langle\psi_{t^*}| \hat{a}_1^{\dagger N}\hat{a}_2^N |\psi_{t^*}\rangle = g_N^0 + \frac{N!}{\sqrt{2}} \langle 0, N|\text{err}\rangle + i\frac{N!}{\sqrt{2}} \langle \text{err}|N, 0\rangle + \langle \text{err}| \hat{a}_1^{\dagger N}\hat{a}_2^N |\text{err}\rangle\,. \tag{2.38}$$

Using Eq. (2.25), we obtain

$$\beta_n |E_n\rangle_a = -\frac{\Delta}{2J}\sqrt{(n+1)(N-n)}\left|E_{n+1}^0\right\rangle + \frac{\Delta}{2J}\sqrt{n(N-n+1)}\left|E_{n-1}^0\right\rangle. \tag{2.39}$$

Up to the first order of U and Δ,

$$|\text{err}\rangle^{(1)} = \frac{\Delta}{2J}\sum_{n=0}^{N} i\sqrt{2}\frac{(-1)^{n+1}}{2^{N/2}}\sqrt{\frac{N!}{n!(N-n)!}}(N-2n)\left|E_n^0\right\rangle. \tag{2.40}$$

It is straightforward to verify that $\langle 0, N|\text{err}\rangle^{(1)}$, $\langle \text{err}|^{(1)} |N, 0\rangle$, and $\hat{a}_1^{\dagger N}\hat{a}_2^N |\text{err}\rangle^{(1)}$ vanish. Then we have to go to the second order of U and Δ,

$$|\text{err}\rangle^{(2)} = \frac{\Delta}{2J}\left(\frac{\Delta}{2J} + \frac{U(N-1)}{16J}\right)\sum_{n=0}^{N} i\sqrt{2}\frac{(-1)^{n+1}}{2^{N/2}}\sqrt{\frac{N!}{n!(N-n)!}}(N-2n)^2\left|E_n^0\right\rangle, \tag{2.41}$$

So,

$$\langle 0, N|\text{err}\rangle^{(2)} = -i\sqrt{2}\frac{\Delta}{2J}\left(\frac{\Delta}{2J} + \frac{U(N-1)}{16J}\right)\frac{N!}{(N-1)!}, \tag{2.42}$$

$$\langle \text{err}|^{(2)} |N, 0\rangle = 0. \tag{2.43}$$

Therefore,

$$\begin{aligned} g_N &= \langle\psi(t^*)| \hat{a}_1^{\dagger N}\hat{a}_2^N |\psi(t^*)\rangle = i\frac{N!}{2} - i\left(\frac{\Delta}{2J}\left(\frac{\Delta}{2J} + \frac{U(N-1)}{16J}\right)\right)\frac{N!^2}{(N-1)!} \\ &= g_N^0\left(1 - 2N\left(\frac{\Delta}{2J}\left(\frac{\Delta}{2J} + \frac{U(N-1)}{16J}\right)\right)\right). \end{aligned} \tag{2.44}$$

2.6.3 Results for attractive interactions and odd number of particles

Attractive interactions As discussed in the main text, when $U > 0$, $t^* = \frac{\pi\hbar}{U}$, and $r_m = 4m$, $|C_-\rangle$, $|P_-\rangle$, $|C_+\rangle$, and $|P_+\rangle$ show up in order starting from t^*. In contrast, $r_m = 4m+2$, $|C_+\rangle$, $|P_+\rangle$, $|C_-\rangle$, and $|P_-\rangle$ show up in order starting from t^*.

Here we discuss $U<0$ and $t^*=\frac{\pi\hbar}{|U|}$.

- For $r_m=4m$, $|C_+\rangle$, $|P_+\rangle$, $|C_-\rangle$, and $|P_-\rangle$ show up in order starting from t^*, and $G(z)=\frac{1}{\sqrt{2}}((\cos J(z-t^*)/\hbar)^N+i(i\sin J(z-t^*)/\hbar)^N)$.
- For $r_m=4m+2$, $|C_-\rangle$, $|P_-\rangle$, $|C_+\rangle$, and $|P_+\rangle$ show up in order starting from t^*, and $G(z)=\frac{1}{\sqrt{2}}((\cos J(z-t^*)/\hbar)^N-i(i\sin J(z-t^*)/\hbar)^N)$.

If r_m is not an even integer, Eq. (2.11) can be generalized to

$$Q(t)\approx\sqrt{\frac{1}{1+\frac{N^2}{4}(\frac{\pi}{2}-\frac{|U|}{2\hbar}t)^2}}\sum_k\left|\exp\left(-\frac{1}{\frac{2}{N}+i\frac{U}{|U|}(\frac{\pi}{2}-\frac{|U|}{2\hbar}t)}(\frac{k\pi}{2}-\frac{\pi N}{4}-\frac{Jt}{\hbar})^2\right)\right|^2. \tag{2.45}$$

Odd number of particles The zeros of $G(z)=\frac{1}{\sqrt{2}}((\cos J(z-t^*)/\hbar)^N\pm i(i\sin J(z-t^*)/\hbar)^N)$ are written as

$$\mathrm{Re}\,\frac{J(z-t^*)}{\hbar}=\frac{\pi}{4}+\frac{l}{2}\pi, l\in\mathbb{Z}, \tag{2.46}$$

$$\mathrm{Im}\,\frac{J(z-t^*)}{\hbar}=\frac{1}{2}\,\mathrm{arcosh}\,\frac{1}{|\cos\pi(\frac{1+2k\mp1/2}{N}-\frac{1}{2})|}\,\mathrm{sgn}\sin\pi\left(\frac{1+2k\mp1/2}{N}-\frac{1}{2}\right), \tag{2.47}$$

$k=1,2,...,N$.

For a finite even N, zeros have finite imaginary parts. For a finite odd N, some zeros reside on the real time axis, as shown in Fig. 2.7.

In the large N limit:

- If N is even,
$$\lim_{N\to\infty}\lambda(t)=-2\ln[\max(|\cos J\tilde{t}/\hbar|,|\sin J\tilde{t}/\hbar|)],$$
which has been analyzed in the main text.
- If N is odd,
$$\lambda_\pm(t)=-\frac{1}{N}\ln\left(\frac{1}{2}|\cos^N J\tilde{t}/\hbar\pm\sin^N J\tilde{t}/\hbar|^2\right).$$
The sign $\pm$ is determined by the sign before i in $G(t)$ and whether $N=4p+1$ or $4p+3$, $p\in\mathbb{Z}$. $\lambda_\pm(t)$ is nonanalytic at $\tilde{t}_c=\frac{\hbar}{J}(\frac{\pi}{4}+k\frac{\pi}{2}), k\in\mathbb{Z}$, when $N\to\infty$. Especially,
$$\lim_{N\to\infty}\lambda_-(t)=-2\ln[\max(|\cos J\tilde{t}/\hbar|,|\sin J\tilde{t}/\hbar|)]$$
except at $\tilde{t}_{c1}=\frac{\hbar}{J}(\frac{\pi}{4}+k\pi), k\in\mathbb{Z}$. As shown in Fig. 2.7(d), $\lambda_-(t)$ diverges at $\tilde{t}_{c1}$ for any finite odd N. Similar conclusions apply to $\lambda_+(t)$.

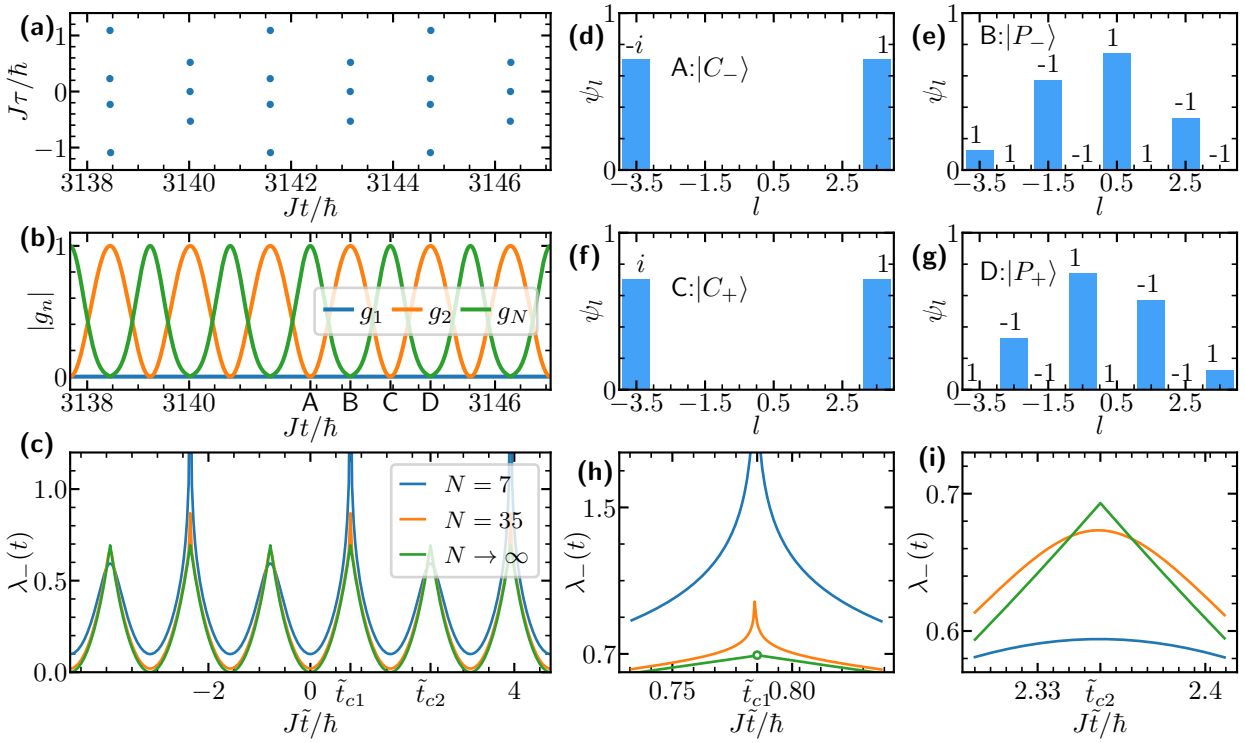

Figure 2.7: (a) Zeros of $G(z)$ in the complex plane of time for 7 particles. (b) The corresponding normalized correlation functions along the real time axis in (a). (d-g) The wave functions at four times picked up from (b). (c) The rate function $\lambda_-(t)$. (h) and (i) show details of $\lambda_-(t)$ near t_c. The hollow dot in (h) represents the discontinuity of $\lambda_-(t)$ at $\tilde{t}_{c1}$ where it approaches infinity. In all panels U and J are fine tuned such that $|\psi(t^*)\rangle = |C_-\rangle$.

The emerged pair condensates near t^* for odd N are also different from those for even N, Using Eq. (2.5), for $N = 2m+1, m \in \mathbb{Z}$, we obtain,

$$|P_-\rangle = \sum_{n=0}^{N} \frac{i^{N-n} - i^{n+1}}{p_n} \hat{a}_1^{\dagger n} \hat{a}_2^{\dagger N-n} |0\rangle = \sum_{n=0}^{N} \frac{i^{n+1}((-1)^{m+n} - 1)}{p_n} \hat{a}_1^{\dagger n} \hat{a}_2^{\dagger N-n} |0\rangle , \tag{2.48}$$

$$|P_+\rangle = \sum_{n=0}^{N} \frac{i^{N-n} + i^{n+1}}{p_n} \hat{a}_1^{\dagger n} \hat{a}_2^{\dagger N-n} |0\rangle = \sum_{n=0}^{N} \frac{i^{n+1}((-1)^{m+n} + 1)}{p_n} \hat{a}_1^{\dagger n} \hat{a}_2^{\dagger N-n} |0\rangle . \tag{2.49}$$

Thus, some Fock states are suppressed by the factor $(-1)^{m+n} - 1$. For instance when $N = 7$, $|P_-\rangle$ only contains $|0,7\rangle, |2,5\rangle, |4,3\rangle, |6,1\rangle$. Apparently both one-body correction g_1 and $G(t) = \langle 7,0|P_-\rangle$ vanishes.

3. DISCRETE TIME CRYSTAL STABILIZED BY ALL-TO-ALL INTERACTIONS

This chapter is based on the published article [99] by C. Lyu, S. Choudhury, C. Lv, Y. Yan, and Q. Zhou, Eternal discrete time crystal beating the Heisenberg limit, Phys. Rev. Research ***2****, 033070 (2020).*

A discrete time crystal (DTC) [30–40] repeats itself with a rigid rhythm, mimicking a ticking clock set by the interplay between its internal structures and an external force. DTCs promise profound applications in precision timekeeping and other quantum techniques. However, it has been facing a grand challenge of thermalization. The periodic driving may continuously pump energies into a discrete time crystal and heat it up to the infinite temperature eventually [100–102]. A number of schemes have been proposed to slow down the thermalization, such as the many-body localization (MBL) [31–33] and the Floquet prethermalization [36]. Compared with other schemes only retaining the coherence of DTCs within certain time scales, MBL is of particular interest. Disorder breaks an interacting system into localized l-bits to encode the memory of the initial state [103], and suppresses thermalization up to an arbitrarily long time scale. However, most studies have considered homogeneous drivings so far. In practice, the driving field may vary across a DTC and local perturbations may further amplify the spatial inhomogeneities, both preventing individual constituents of the DTC from synchronization and impeding applying DTCs in quantum technologies. Whereas MBL could stabilize a DTC against weak inhomogeneous perturbations to π-rotations [104], it is no longer powerful in the presence of strong inhomogeneities, as the exponentially decayed couplings between l-bits in MBL have readily weakened the synchronization between remote parts of a DTC in spite of the presence of interactions.

Fundamental questions naturally arise. (1) How to access a DTC that could maintain quantum coherence and quantum synchronization in the presence of arbitrarily strong inhomogeneous driving fields and local perturbations? (2) Furthermore, how to implement such a DTC to promote the precision of quantum metrology?

In this chapter, we present a new type of DTC that has a number of unique features distinct from previously studied ones. DTCs in the literature survive a small deviation of the driving fields from uniform π pulses. In contrast, our DTC is stable against arbitrarily strong perturbations in both homogeneous and inhomogeneous pulses. It could also start from any initial state, not necessarily a superposition of only two eigenstates of the Floquet

operator [33]. Meanwhile, the hypersensitivity of our DTC to interaction strength makes it a promising quantum device to measure interactions beyond the Heisenberg limit, unlike other DTCs not sensitive to interactions within a finite range.

3.1 Quantum Revival of Spins with All-to-All Interactions

We consider N spin-1/2s described by a Hamiltonian, $H = H_{\text{int}} + \sum_n H_{\text{pul}}\delta(t - nT)$, where

$$H_{\text{int}} = 2J \sum_{i<j} S_i^z S_j^z, \quad H_{\text{pul}} = \sum_i^N \theta_i S_i^y. \tag{3.1}$$

As shown in Fig. 3.1(a), J is the strength of an all-to-all interaction, which has been considered in the Lipkin-Meshkov-Glick model [105]. $\vec{S}_i = \frac{1}{2}\vec{\sigma}_i$ and $\vec{\sigma}_i$ are Pauli matrices (we have set $\hbar = 1$). H_{pul} represents periodic pulses applied on spins. θ_i determines the angle rotated by the ith spin about the y-axis. The dependence of θ_i on i characterizes the spatial inhomogeneity of pulses. In the time evolution, H_{int} and H_{pul} control the dynamical phases and the geometric phases respectively, both of which depend on the number of spin excitations. As shown later, the interplay of H_{int} and H_{pul} will lead to a perfect revival of the initial state. Eq. (3.1) can be realized using spin-1/2s coupled to a cavity or a waveguide [106, 107], or particles with long-range interactions whose ranges are much larger than the system size. The equivalence between spin-1/2s and bosons also provides a natural realization of such interaction [37].

We prove that, when $JT = \pi$ is satisfied, any initial state returns to itself at $t = 2nT^-$ for any even $N \in 2\mathbb{Z}$ and any θ_i as an arbitrary function of i. t^- (t^+) denotes the time right before (after) a pulse is applied. This perfect revival delivers an eternal DTC that evades thermalization and is equipped with a strong synchronization even in the presence of a noisy environment. Previous works on normalized all-to-all interactions have considered the small J limit of Eq. (3.1) [37], not the optimal choice of JT discussed here.

Consider an initial state with m spin-ups and $N - m$ spin-downs, $|\Psi(0^-)\rangle = \prod_i |\eta\rangle_i$, where $\eta = \uparrow, \downarrow$. After the first pulse,

$$|\uparrow\rangle_i \to +\cos\left(\frac{\theta_i}{2}\right)|\uparrow\rangle_i + \sin\left(\frac{\theta_i}{2}\right)|\downarrow\rangle_i, \tag{3.2}$$

$$|\downarrow\rangle_i \to -\sin\left(\frac{\theta_i}{2}\right)|\uparrow\rangle_i + \cos\left(\frac{\theta_i}{2}\right)|\downarrow\rangle_i, \tag{3.3}$$

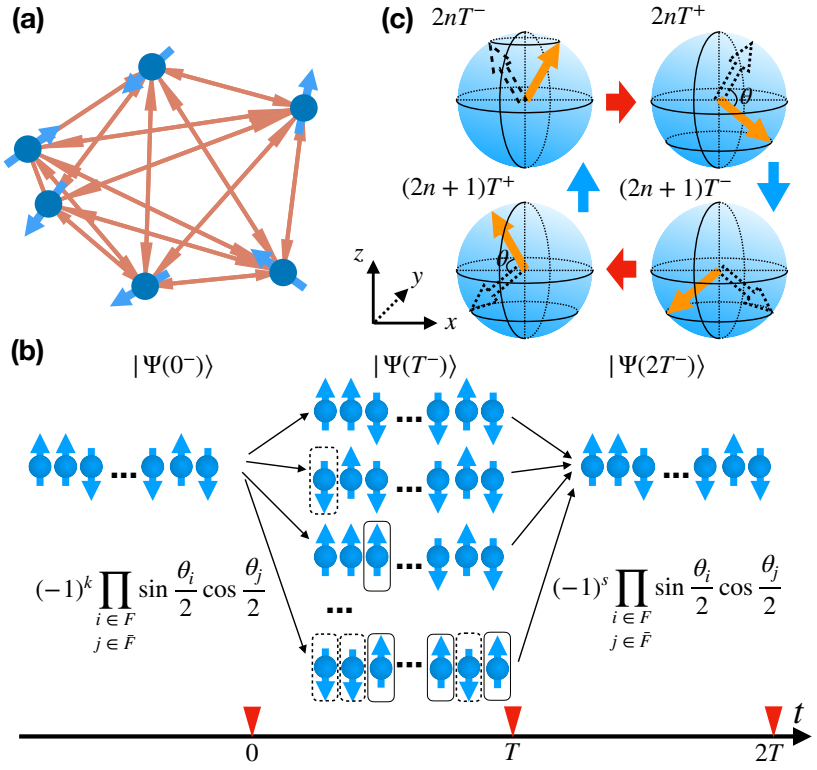

Figure 3.1: A DTC induced by an all-to-all interaction. (a)All-to-all interactions (brown arrows) between spin-1/2s (blue spheres attached to arrows). (b)A perfect revival of an arbitrary initial state due to constructive interference among all pathways. Dashed and solid boxes highlight the k spin-ups and s spin-downs flipped by the first pulse, leading to geometric phases, $(-1)^k$ and $(-1)^s$, respectively. Triangles on the time axis represent H_{pul}. (c)Rotations of a spin-L (yellow arrow) on the Bloch sphere. When $JT = \pi$, the non-linear term, JL_z^2, leads to an effective π rotation about the z axis between $2nT^+$ and $(2n+1)T^-$ such that any initial state returns to itself after $2T$ for any θ.

$|\Psi(0^+)\rangle$ becomes a superposition of 2^N states, each of which is obtained from flipping s spin-ups and k spin-downs of $|\Psi(0^-)\rangle$, as shown in Fig. 3.1(b). Each state acquires a dynamical phase, $e^{-i\varphi_1}$, imposed by H_{int} from $t = 0^+$ to $t = T^-$. The second pulse flips the spins again, followed by H_{int} imposing another dynamical phase, $e^{-i\varphi_2}$, from $t = T^+$ to $t = 2T^-$, and

$$\left|\Psi(2T^-)\right\rangle = A\left|\Psi(0^-)\right\rangle + ..., \tag{3.4}$$

where "..." represents states different from $|\Psi(0^-)\rangle$.

To return to $|\Psi(0^-)\rangle$, the s (k) spin-ups (spin-downs) flipped by the first pulse need to be flipped back to spin-ups (spin-downs) during the second pulse. 2^N such pathways allow the system to come back to $|\Psi(0^-)\rangle$. The contribution to A from each pathway is written as $(-1)^{k+s}\prod_{j\in\bar{F}}\cos^2(\frac{\theta_j}{2})\prod_{i\in F}\sin^2(\frac{\theta_i}{2})$, where $(-1)^{k+s}$ comes from flipping $k+s$ spin-1/2s twice, equivalent to the geometric phase from rotating these spins about the y axis for 2π. F ($\bar{F}$) denotes the collection of flipped (unflipped) spins. As each of these 2^N states is an eigenstate of H_{int}, $\varphi_1 = (m-s+k)(m-s+k-N)\pi$, and $\varphi_2 = m(m-N)\pi$ when $JT = \pi$. m-independent terms have been dropped. The total dynamical phase accumulated from 0^- to $2T^-$ is $e^{-i(\varphi_1+\varphi_2)} = e^{i\pi\{2[m^2+m(k-s-N)-ks]+N(s-k)+k^2+s^2\}} = (-1)^{k+s}$. We have used $N \in 2\mathbb{Z}$, and $e^{iZ^2\pi} = e^{iZ\pi} = (-1)^Z$ for any integer Z. This dynamical phase factor cancels exactly the previously obtained geometric phase, and thus $A = \sum_F \prod_{j\in\bar{F}}\cos^2(\frac{\theta_j}{2})\prod_{i\in F}\sin^2(\frac{\theta_i}{2})$. $\sum_F$ denotes the sum over all 2^N choices of flipping the N spins in $|\Psi(0^-)\rangle$. Since F is an arbitrary choice from the N spins,

$$A = \prod_i(\sin^2(\frac{\theta_i}{2}) + \cos^2(\frac{\theta_i}{2})) = 1. \tag{3.5}$$

These discussions apply to any initial product state and any $t \in [2nT^-, 2(n+1)T^-]$. Thus, any initial state returns to itself at $t = 2nT^-$. Unlike traditional spin-echo schemes using tailored pulses to restore quantum coherence [108], we implement interactions, one source of the decoherence, to overcome the other, the inhomogeneities, so as to access a perfect dynamical localization, an analogy to the Anderson localization in the Hilbert space [109]. Therefore, this interaction induced spin-echo could be used in a broad class of systems to extend the coherence time.

For spatially uniform pulses, a simpler proof exists. H is rewritten as

$$H_{\text{hom}} = JL_z^2 + \theta L_y\sum_n \delta(t-nT), \tag{3.6}$$

where $\vec{L} = \sum_i \vec{S}_i$. Eq. (3.6) is equivalent to the kicked top model describing a periodically driven spin-L [110], where $L = \frac{N}{2}$. The propagator from $t = 2nT^-$ to $t = 2(n+1)T^-$ is written as

$$\mathcal{U}_{JT}(2T) = e^{-iJTL_z^2} e^{-i\theta L_y} e^{-iJTL_z^2} e^{-i\theta L_y}. \tag{3.7}$$

As $e^{-i\pi L_z^2} = e^{-i\pi L_z}$ applies to any integer L (or even N),

$$\mathcal{U}_{\pi}(2T) = e^{-2i\pi L_z} e^{e^{i\pi L_z}(-i\theta L_y)e^{-i\pi L_z}} e^{-i\theta L_y} = 1. \tag{3.8}$$

As shown by Fig. 3.1(c), any state on the Bloch sphere of a spin-L returns to the original place after $2T$. If N is odd, $e^{-i\pi L_z^2}$ and $e^{-i\pi L_z}$ are no longer identical. Such DTC with a period of $2T$ does not exist. In contrast, if we consider spin-1 instead of spin-1/2 in Eq. (3.1), such even-odd effect is absent, as L is always an integer for both even and odd N.

$\mathcal{U}_{\pi}(2T) = 1$ means that the quasi-energy spectrum of H_{eff}, where $\mathcal{U}_{JT}(2T) = e^{-iH_{\text{eff}}}$, has 2^N degenerate eigenstates. Whereas this looks similar to the non-interacting case when $\theta_i = \pi$, a conceptual difference is that, the degeneracy here is stable against any perturbations in θ_i, unlike non-interacting systems, where any infinitesimal deviation from a homogeneous π-pulse lifts the degeneracy, breaks the integrability, and suppresses DTCs. Similar to other models the period doubling comes from the spontaneous time-translation symmetry breaking [31, 32, 37, 104]. When $JT = \pi$, the Floquet eigenstates are $|\pm\rangle = \frac{1}{\sqrt{2}}|\psi(0)\rangle \pm \frac{1}{\sqrt{2}}\mathcal{U}_{\pi}(T)|\psi(0)\rangle$, where $|\psi(0)\rangle$ is an arbitrary initial state. Equivalently, every state $|+\rangle$ with quasi-energy 0 has a partner $|-\rangle$ with quasi-energy π/T. Choosing the initial state as $|\psi(0)\rangle = \frac{1}{\sqrt{2}}(|+\rangle + |-\rangle)$, the Rabi oscillation between the two Floquet eigenstates leads to a period of $2T$. Previous works have been mainly focusing on uniform π-pulses, where the Floquet eigenstate, $\frac{1}{\sqrt{2}}|\uparrow\uparrow ...\rangle \pm \frac{1}{\sqrt{2}}|\downarrow\downarrow ...\rangle$, is a special case of our results. In particular, results here apply to any uniform and nonuniform pulses and thus are far more general.

3.2 Stability Against Spatial Inhomogeneities

We compare the all-to-all interaction model to the power-law interaction model,

$$H' = H'_{\text{int}} + \sum_n H_{\text{pul}}\delta(t - nT),\ H'_{\text{int}} = 2J\sum_{i<j}\frac{S_i^z S_j^z}{|i-j|^{\alpha}}. \tag{3.9}$$

Starting from $|\Psi(0^-)\rangle = \prod_i |\uparrow\rangle_i$, we compute some quantities for both interactions using exact diagonalization,

$$P(2nT^-) = |\left\langle \Psi(0^-)\middle|\Psi(2nT^-)\right\rangle|^2, \tag{3.10}$$

$$M_z(2nT^-) = 2\left\langle \Psi(2nT^-)\middle| L_z \middle|\Psi(2nT^-)\right\rangle/N, \tag{3.11}$$

$$E(2nT^-) = \left\langle \Psi(2nT^-)\middle| H_{\rm int} \middle|\Psi(2nT^-)\right\rangle, \tag{3.12}$$

$$S(2nT^-) = -{\rm Tr}(\rho_B \ln \rho_B). \tag{3.13}$$

$P(2nT^-)$ characterizes the quantum memory of the initial state, $M_z(2nT^-)$ denotes the z-component of the total spin, $E(2nT^-)$ (or $E'(2nT^-) = \langle\Psi(2nT^-)| H'_{\rm int} |\Psi(2nT^-)\rangle$) captures the absorption of energy, and $S(2nT^-)$ is the bipartite entanglement entropy using ρ_B, the reduced density matrix of half of the system.

When $\theta_i = \bar{\theta}$ for any i, a finite J in Eq. (3.9) restores the quantum coherence, if $\epsilon = \bar{\theta} - \pi$ is small [33–35]. However, with increasing ϵ, both $P(2nT^-)$ and $M_z(2nT^-)$ get suppressed, as depicted in Fig. 3.2(a-d). Meanwhile, Q and S grow quickly, where we have used $Q = \frac{E(2nT^-)-E(0)}{E_\infty - E(0)}$ to characterize the absorption of the energy. $E_\infty = 2^{-N}\sum_j \langle j| H_{\rm int} |j\rangle$ is the energy at the infinite temperature and $|j\rangle$ denotes the 2^N eigenstates of $H_{\rm int}$. These results signify the thermalization at large ϵ.

We further take into account the spatial inhomogeneity. As shown in Fig. 3.2(e-h), we choose a random θ_i from $[\bar{\theta} - w_s, \bar{\theta} + w_s]$ with an equal probability. When w_s is finite, the thermalization becomes even faster and Q approaches 1, indicating that the system thermalizes to the infinite temperature. For power-law interactions, dynamical phases controlled by interactions cannot cancel geometric phases induced by pulses. It is impossible to obtain a constructive interference between all pathways. When $\bar{\theta}$ deviates from π, as shown in Fig. 3.3(a-d), P and M_z are suppressed more quickly and S and Q grow faster than the results of $\bar{\theta} = \pi$. If $\bar{\theta}$ is further decreases down to 0.8π, this tendency continues, showing that the power-interaction cannot synchronize spins when pulses are not uniform.

In contrast, $P(2nT^-)$ and $M_z(2nT^-)$ of the all-to-all interaction are unaffected by w_s and remain unity, and both $Q(2nT^-)$ and $S(2nT^-)$ remain zero, directly reflecting the robustness of this eternal DTC against arbitrarily strong spatial inhomogeneities and representing the most synchronized DTC.

The onsite disorder is often considered in DTC to introduce many-body localization [33–35]. Since the coupling between l-bits decays exponentially with increasing their distance,

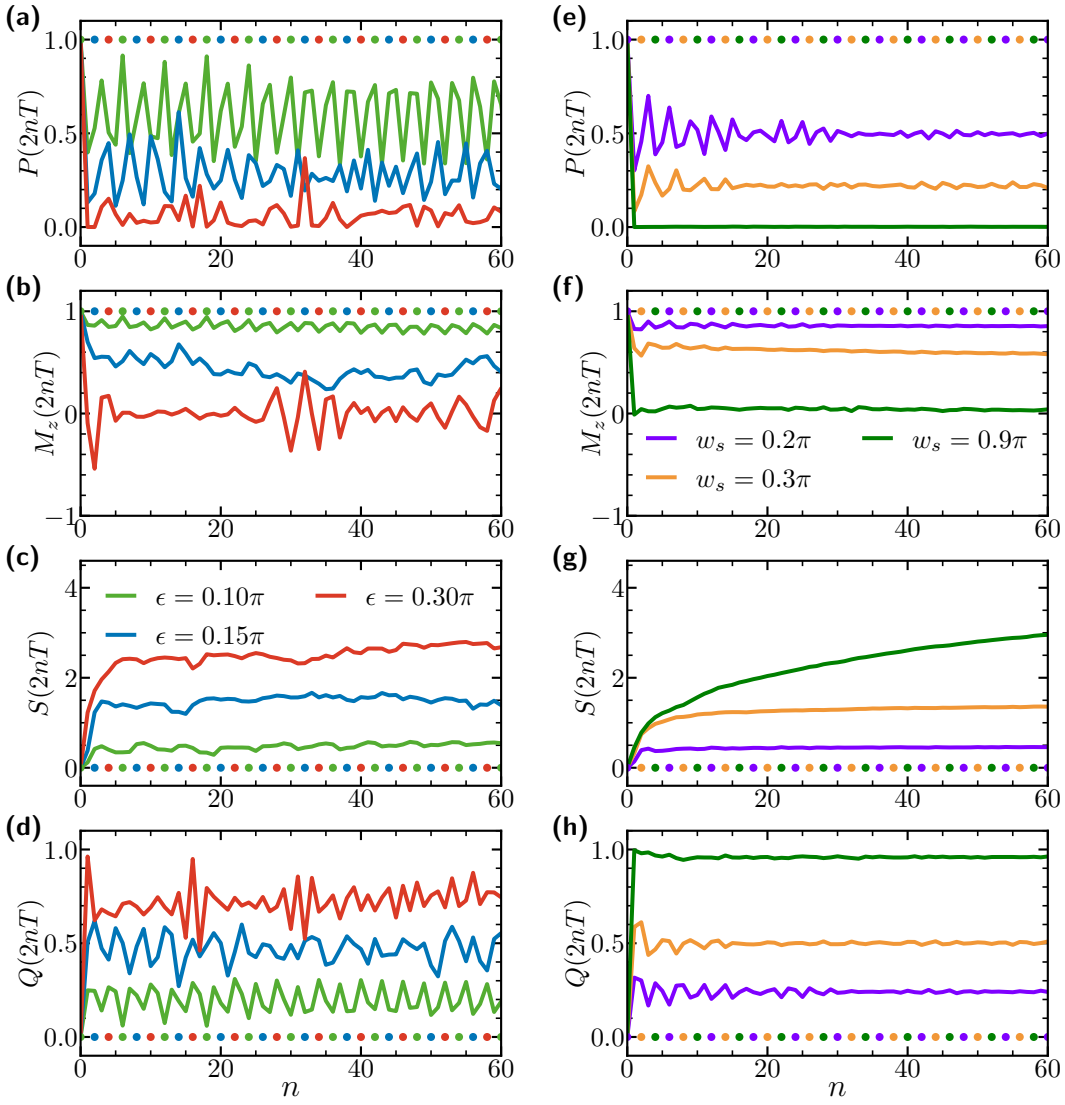

Figure 3.2: Comparison between the all-to-all interaction and a power-law potential with $\alpha = 3$. Here $N = 14$. (a-d) Uniform rotations of spins, $w_s = 0$. The DTC with all-to-all interactions (dots) is unaffected by ϵ, the deviation of $\bar{\theta}$ from π. With the power-law potential (curves), increasing ϵ leads to the suppression of $P(2nT)$ and $M_z(2nT)$, and the growth of $S(2nT)$ and $Q(2nT)$. (e-h) Keeping $\bar{\theta} = \pi$ and increasing the spatial inhomogeneities w_s, the DTC with the power-law potential is suppressed. The DTC with all-to-all interactions remains stable.

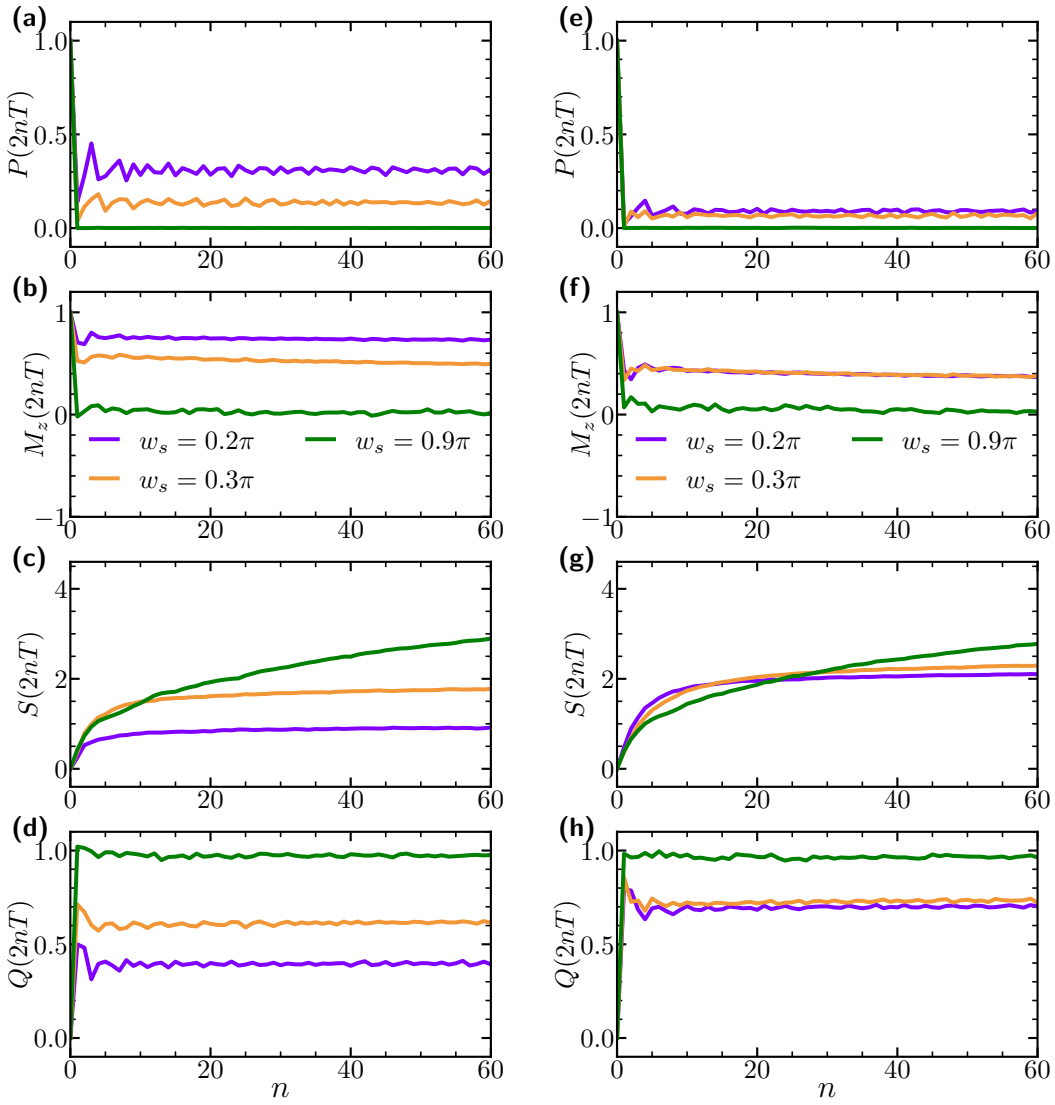

Figure 3.3: Results of inhomogeneities pulses for a power-law potential with $\alpha = 3$. Parameters are the same as Fig. 3.2(e-h), except here in (a-b), $\bar{\theta} = 0.9\pi$ and in (e-h) $\bar{\theta} = 0.8\pi$.

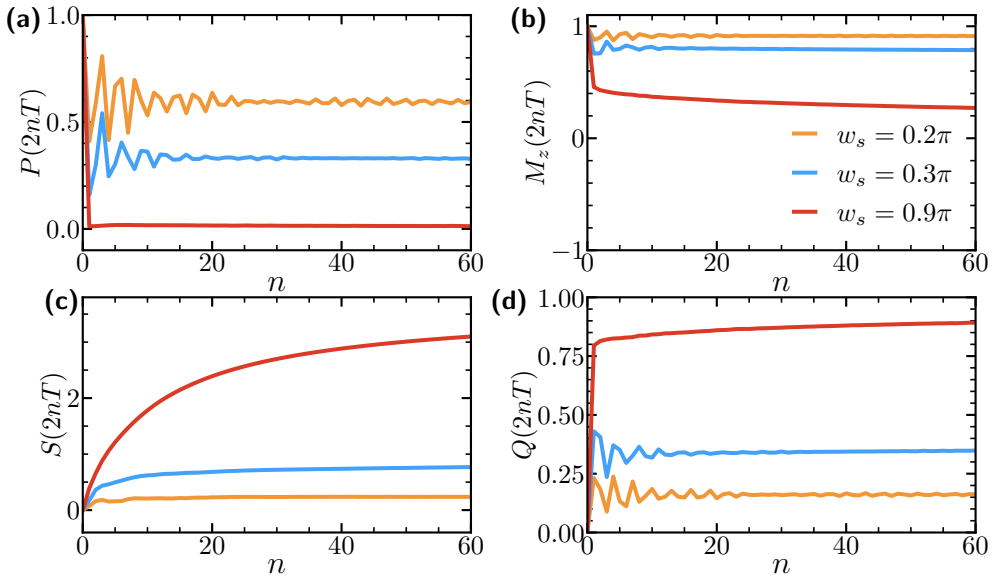

Figure 3.4: Effects of inhomogeneous θ_i on MBL. θ_i is chosen from a uniform distribution $[-w_s + \bar{\theta}, \bar{\theta} + w_s]$. The onsite disorder is chosen from $[0, W]$, where $W = 40J$, $\alpha = 3$, $\bar{\theta} = \pi$, $N = 14$.

this could slow down the thermalization, provided that θ_i is spatially uniform. However, this mechanism of suppressing the thermalization automatically weakens the synchronization between different spatial parts of the system. Thus, when θ_i has strong spatial inhomogeneities, the onsite disorder cannot stabilize the DTC. Consider the Hamiltonian,

$$H = 2J \sum_{i<j} \frac{S_i^z S_j^z}{|i-j|^\alpha} + \sum_n \delta(t - nT) \sum_{i=1}^N \theta_i S_i^y + 2 \sum_{i=1}^N \Delta_i S_i^z, \tag{3.14}$$

where θ_i has a uniform distribution in $[\bar{\theta} - w_s, \bar{\theta} + w_s]$, similar to Fig. 3.2. The onsite disorder, Δ_i, has a uniform distribution in $[0, W]$. As shown in Fig. 3.4, for a given W, with increasing w_s, $P(2nT)$ and $L_z(2nT)$ are suppressed down to zero. Meanwhile, the entropy $S(2nT)$ and $Q(2nT)$ grow faster, signifying the thermalization of the DTC.

3.3 Applications in Precision Measurement

As aforementioned, the perfect revival at $t = 2nT^-$ comes from the same dynamical phase of all 2^N pathways of returning to $|\Psi(0)\rangle$ when $JT = \pi$. Once $JT \neq \pi$, these dynamical phases are no longer the same. In particular, the larger N is, the more rapidly the dynamical phase varies with changing the pathways. In the large N limit, this DTC becomes supersensitive to the value of JT and serves as a high precision device to measure

either J or T.

Since it is time-consuming to solve more than 14 lattice sites using exact diagonalization when inhomogeneities exist, we focus on homogeneous systems. It is expected that the lower bound of the results of an inhomogeneous distribution, $\theta_i \in [\bar{\theta} - w_s, \bar{\theta} + w_s]$, could be estimated using homogeneous $\theta_i = \bar{\theta} \pm w_s$. As an example, we consider θ_i fixed at $\pi/4$. As shown in Fig. 3.5(a), $P(2nT^-)$ quickly vanishes if $|\delta| \gg \pi/N^{\frac{3}{2}}$, where $\delta = JT - \pi$. It is known that the Heisenberg limit, $1/N$, sets the bound of the precision in linear metrology, whereas non-linearity allows going beyond this limit [111]. The DTC discussed here represents a new category of nonlinear quantum metrology using periodic drivings.

We evaluate some observables to quantitatively characterize the sensitivity. $P(2T)$, the returning probability to $|\Psi(0^-)\rangle$ after two periods, captures short time dynamics. Fig. 3.5(c) shows that the dependence of $P(2T)$ on JT has a narrow peak centered at π, whose width is of the order of $1/N^{\frac{3}{2}}$. Such scaling can be obtained analytically (Appendix 3.5.1), and is verified numerically, as shown in the inset of Fig. 3.5(c). Another quantity is the power spectrum, $\tilde{P}(f) = \frac{1}{M}\sum_{n=0}^{M-1} e^{i2\pi nTf} P(nT)$. We are particularly interested in $\tilde{P}(f = \frac{1}{2T})$ characterizing the response of the DTC at half of the frequency of the periodic driving. The dependence of $\tilde{P}(f)$ on JT also has a peak around π. We define the full width at half maximum (FWHM) as Δ_{JT}, and find both numerically and analytically that Δ_{JT} is proportional to $1/N^{\frac{3}{2}}$ (Appendix 3.5.1).

To gain insights into the scalings, we consider the quantum Fisher information,

$$I_{JT}(2nT) = \lim_{\epsilon \to 0} 4\frac{1 - F_\epsilon}{\epsilon^2}, \tag{3.15}$$

$$F_\epsilon = |\left\langle \Psi(0^-) \right| \mathcal{U}_{JT}(2nT)\mathcal{U}_{JT+\epsilon}(-2nT) \left| \Psi(0^-) \right\rangle|^2, \tag{3.16}$$

where F_ϵ is the Loschmidt echo. The squared root of the quantum Fisher information limits the precision of a phase measurement [15]. The uncertainty of JT is bounded by $\sqrt{I_{JT}(2nT)}$, i.e., $\Delta_{JT} \geq 1/\sqrt{I_{JT}(2nT)}$. We have found analytically that (Appendix 3.5.1),

$$I_\pi(2nT) = \frac{n^2}{4}[\sin^2(2\bar{\theta})N^3 + 2\sin^4(\bar{\theta})N^2]. \tag{3.17}$$

When $\bar{\theta} \neq 0, \pm\pi/2, \pi$, $I_\pi(2nT) \sim n^2N^3$, provided that $\sin^2(2\bar{\theta})N^3 \gg 2\sin^4(\bar{\theta})N^2$. Thus, $I_\pi(2nT)$ scales with n^2N^3 in the large N limit, as shown in Fig. 3.5(g,h). Correspondingly, $\Delta_{JT} \geq 1/\sqrt{I_\pi(2nT)} \sim n^{-1}N^{-\frac{3}{2}}$. This is precisely what we have obtained in Fig. 3.5(c,e).

DTCs previously discussed in the literature are stable within a finite range of both

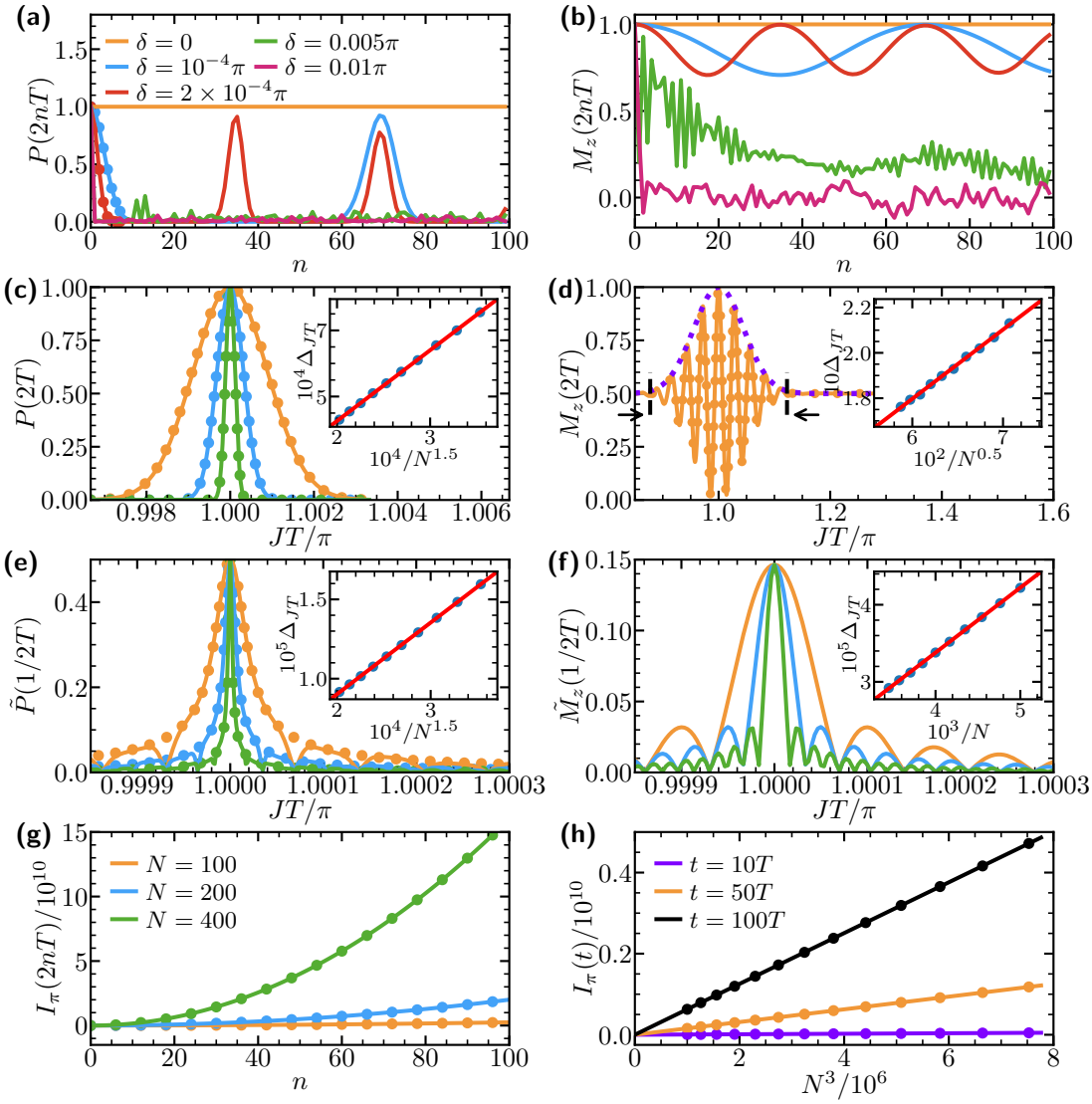

Figure 3.5: Sensitivity to JT. Curves (dots) are numerical (analytical) results. $\theta_i = \pi/4$ is used in all panels. The legend of (g) also applies to (c-f). (a,b) $P(2nT)$ and $M_z(2nT)$ as functions of n at various JT. When $|JT - \pi| \gg \pi/N^{3/2}$, both quantities decrease down to zero quickly. $N = 200$. (c,d) $P(2T)$ and $M_z(2T)$ as functions of JT. For a fixed N, $P(2T)$ and $M_z(2T)$ have narrow peaks centered at $JT = \pi$. $M_z(2T)$ has an extra fast oscillation. The dashed curve highlights the analytical result of its profile, whose width is denoted by black arrows. (e,f) The power spectra, $\tilde{P}(1/2T)$ and $\tilde{M}_z(1/2T)$, which contain information of both short and long-time dynamics, are also featured by narrow peaks around $JT = \pi$. $M = 200$. (g) The quantum Fisher information $I_\pi(2nT)$ as a function of n. (h) $I_\pi(2nT)$ is proportional to N^3. Insets show the scaling of the peak widths with N.

the interaction strength and a uniform deviation of θ_i from π. In contrast, the all-to-all interaction induced DTC is stable against any spatial fluctuations in θ_i and meanwhile supersensitive to JT. In practice, it is much easier to control J and T other than the N local parameters θ_i in a noisy environment, where θ_i's may not have any correlations at different locations. Moreover, our DTC could be used to measure JT with high precision beyond the Heisenberg limit. It mimics a supersensitive clock. If the frequency of the external field, $\omega_{\rm d} = 1/T$, is fixed, J, which corresponds to some internal parameter of a clock, for instance, the length of a pendulum clock, needs to be tuned with a precision of $1/N^{\frac{3}{2}}$ to deliver rigid ticks at $t = 2nT$. Otherwise, as shown in Fig. 3.5(c,e), once JT is out of the window of length $1/N^{3/2}$ centered at $JT = \pi$, both $P(2T)$ and $\tilde{P}(f)$ quickly decrease and the DTC stalls to avoid errors in the timekeeping. Our results thus lead to a new type of precision measurement of J. From $JT = \pi$, the precision of J can be estimated as $\Delta_J/J \approx \Delta_{\rm d}/\omega_{\rm d} + N^{-\frac{3}{2}}$, where $\Delta_{\rm d}/\omega_{\rm d}$ characterizes the precision of the driving frequency. When $N^{-\frac{3}{2}} \gg \Delta_{\rm d}/\omega_{\rm d}$, Δ_J/J scalings with $N^{-\frac{3}{2}}$. When $N \to (\Delta_{\rm d}/\omega_{\rm d})^{-2/3}$, the uncertainty of J eventually approaches the precision limit of $\Delta_{\rm d}/\omega_{\rm d}$. Whereas the precision of $\Delta_{\rm d}/\omega_{\rm d}$ is up to 10^{-19} in the THz regime [112], typical experiments on ultracold atoms, ion traps and NV centers have interaction strengths $\sim 10^2 - 10^5$Hz. In such regime, the precision of $\Delta_{\rm d}/\omega_{\rm d}$ could be 10^{-6} and above. Our results thus provide a new application of precision timekeeping in many-body physics.

Alternatively, if J is fixed, the DTC discussed here could gauge the frequency, as only a driving field, whose T deviates from π/J within $1/N^{\frac{3}{2}}$, could induce its long-lasting dynamics. Different from atomic clocks using a transition with a narrow line width, the selection of the driving frequency here entirely comes from the many-body effect we previously discussed. In particular, the rotated angle, $\bar{\theta}$, can be arbitrary such that the DTC could function in a non-ideal environment, unlike previous works requiring a precise control of pulses in non-linear metrology without periodic driving [113–115]. Though $1/J$ may not be as precise as transition frequencies in atomic clocks, the many-body effect induced $1/N^{\frac{3}{2}}$ scaling could make this DTC a useful gauge of the frequency or time.

We have also studied the scalings of other quantities. We have found that $M_z(2T^-)$ and $\tilde{M}(\frac{1}{2T})$ scale with $1/N^{\frac{1}{2}}$ and $1/N$, respectively, as shown by Fig. 3.5(b,d,f). Similar scalings are obtained for other uniform rotations. For instance, when $\theta_i = \pi/2$, Δ_{JT} of either $\tilde{P}(\frac{1}{2T})$ or $\tilde{M}_z(\frac{1}{2T})$ scales with $1/N$ (Appendix 3.5.1).

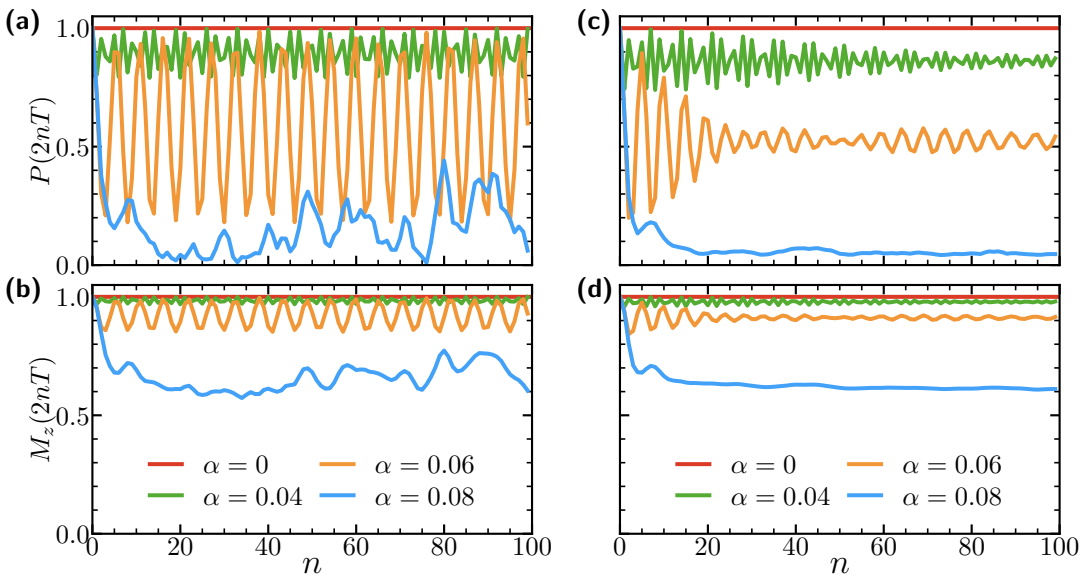

Figure 3.6: Power-law potentials for $N = 14$. (a,b) Uniform rotations with $\bar{\theta} = 0.95\pi$. $\alpha = 0$ corresponds to the all-to-all interaction. With decreasing α, the results of the power-law potentials approach those of the all-to-all interaction. All parameters are the same in (a) and (b). (c,d) Inhomogeneous rotations with $\bar{\theta} = \pi$ and $w_s = 0.1\pi$.

Whereas we have been focusing on the all-to-all interaction, similar conclusions apply to a generic long-range interaction, provided that its range is much larger than the size of the system. For instance, with decreasing α, the range of the a power-law potential in Eq. (3.9) increases. When $\alpha = 0$, it is equivalent to the all-to-all interaction. Fig. 3.6 shows the results for $N = 14$. With decreasing α down to zero, $P(2nT)$ and $M_z(2nT)$ increase and eventually approach the result of the all-to-all interaction. A small $\alpha = 0.04$ readily provides us with a good approximation of the all-to-all interaction in such a finite system.

Another application of the all-to-all interaction is to create a DTC of highly entangled states. To this end, we consider a uniform θ_i. When $JT = \pi/2$, $\theta_i = \pi/2$, starting from $|\Psi(0^-)\rangle = \prod_i |\uparrow\rangle_i$, as depicted in Fig. 3.1(d), the first pulse rotates the initial state to the equator, and $|\Psi(0^-)\rangle = |\pi/2, 0\rangle_c$, where $|\phi, \varphi\rangle_c$ denotes the coherent state specified by two angles ϕ and φ. Then the operator $e^{-i\frac{\pi}{2}J_z^2} = \frac{1-i}{2}(\mathbb{I} + ie^{-i\pi J_z})$ creates a superposition, $|\Psi(T^-)\rangle = \frac{1}{\sqrt{2}}(|\pi/2, 0\rangle_c + i^{N+1}|\pi/2, \pi\rangle_c)$, a Schrödinger's cat state formed by two coherent states. The second pulse rotates this cat state by $\pi/2$ about the y-axis, creating a NOON state, $|\Psi(T^+)\rangle = \frac{1}{\sqrt{2}}(i^{N+1}\prod_i |\uparrow\rangle_i + \prod_i |\downarrow\rangle_i) = \frac{1}{\sqrt{2}}(i^{N+1}|N/2\rangle + |-N/2\rangle)$, a cat formed by two Fock states. We have defined the eigenstate of L_z via $L_z|l\rangle = l|l\rangle$. Similar Schrödinger's cat

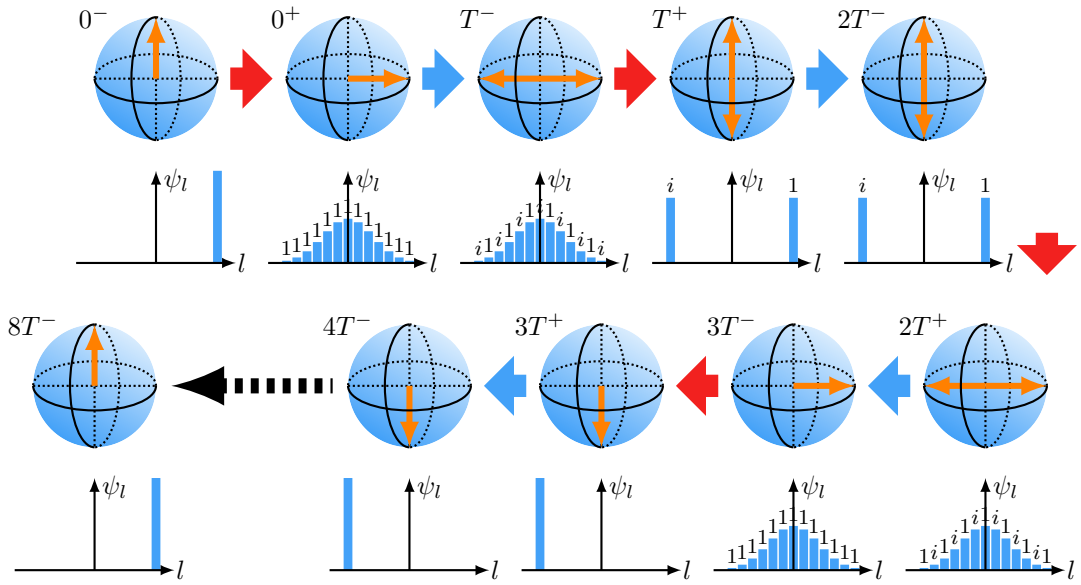

Figure 3.7: A DTC with a lattice spacing of $8T$ in time. Graphs under the Bloch spheres show the expansion of the wavefunctions in the basis of $|l\rangle$, the eigenstates of L_z, i.e., $|\Psi(t)\rangle = \sum_l \psi_l |l\rangle$. After the first $\pi/2$ pulse, $|\Psi(0^+)\rangle$ becomes a coherent state and ψ_l is a binomial distribution. When $JT = \pi/2$, the non-linear term creates a superposition of two coherent states, $|\Psi(T^-)\rangle = (|\pi/2, 0\rangle_c + i^{N+1} |\pi/2, \pi\rangle_c)/\sqrt{2}$. ψ_l remains a binomial distribution but the phases alternate between 1 and i. The second $\pi/2$-pulse creates a NOON state, $|\Psi(T^+)\rangle = (i^{N+1} |N/2\rangle + |-N/2\rangle)/\sqrt{2} = |\Psi(2T^-)\rangle$. The third $\pi/2$ pulse rotates the NOON state to the equator, $|\Psi(2T^+)\rangle = (i^{N+1} |\pi/2, 0\rangle_c + |\pi/2, \pi\rangle_c)/\sqrt{2}$, which is then turned into a coherent state $|\pi/2, 0\rangle_c$ at $t = 3T^-$ by the non-linear term. The fourth $\pi/2$ pulse rotates this coherent state to the south pole, which then becomes $|-N/2\rangle$ at $t = 4T^-$. Similar steps repeat and the system returns to the initial state at $t = 8T^-$

states emerge as time goes on, as depicted in Fig. 3.7, leading to a unique DTC with a lattice spacing of $8T$ in time. Its unit cell includes multiple Schrödinger's cat states. Whereas the nonlinear operator $e^{-i\frac{\pi}{2}J_z^2}$ has been used to squeeze a spin and create a NOON state [82, 116], a unique feature here is that Schrödinger's cat states repeatedly emerge in time, forming an intriguing DTC distinct from previously found ones that have simple unit cells containing trivial Fock states. As Schrödinger's cat states are fundamental ingredients in beating the standard quantum limit [81–84], this DTC gives rise to a sustainable source of such high entangled states for quantum metrology.

3.4 Experimental Realizations

In this section, we discuss the experimental realization of our model. Whereas we have used idealized delta-like kicks in the discussions of previous sections, our results can be straightforwardly generalized to pulses with finite widths. If we consider the Hamiltonian,

$$H = \begin{cases} 2J\sum_{i<j} S_i^z S_j^z, & nT < t < (n+1)T - \tau \\ \sum_i^N \frac{\theta_i}{\tau} S_i^y, & (n+1)T - \tau < t < (n+1)T, \end{cases} \tag{3.18}$$

where τ represents the finite width, we only need to replace $JT = \pi$ by $J(T-\tau) = \pi$ and other results remain unchanged.

In a finite system, as shown in Fig. 3.6, to qualitatively demonstrate our results for a system consisting of 14 spins, a power-law interaction width $\alpha = 0.04$ readily provides us with a good approximation of the all-to-all interaction. In fact, the only requirement is that the range of interaction is much larger than the size of the system. Meanwhile, the all-to-all interaction can be accessed by using photons in cavities or waveguides to couple atoms at different locations. We consider the following Hamiltonian,

$$H = \hbar\omega b^\dagger b + \Omega(b^\dagger + b)\sum_i (S_i^+ + S_i^-), \tag{3.19}$$

where the first term represents a single photon mode and the second term denotes the interaction between photons and atoms. We have assumed that the local Hamiltonian acting on each spin vanishes. $S_i^\pm = S_i^x \pm S_i^y$. Without the second term, the eigenstates are $|n\rangle \prod_i |\eta_i\rangle$, representing n photons and a Fock state of atoms, and $\eta = \uparrow, \downarrow$. Consider two specific atoms at sites $i \neq j$, their couplings induced by the photon can be derived using second order perturbation. For instance, the off-diagonal term is written as,

$$\begin{aligned} &\frac{1}{-\hbar\omega}\Omega^2 \langle n| \langle\downarrow_i\uparrow_j| \prod_{k\neq i,j} \langle\eta_k| bS_j^+ |n+1\rangle |\downarrow_i\downarrow_j\rangle \prod_{k\neq i,j} |\eta_k\rangle \\ &\quad \times \langle n+1| \langle\downarrow_i\downarrow_j| \prod_{k\neq i,j} \langle\eta_k| b^\dagger S_i^- |n\rangle |\uparrow_i\downarrow_j\rangle \prod_{k\neq i,j} |\eta_k\rangle \\ &+\frac{1}{\hbar\omega}\Omega^2 \langle n| \langle\downarrow_i\uparrow_j| \prod_{k\neq i,j} \langle\eta_k| b^\dagger S_j^+ |n-1\rangle |\downarrow_i\downarrow_j\rangle \prod_{k\neq i,j} |\eta_k\rangle \\ &\times \langle n-1| \langle\downarrow_i\downarrow_j| \prod_{k\neq i,j} \langle\eta_k| bS_i^- |n\rangle |\uparrow_i\downarrow_j\rangle \prod_{k\neq i,j} |\eta_k\rangle = -\frac{\Omega^2}{\hbar\omega}. \end{aligned} \tag{3.20}$$

This is equivalent to adding a term $-\frac{\Omega^2}{\hbar\omega} S_j^+ S_i^-$ to the unperturbed Hamiltonian. The diagonal

couplings can be obtained in a similar means. The full effective Hamiltonian after eliminating the photon mode is written as,

$$H_{\text{eff}} = -\frac{\Omega^2}{\hbar\omega}\sum_{i,j} S_j^+ S_i^- + h.c., \tag{3.21}$$

which can be further simplified as

$$H_{\text{eff}} = -\frac{2\Omega^2}{\hbar\omega}(\sum_i \vec{S}_i)^2 + \frac{2\Omega^2}{\hbar\omega}\sum_i (S_i^z)^2 + \frac{4\Omega^2}{\hbar\omega}\sum_{i<j} S_i^z S_j^z. \tag{3.22}$$

Since $\sum_i \vec{S}_i$ is conserved, the first two terms commute with the last term and the last term exactly matches an all-to-all interaction, we thus created all-to-all interaction with an equivalent strength $J = \frac{2\Omega^2}{\hbar\omega}$. Whereas the above discussions do not require the leakage of photons from the cavity, a "bad" cavity with leaking photons has the unique advantage of suppressing the heating that may be caused by the driving [117]. Thus, our results can be generalized to the full model including both the atoms and photons.

Whereas the above scheme is relevant to small systems, in which a fine tune of the local effective magnetic field is doable, our model can also be implemented by a two-mode bosonic system, in which the all-to-all interaction naturally exists. For instance, we consider a BEC in a double-well potential,

$$H = g_1\frac{n_l(n_l-1)+n_r(n_r-1)}{2} + g_2 n_l n_r + \sum_n (\theta a_l^\dagger a_r + h.c.)\delta(t-nT), \tag{3.23}$$

where g_1 and g_2 representonsite and intersite interactions and θ denotes the tunneling. If we map the left and the right site to the spin-up and the spin-down, respectively, $J = g_1 + g_2$ directly corresponds to the all-to-all interaction, and the tunneling term is mapped to H_{pul}. Such a mapping allows us to implement all results in the spin model to a large bosonic system with 10^4 particle and more.

3.5 Appendix

3.5.1 Scalings of physical quantities with particle numbers

We have analytically obtained how the dependence of $P(2T)$ ($M_z(2T)$) on JT scales with the particle number N,

$$P'(\delta) \equiv P(2T; JT = \pi + \delta) = (1 + \frac{N^2\delta^2 \sin^4\theta}{4})^{-1/2} e^{-\frac{1}{4N^2\delta^2\sin^4\theta+16}\sin^2(2\theta)\delta^2N^3}, \tag{3.24}$$

$$M_z'(\delta) \equiv M_z(2T; JT = \pi + \delta) = \cos^2\theta + \sin^2\theta\cos(\cos\theta N\delta)e^{-\frac{N}{2}\delta^2\sin^2\theta}. \tag{3.25}$$

When $\theta = \pi/2$, $\sin(2\theta) = 0$. The exponential function in Eq. (3.24) becomes identity, and $P'(\delta) = (1 + \frac{N^2\delta^2\sin^4\theta}{4})^{-1/2}$. Thus, the peak width shown in Fig. 3.8 scales with $1/N$. The same scaling applies to θ near 0 and π. In contrast, when θ is away from 0, $\pi/2$ and π, the exponential function becomes dominant, and $P(2T)$ decays faster, as shown in Fig. 3.5(c). In particular, the peak width of $P(2T)$ in Fig. 3.5(e) scales with $1/N^{3/2}$.

In Eq. (3.25), the $N\delta$ term in the cosine function leads to a fast oscillation, and the $N\delta^2$ term in the exponential function leads to the $1/N^{1/2}$ scaling of the profile of $M_z(2T)$, regardless of θ, as shown in the insets of Fig. 3.8(d) and Fig. 3.5(d).

To derive Eq. (3.24) and Eq. (3.25), we consider an initial state, $|\Psi(0^-)\rangle = \prod_i |\uparrow\rangle_i = \left|\frac{N}{2}, \frac{N}{2}\right\rangle$, where $L_z\left|\frac{N}{2}, l\right\rangle = l\left|\frac{N}{2}, l\right\rangle$ and $\frac{N}{2} = L$ is the total angular momentum.

$$\begin{aligned} P'(\delta) =& |\left\langle\Psi(0^-)\right| e^{-i(\pi+\delta)L_z^2}e^{-i\theta L_y}e^{-i(\pi+\delta)L_z^2}e^{-i\theta L_y}\left|\Psi(0^-)\right\rangle|^2 \\ =& |e^{-i(\pi+\delta)(\frac{N}{2})^2}\left\langle\Psi(0^-)\right| e^{-i\theta L_y}e^{-i(\pi+\delta)L_z^2}e^{-i\theta L_y}\left|\Psi(0^-)\right\rangle|^2. \end{aligned} \tag{3.26}$$

As discussed in Sec. 3.1, $e^{-i\pi L_z^2} = e^{-i\pi L_z}$ is satisfied for any even particle number N. When δ is small, $e^{-i\delta L_z^2}$ can be written as

$$e^{-i\delta L_z^2} \approx \int_{-N\delta}^{N\delta} dk e^{-ik^2/4\delta}\frac{1}{2\pi}\frac{\sqrt{\pi}}{\sqrt{-i\delta}}e^{-ikL_z}. \tag{3.27}$$

We thus obtain

$$P'(\delta) = |e^{-i(\pi+\delta)(\frac{N}{2})^2}\int_{-N\delta}^{N\delta} dk e^{-ik^2/4\delta}\frac{1}{2\pi}\frac{\sqrt{\pi}}{\sqrt{-i\delta}}I(\theta,k)|^2, \tag{3.28}$$

$$I(\theta,k) = \left\langle\Psi(0^-)\right| e^{-i\theta L_y}e^{-i\pi L_z}e^{-ikL_z}e^{-i\theta L_y}\left|\Psi(0^-)\right\rangle. \tag{3.29}$$

Note that $e^{-i\theta L_y}|\Psi(0^-)\rangle = |\theta,0\rangle_c$, $e^{i\pi L_z}e^{i\theta L_y}|\Psi(0^-)\rangle = (-1)^{\frac{N}{2}}|\theta,0\rangle_c$, we obtain

$$I(\theta,k) = (-1)^{\frac{N}{2}}\langle\theta,0|_c e^{-ikL_z}|\theta,0\rangle_c = (-1)^{\frac{N}{2}}e^{ik\frac{N}{2}}(\frac{1}{1+\alpha})^N(e^{-ik}\alpha+1)^N, \tag{3.30}$$

where $\alpha \equiv \tan^2\frac{\theta}{2}$ and

$$|\theta,\phi\rangle_c = \sum_{l=-N/2}^{N/2} \sqrt{\frac{N!}{(\frac{N}{2}+l)!(\frac{N}{2}-l)!}} (\cos\theta)^{\frac{N}{2}+l} (\sin\theta)^{\frac{N}{2}-l} e^{i\phi(\frac{N}{2}-l)} |l\rangle \tag{3.31}$$

is a coherent state pointing along θ, ϕ. In the large N limit,

$$I(\theta,k) \approx (-1)^{\frac{N}{2}} e^{-ik\frac{N}{2}+i\frac{N}{1+\alpha}k} e^{-\frac{N}{2}\frac{\alpha}{(1+\alpha)^2}k^2}, \tag{3.32}$$

which represents a narrow Gaussian centered at $k=0$. Substituting $I(\theta,k)$ in Eq. (3.28) by Eq. (3.32), we obtain Eq. (3.24).

As for $M_z'(\delta)$, using the time evolution operator $U(T) = e^{-iL_z^2 JT} e^{-iL_y\theta}$, we obtain the Heisenberg equations, which provide us with the nonlinear recursion relations as shown in [110],

$$\begin{aligned}
L_x' &= U^{-1}(T) L_x U(T) = \frac{1}{2}(L_x\cos\theta + L_z\sin\theta + iL_y) e^{i2JT(L_z\cos\theta - L_x\sin\theta+\frac{1}{2})} + h.c. \\
L_y' &= U^{-1}(T) L_y U(T) = \frac{1}{2i}(L_x\cos\theta + L_z\sin\theta + iL_y) e^{i2JT(L_z\cos\theta - L_x\sin\theta+\frac{1}{2})} + h.c. \\
L_z' &= U^{-1}(T) L_z U(T) = L_z\cos\theta - L_x\sin\theta.
\end{aligned} \tag{3.33}$$

Since $M_z(2T) = \frac{2}{N}\langle\Psi(0^-)| U^{-1}(T)U^{-1}(T)L_z U(T)U(T) |\Psi(0^-)\rangle$, we obtain,

$$\begin{aligned}
M_z'(\delta) =& \frac{2}{N}\Big\langle\Psi(0^-)\Big| [(L_z\cos\theta - L_x\sin\theta)\cos\theta \\
& - (\frac{1}{2}(L_x\cos\theta + L_z\sin\theta + iL_y) e^{i2JT(L_z\cos\theta - L_x\sin\theta+\frac{1}{2})} + h.c.)\sin\theta] \Big|\Psi(0^-)\Big\rangle \\
=& \cos^2\theta - (-1)^{\frac{N}{2}}\sin\theta[\sin\theta\cos^N\frac{\Theta}{2}\cos(JT - N\Phi) \\
& + (\cos\theta+1)\cos^N\frac{\Theta}{2}\tan\frac{\Theta}{2}\cos(\Phi + JT - N\Phi)] \\
=& \cos^2\theta + (-1)^{\frac{N}{2}}\sin\theta\cos^N(\frac{\Theta}{2})[\sin\theta\cos(\delta - N\Phi) \\
& + (\cos\theta+1)\tan\frac{\Theta}{2}\cos(\Phi + \delta - N\Phi)] \\
\approx& \cos^2\theta + \sin^2\theta\cos(\cos\theta N\delta) e^{-\frac{N}{2}\delta^2\sin^2\theta}
\end{aligned} \tag{3.34}$$

where $\Theta = \arccos\big(\cos^2\theta + \cos(2\delta)\sin^2\theta\big)$, $\Phi = \arctan\Big(\frac{-\sin\theta\sin(2\delta)}{\cos\theta\sin\theta(-1+\cos(2\delta))}\Big)$. The expression which contains Θ and Φ is exact for any θ and δ's. The final approximation comes from $\Theta^2 = 4\sin^2\theta\delta^2 + O(\delta^4)$, $\Phi = \pi/2 - \cos\theta\delta + O(\delta^3)$ and $\cos^N\frac{\Theta}{2} \approx e^{-N\delta^2\sin^2\theta/2}$ when δ is small and N is large. The overall profile as shown in Fig. 3.5(d) is thus given by $e^{-\frac{N}{2}\sin^2\theta\delta^2}\sin^2\theta + \cos^2\theta$.

We have also obtained an analytical form for $\tilde{P}(f)$, the Fourier transform of $P(2nT)$.

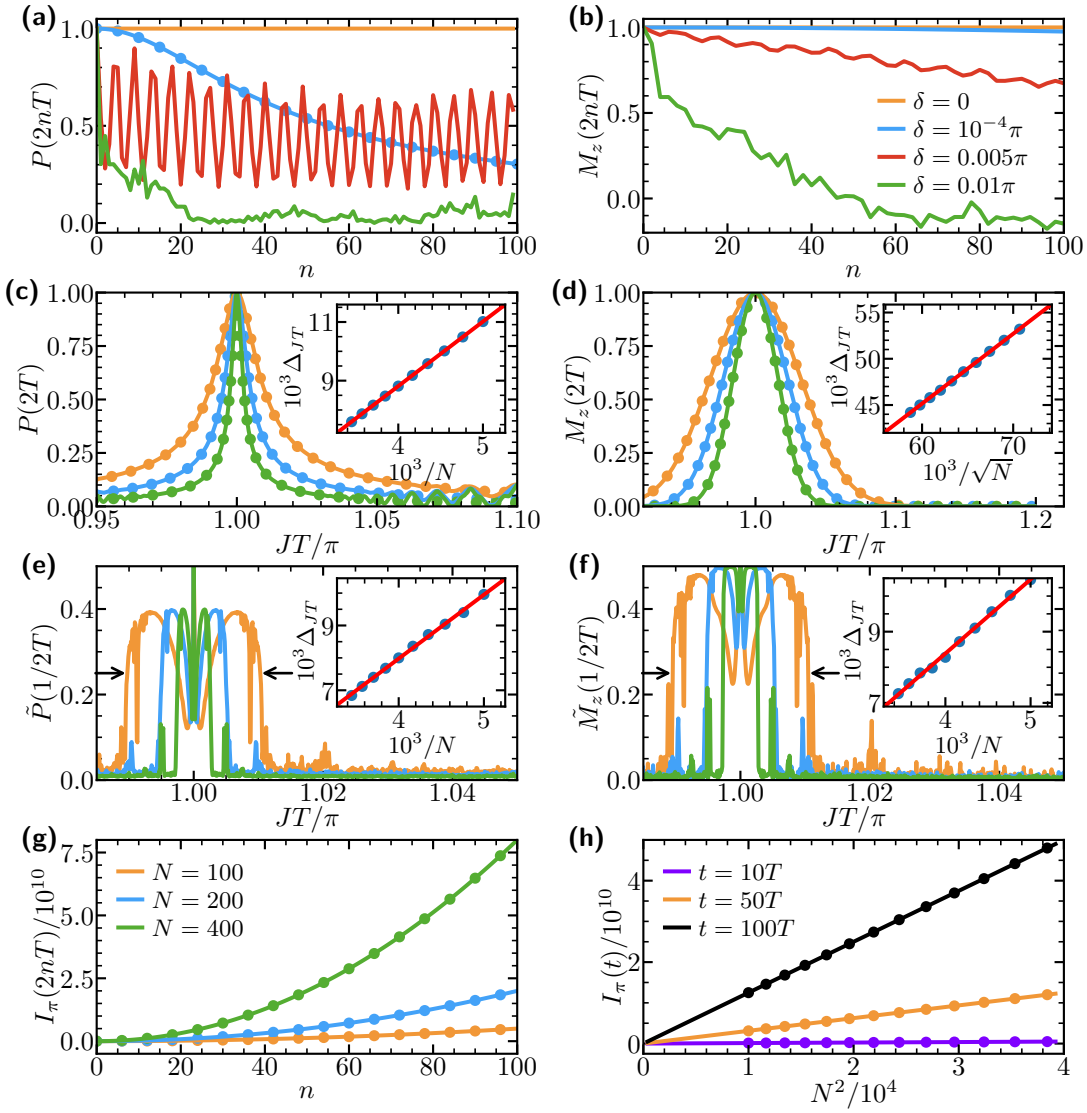

Figure 3.8: Sensitivity of the DTC to JT when $\theta_i = \pi/2$. Dots (curves) are analytical (numerical) results. The legend of (g) also applies to (c-f). (a,b) $P(2nT)$ and $M_z(2nT)$ as functions of n for various JT. When $|JT - \pi| \gg \pi/N$ (here N=200), both quantities quickly decrease down to zero. (c,d) $P(2T)$ and $M_z(2T)$ as functions of JT. For a fixed N, both quantities are featured with narrow peaks centered at $JT = \pi$. (e,f) The power spectra $\tilde{P}(1/2T)$ and $\tilde{M}_z(1/2T)$ are also featured with narrow peaks around $JT = \pi$. Whereas they exhibit non-monotonic behaviors near $JT = \pi$, both quantities vanish when $|JT - \pi| \gg \pi/N$. (g) The quantum Fisher information $I_\pi(2nT)$ as a function of n. (h) $I_\pi(2nT)$ is proportional to N^2. $\theta_i = \pi/2$ is used in all panels. Insets show the scalings of the widths of the peaks with N.

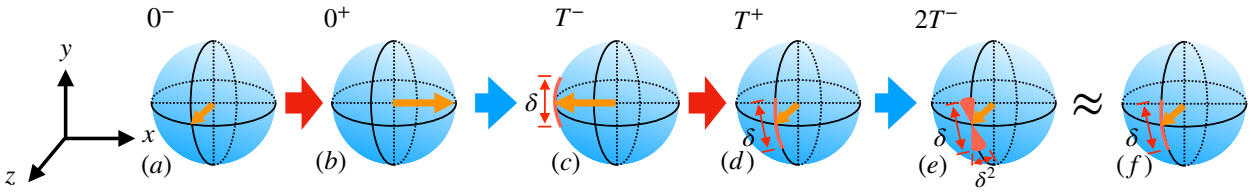

Figure 3.9: The approximation used to derive $P(2nT)$. When $t = T^-$, the nonlinear operator $e^{-iJTL_z^2}$ creates a superposition of coherent states, which spans a length scale $\sim \delta$ in the latitude direction, as shown in (c). This length scale is transferred to the longitude direction around the north pole by the pulse at $t = T^+$, as shown in (d). Then the nonlinear operator creates a superposition of coherent states in the region highlighted by the red color at $t = 2T^-$. The length scales of this region in the longitude and latitude directions are δ and δ^2 respectively, as shown in (e). Replacing the second nonlinear operator $e^{-iJTL_z^2}$ by $e^{-i\pi L_z^2}$, as shown in (f), we have ignored the expansion of the wavefunction in the latitude direction that gives rise to a high order correction to $P(2nT)$ at small times.

As shown in Fig. 3.9, starting from an initial state at the north pole, the state at $t = 2T^-$ covers a finite small region near the north pole, if $\delta = JT - \pi$ is small. The length scales of the longitude and latitude directions are proportional to δ and δ^2, the latter of which can be ignored in the small δ limit. Thus, we make use of the following approximation to capture the dynamics in the small δ limit,

$$U(2T) = e^{-iJTL_z^2}e^{-i\theta L_y}e^{-iJTL_z^2}e^{-i\theta L_y} \approx e^{-i\pi L_z^2}e^{-i\theta L_y}e^{-iJTL_z^2}e^{-i\theta L_y}. \tag{3.35}$$

$P(2nT)$ is written as

$$P(2nT) = |\left\langle\Psi(0^-)\right|(e^{-i\pi L_z^2}e^{-i\theta L_y}e^{-i(\pi+\delta)L_z^2}e^{-i\theta L_y})^n\left|\Psi(0^-)\right\rangle|^2. \tag{3.36}$$

Using the identities, $e^{-i\pi L_z^2} = e^{-i\pi L_z}$ and $e^{-i\pi L_z}e^{-i\theta L_y}e^{-i\pi L_z} = e^{i\theta L_y}$, the equation above can be written as

$$\begin{aligned} P(2nT) &= |\left\langle\Psi(0^-)\right|(e^{i\theta L_y}e^{-i\delta L_z^2}e^{-i\theta L_y})^n\left|\Psi(0^-)\right\rangle|^2 \\ &= |\left\langle\Psi(0^-)\right|e^{i\theta L_y}e^{-in\delta L_z^2}e^{-i\theta L_y}\left|\Psi(0^-)\right\rangle|^2. \end{aligned} \tag{3.37}$$

Applying Eq. (3.24), we obtain

$$P(2nT) = e^{-\frac{n^2\sin^2(2\theta)\delta^2N^3}{4N^2n^2\delta^2\sin^4\theta+16}}(1+\frac{n^2N^2\delta^2\sin^4\theta}{4})^{-1/2}. \tag{3.38}$$

Eq. (3.38) recovers Eq. (3.24) when $n = 1$. As shown in Fig. 3.8(a), this expression well captures the initial decay of $P(2nT)$. However, it cannot describe the revival of $P(2nT)$ in later times for certain JT due to the made approximation in Eq. (3.35).

The power spectrum is therefore written as

$$\tilde{P}(1/2T) = \frac{1}{M}\sum_{n=0}^{M-1} P(nT)e^{i\frac{2\pi}{2T}nT} = \frac{1}{M}\sum_{n=0}^{M-1} P(nT)(-1)^n \approx \frac{1}{M}\sum_{n=0}^{M/2-1} P(2nT), \tag{3.39}$$

where M is the cutoff required in numerics. In the last step, we have used the fact that, for small n, $|\psi(2nT+T)\rangle$ is located at a place on the Bloch sphere away from the north pole, provided that θ is not small, and thus,

$$P(2nT+T) = |\left\langle \Psi(0^-)\middle|\psi(2nT+T)\right\rangle|^2 \approx 0. \tag{3.40}$$

When $nN\delta \ll 1$ and $\theta \neq 0, \pi/2, \pi$, Eq. (3.38) becomes $P(2nT) = e^{-\frac{n^2\sin^2(2\theta)\delta^2N^3}{16}}$, and Eq. (3.39) is rewritten as

$$\tilde{P}(1/2T) \approx \frac{2\sqrt{\pi}\mathrm{Erf}(\frac{1}{8}\delta M N^{3/2}\sin(2\theta))}{\sin(2\theta)\delta M N^{3/2}}, \tag{3.41}$$

In the limit $M \to \infty$, $\tilde{P}(1/2T) \to \frac{1}{2\sqrt{\pi}}e^{-\frac{1}{64}\delta^2N^3M^2}$. To compare with numerical result, we choose $\theta = \pi/4$ and $M = 200$. Eq. (3.41) becomes

$$\tilde{P}(1/2T) \approx \frac{2\sqrt{\pi}\mathrm{Erf}(25\delta N^{3/2})}{200\delta N^{3/2}}, \tag{3.42}$$

which shows the $1/N^{3/2}$ scaling. Erf is the error function. The comparison between this analytical result and the numerical one is shown in Fig. 3.5(e).

When $\theta = \pi/2$, the exponential term in Eq. (3.38) becomes identity. We obtain

$$\tilde{P}(1/2T) \approx \frac{\mathrm{arcsinh}(\delta M N/4)}{\delta M N/2}. \tag{3.43}$$

As mentioned in Fig. 3.8, when $\theta = \pi/2$, the dependence of $\tilde{P}(1/2T)$ on JT is not monotonic. With increasing δ, $\tilde{P}(1/2T)$ first quickly decreases and then increases before it eventually vanishes when $\delta > \pi/N$. Eq. (3.43) captures the narrow peak, whose width is much smaller than π/N, near $\delta = 0$. The broader peak scales with $1/N$ as shown in Fig. 3.8(f). When θ deviates from $\pi/2$, the broader peak gets suppressed as shown in Fig. 3.10. When $\theta = \pi/4$, only the central narrow peak is visible, whose width scales with $1/N^{3/2}$, as discussed before.

$M_z(2nT)$ and $\tilde{M}_z(1/2T)$ do not have simple analytical forms. We have numerically evaluated them and the scaling of $\tilde{M}_z(1/2T)$ with N is shown in Fig. 3.8(b, e).

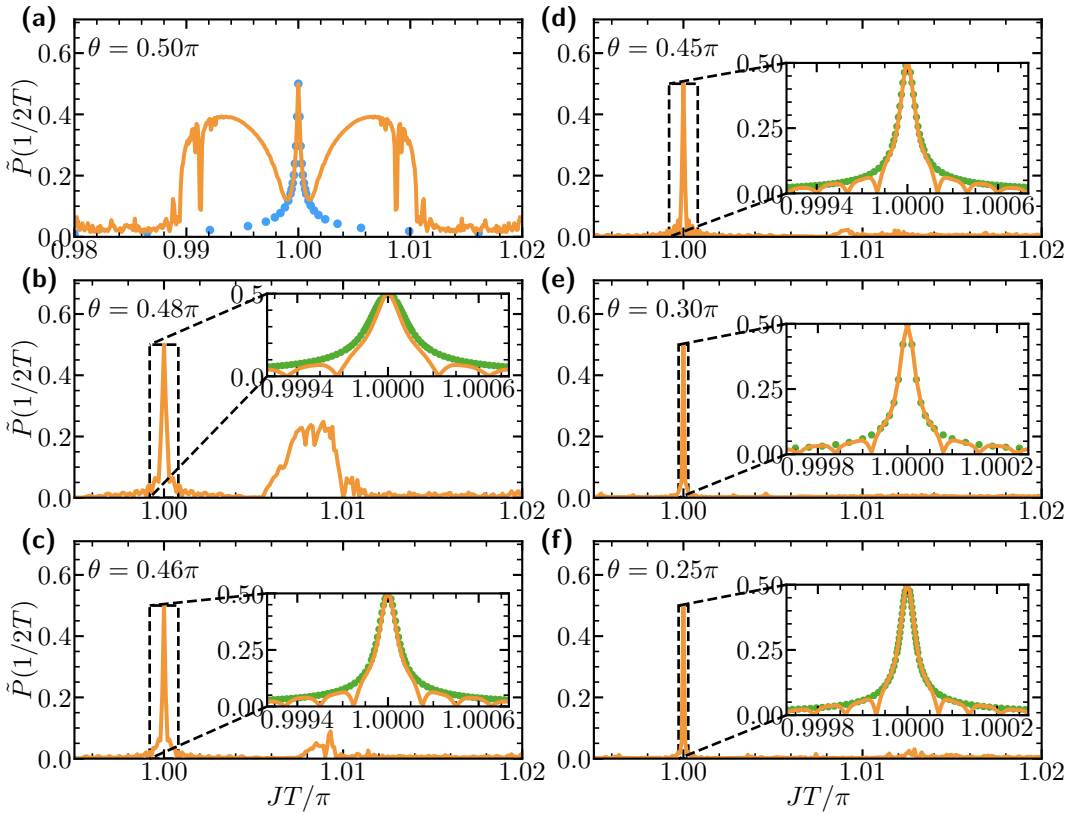

Figure 3.10: The power spectra $\tilde{P}(1/2T)$ for different pulses for $N = 100$, $M = 200$. (a) It is identical to the curve for $N = 100$ in Fig. 3.8(e). The central sharp peak at $JT = \pi$ for $\pi/2$ pulse is well approximated by the analytical result (blue dots) shown in Eq. (3.43). (b-f) When θ decreases, the two broader peaks gradually vanish. When the exponential term in Eq. (3.38) dominates, the central peak is described by Eq. (3.41) (green dots). Enlarging (f) around $JT = \pi$ gives rise to Fig. 3.5(e).

When $JT = \pi$, the quantum Fisher information is written as

$$I_\pi(2nT) = \lim_{\epsilon\to 0} 4\frac{1-F_\epsilon}{\epsilon^2}, \tag{3.44}$$

$$F_\epsilon = |\left\langle \Psi(0^-)\right| \mathcal{U}_\pi(-2nT)\mathcal{U}_{\pi+\epsilon}(2nT)\left|\Psi(0^-)\right\rangle|^2. \tag{3.45}$$

As $\mathcal{U}_\pi(2nT)\left|\Psi(0^-)\right\rangle = \left|\Psi(0^-)\right\rangle$ or equivalently, $\left\langle\Psi(0^-)\right|\mathcal{U}_\pi(-2nT) = \left\langle\Psi(0^-)\right|$, the Loschmidt echo is identical to the quantum memory of the initial state, F_ϵ. Using Eq. (3.38) and replacing ϵ by δ, we obtain

$$I_\pi(2nT) = \lim_{\delta\to 0} 4\frac{1-P(2nT)}{\delta^2} = \frac{n^2N^3\sin^2(2\theta)}{4} + \frac{n^2N^2\sin^4\theta}{2}. \tag{3.46}$$

3.5.2 Numerical simulation methods

In this section, we present some details of the numerical simulations used to produce Fig. 3.2, 3.5, and Fig. 3.8. We write the time-dependent many-body wavefunction, $|\Psi(t)\rangle$, as superposition of Fock states, which are eigenstates of S_z. In the presence of $H_{\rm int}$, every Fock state acquires an dynamical phase factor. $H_{\rm pul}$ is then applied to flip the spins at $t = nT$ to obtain the evolution of the many-body wavefunction.

The entanglement entropy S in Fig. 3.2 is calculated by first tracing out half of the system and obtaining a density matrix ρ_B for the other half of the system. We then diagonalize ρ_B and obtain all its eigenvalues v_i. S is then calculated by using $S = -\sum_i v_i \ln(v_i)$.

The power spectra shown in Fig. 3.5 and Fig. 3.8 are obtained as follows. $P(t)$ and $M_z(t)$ are evaluated in the time interval between $t = 0$ and $t = MT$ where M represents the longest time we considered in the simulation. We then use $\tilde{P}(f) = \frac{1}{M}\sum_{n=0}^{M-1} e^{i2\pi nTf}P(nT)$ to calculate the power spectra.

We have used to the full width at half maximum to characterize the width of power spectrum. Namely, when the value of P or M_z is decreased to half of its maximum, we define the twice of the deviation of JT from π as the width.

4. GEOMETRIZING QUANTUM DYNAMICS OF A BOSE-EINSTEIN CONDENSATE

This chapter is based on the published article [118] by C. Lyu, C. Lv, and Q. Zhou, Geometrizing quantum dynamics of a Bose-Einstein condensate, Phys. Rev. Lett. ***125****, 253401 (2020). Copyright (2020) by the American Physical Society.*

The importance of geometry in physics has been well established in general relativity and many other topics. More strikingly, geometries arise as emergent phenomena in certain quantum systems. For instance, AdS/CFT has revolutionized our understandings of the space-time by establishing the duality between a quantum field theory and a gravity in a higher dimension, where the hyperbolic geometry is essential [119, 120]. It has also been conjectured that two entangled copies of quantum field theories, which is described by a thermofield double state (TFD) living on the boundaries, are dual to an Einstein-Rosen wormhole in the bulk [121–124]. The hyperbolic geometry also occurs in scale invariant tensor networks that have offered physicists a new scheme of exploring quantum entanglement [125–128]. In these known examples, a prerequisite for the emergent geometries is the existence of strong correlations in quantum many-body systems. A question thus arises as to whether one could use weakly interacting systems, where gauge theory/gravity duality is unavailable at the moment, to reveal some intriguing geometries.

In this chapter, by revealing the SU(1,1) symmetry, we show that quantum dynamics of weakly interacting bosons have deep roots in the hyperbolic geometry. A wide range of quantum dynamical phenomena, including stable and unstable excitation modes of a Bose-Einstein condensate (BEC) [129–138], have direct geometric interpretations using closed or open trajectories on a Poincaré disk, a prototypical model for the hyperbolic surface (Sec. 4.3). This geometric approach allows us to correlate the time, the most fundamental measure of quantum dynamics, to the length in the hyperbolic space, and to the temperature that captures thermalization of a subsystem in TFD. The overlap between two close TFDs are is related to the metric of a Poincaré disk. In addition to fundamental insights, our geometric scheme provides us with a powerful tool to coherently control the quantum dynamics (Sec. 4.4). For instance, using periodical drivings, we could pump bounded stable modes to arbitrarily large occupations or coherently slow down the inflation of unstable modes. In particular, a Poincaré disk encodes SU(1,1) echoes that deliver quantum revivals of any initial state. Analogous to conventional echoes in spin systems, which are based on

$\mathfrak{su}(2)$ algebra, SU(1,1) echoes offer a broad range of bosonic systems a powerful scheme to reverse their quantum dynamics and explore information scrambling via out-of-time ordering correlators (OTOC) [42, 43, 46, 47].

4.1 Introduction

We consider the Hamiltonian describing weakly interacting bosons

$$H = \sum_{\vec{k}} E_{\vec{k}} c^\dagger_{\vec{k}} c_{\vec{k}} + \frac{\tilde{U}}{2V} \sum_{\vec{k},\vec{k}',\vec{q}} c^\dagger_{\vec{k}+\vec{q}} c^\dagger_{\vec{k}'-\vec{q}} c_{\vec{k}'} c_{\vec{k}}, \tag{4.1}$$

where the interaction strength $\tilde{U} = 4\pi\hbar^2 \frac{a_s}{m}$ is determined by the scattering length $a_s(t)$ and the mass m. $c^\dagger_{\vec{k}}$ and $c_{\vec{k}}$ are the creation and annihilation operators for bosons at the momentum $\vec{k}$. At the initial state, the scattering length is fixed at a small value, $a_s(t=0)$. The ground state is a BEC at $\vec{k} = 0$ with small depletions at finite momenta. Starting from $t = 0$, $a_s(t)$ is tuned dynamically using the magnetic or optical Feshbach resonance [1], as shown in Fig. 4.1. We are interested in an arbitrary $a_s(t)$, including negative scattering lengths. Though the ground state of a BEC with attractive interactions is not stable [129, 133, 134, 138], coherent dynamics is still achievable within a timescale before the loss of particles begins to happen, as shown by a recent experiment [139]. Indeed, we focus on short-time dynamics in which the particle number at a finite momentum, $N_{\vec{k}\neq 0}$, is small enough such that interactions among excitations, such as $N_{\vec{k}\neq 0} N_{\vec{k}'\neq 0}$, are negligible. The quantum dynamics is therefore governed by a Hamiltonian, $H_{\text{eff}} = \sum_{\vec{k}} H_{\vec{k}}$,

$$H_{\vec{k}}(t) = \xi_0(\vec{k}) K_0 + \xi_1(\vec{k}) K_1 + \xi_2(\vec{k}) K_2, \tag{4.2}$$

where

$$K_0 = \frac{1}{2}(c^\dagger_{\vec{k}} c_{\vec{k}} + c_{-\vec{k}} c^\dagger_{-\vec{k}}),\ K_1 = \frac{1}{2}(c^\dagger_{\vec{k}} c^\dagger_{-\vec{k}} + c_{\vec{k}} c_{-\vec{k}}),\ K_2 = \frac{1}{2i}(c^\dagger_{\vec{k}} c^\dagger_{-\vec{k}} - c_{\vec{k}} c_{-\vec{k}}) \tag{4.3}$$

$\xi_0(\vec{k}) = 2(E_{\vec{k}} + \tilde{U}|\Psi_0|^2)$, $\xi_1(\vec{k}) = 2\,\mathrm{Re}\,U$, $\xi_2(\vec{k}) = -2\,\mathrm{Im}\,U$, $U = \tilde{U}\Psi_0^2$, and $\Psi_0 = \sqrt{N_0/V}e^{i\theta}$ is the condensate wavefunction. The above equations show that we could discuss the dynamics at different $\vec{k}$ separately. Since all microscopic parameters in $H_{\vec{k}}(t)$, including $E_{\vec{k}}$, $\tilde{U}$ and θ, are tunable, we could focus on a single $H_{\vec{k}}$. As shown in later sections, this model can be realized using a wide range of apparatuses, and thus our results are applicable to a variety of systems.

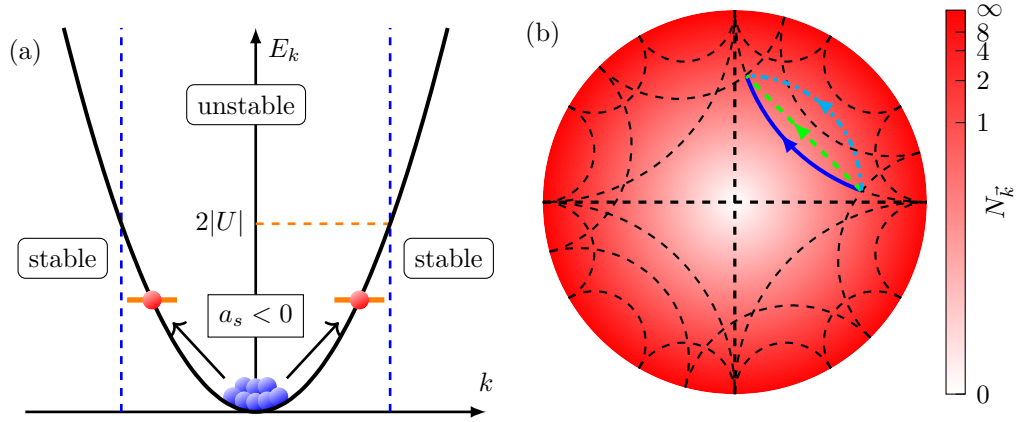

Figure 4.1: Geometrization of quantum dynamics. (a) A time-dependent interaction scatters pairs of bosons from the condensate to states with opposite momenta. When the interaction strength is negative, states with small kinetic energies have exponentially growing occupations, referred to as unstable modes. Occupations at stable modes with large kinetic energies have upper bounds. (b) Each point on a Poincaré disk represents a TFD. The color scale highlights the particle number or equivalently, the effective temperature of each TFD. Dashed straight lines passing through the origin and arcs perpendicular to the boundary circle represent the geodesics. Arrowed curves denote trajectories representing dynamical evolution of the quantum system. The blue curve following the geodesic corresponds to an extreme of the time spent in a quench dynamics.

As the first trial to understand the Hamiltonian Eq. (4.2), let us first set $\xi_2 = 0$, $\xi_0 > 0$, $\xi_1 > 0$ and view $c_{\vec{k}}$ and $c_{-\vec{k}}$ as the ladder operators of two harmonic oscillators. Introducing

$$x_1 = \frac{1}{\sqrt{2}}(c^\dagger_{\vec{k}} + c_{\vec{k}}),\ p_1 = \frac{i}{\sqrt{2}}(c^\dagger_{\vec{k}} - c_{\vec{k}}), \tag{4.4}$$

$$x_2 = \frac{1}{\sqrt{2}}(c^\dagger_{-\vec{k}} + c_{-\vec{k}}),\ p_2 = \frac{i}{\sqrt{2}}(c^\dagger_{-\vec{k}} - c_{-\vec{k}}), \tag{4.5}$$

The Hamiltonian becomes two coupled harmonic oscillators,

$$H = \frac{\xi_0}{2}(\frac{1}{2}x_1^2 + \frac{1}{2}p_1^2 + \frac{1}{2}x_2^2 + \frac{1}{2}p_2^2) + \frac{\xi_1}{2}(x_1x_2 - p_1p_2). \tag{4.6}$$

Further introducing

$$X_1 = \frac{1}{\sqrt{2}}(x_1 + x_2), P_1 = \frac{1}{\sqrt{2}}(p_1 + p_2), \tag{4.7}$$

$$X_2 = \frac{1}{\sqrt{2}}(x_1 - x_2), P_2 = \frac{1}{\sqrt{2}}(p_1 - p_2), \tag{4.8}$$

we get two decoupled harmonic oscillators,

$$H = \frac{\xi_0 + \xi_1}{4}X_1^2 + \frac{\xi_0 - \xi_1}{4}P_1^2 + \frac{\xi_0 - \xi_1}{4}X_2^2 + \frac{\xi_0 + \xi_1}{4}P_2^2. \tag{4.9}$$

It is now clear that

- when $\xi_0 > \xi_1$, these are two ordinary oscillators.
- when $\xi_0 < \xi_1$, the first oscillator has a negative kinetic energy and the second oscillator sees a parabolic potential with its opening facing down. This results in dynamic instability shown in later sections.
- $\xi_0 = \xi_1$ corresponds to a critical point between the two phases above. Naively speaking, the Hamiltonian is a massless oscillator plus a free particle.

4.2 SU(1,1) Symmetry of Weakly Interacting Bose Gas

The generic form of the Hamiltonian in Eq. (4.2) is a combination of three operators that satisfy the commutation relations of $\mathfrak{su}(1,1)$ algebra

$$[K_1, K_2] = -iK_0,\ [K_0, K_1] = iK_2,\ [K_2, K_0] = iK_1. \tag{4.10}$$

Therefore, any propagator,

$$P(t) = \mathrm{T}e^{-i\int_0^t dt' H_{\vec{k}}(t')}, \tag{4.11}$$

where T is the time-ordering operator, is an element in SU(1,1) group[140]. The three coefficients $\xi_{0,1,2}$ form an external field $\vec{\xi} = \{\xi_0, \xi_1, \xi_2\}$, analogous to the magnetic field in the case of spin-1/2, and its strength $\xi = \sqrt{\xi_0^2 - \xi_1^2 - \xi_2^2}$ characterizes the energy scale of the Hamiltonian. For instance, when $\xi_0^2 > \xi_1^2 + \xi_2^2$, using standard Bogoliubov transformation, the energy spectrum is given by $m\xi$, where m is an integer.

Since the global U(1) phase does not affect physical observables, we consider the quotient, SU(1,1)/U(1), which has a dimension of two, i.e., each group element can be parameterized by two real numbers, similar to SU(2)/U(1). An element of this group can be explicitly created by a combination of two operations,

$$R(\varphi_0) = e^{-i\varphi_0 K_0}, \tag{4.12}$$

$$B(\varphi_1, 0) = e^{-i\varphi_1 K_1}, \tag{4.13}$$

which correspond to a rotation and a boost respectively. A generic expression of the boost is given by $B(\varphi_1, \varphi_2) = e^{-i(\varphi_1 K_1 + \varphi_2 K_2)}$, which amounts to boosts along different directions. Eqs. (4.12, 4.13) provide us with a parameterization of the propagators determined by $H_{\vec{k}}$. It is well-known that SU(1,1)/U(1) has a nice geometric representation using a Poincaré disk [140, 141], a fundamental model for the hyperbolic surface. It is defined in a unit circle with the metric

$$ds^2 \equiv \frac{4(dx^2 + dy^2)}{(1 - x^2 - y^2)^2}, \tag{4.14}$$

where (x, y) denotes Cartesian coordinates. Geodesics in this curved space are either diameters through the center of the disk or circles perpendicular to the boundary, as shown in Fig. 4.1(b). A similar approach was revisited very recently to consider geometric phases in the adiabatic limit [142].

The above observation of the symmetry inspires us to establish a one-to-one correspondence between the quantum dynamics of the BEC and a Poincaré disk. Such a mapping requires two steps. First, we need to assign each point on the Poincaré disk a unique quantum state. Second, the metric of a Poincaré disk need to be associate with a physical quantity of the dynamics.

We consider the vacuum as the initial state, $|\Psi(0)\rangle = |0\rangle_{\vec{k}}|0\rangle_{-\vec{k}}$, where $c_{\vec{k}}|0\rangle_{\vec{k}} = 0$. The

two operators in Eqs. (4.12, 4.13) deliver a wavefunction, which is written as

$$\begin{aligned}|z\rangle =& R(\varphi_0)B(\varphi_1,0)R^\dagger(\varphi_0)\,|\Psi(0)\rangle \\ =& R(\varphi_0)e^{i\frac{\varphi_0}{2}}e^{-i\frac{\varphi_1}{2}(c^\dagger_{\vec{k}}c^\dagger_{-\vec{k}}+c_{\vec{k}}c_{-\vec{k}})}\,|0\rangle_{\vec{k}}\,|0\rangle_{-\vec{k}} \\ =& \sqrt{1-|z|^2}\sum_n z^n\,|n\rangle_{\vec{k}}\,|n\rangle_{-\vec{k}}\,,\end{aligned} \tag{4.15}$$

where $z=-ie^{-i\varphi_0}\tanh\frac{\varphi_1}{2}$ and $|n\rangle_{\vec{k}}=c^{\dagger n}_{\vec{k}}|0\rangle/\sqrt{n!}$. The expression in Eq. (4.15) is a TFD, which has a wide range of powerful applications in high energy physics, condensed matter physics, and quantum information [42, 43, 121–124]. Since $|z|\leq 1$, if we choose $z=x+iy$, we could identify each TFD in Eq. (4.15) with a unique point on the Poincaré disk. The expectation value of excited particle number of a TFD is

$$N_{\vec{k}}=(1-|z|^2)\sum_n |z|^{2n}n=\frac{|z|^2}{1-|z|^2}. \tag{4.16}$$

An intriguing property of TFD is that tracing half of the system in such a pure state leaves the other half with a thermal density matrix,

$$\rho_{\vec{k}}=\mathrm{Tr}_{-\vec{k}}\,|z\rangle\,\langle z|=\mathcal{Z}^{-1}\sum_n e^{-\frac{nE_{\vec{k}}}{k_BT}}\,|n\rangle_{\vec{k}}\,\langle n|_{\vec{k}}\,, \tag{4.17}$$

similar to Hawking radiation and Unruh effects [143, 144]. In Eq. (4.17), we have identified the Euclidean distance to the center of the disk, $|z|$, with a temperature,

$$\tilde{T}\equiv\frac{k_BT}{E_k}=-\frac{1}{2}\ln^{-1}|z|, \tag{4.18}$$

and $\mathcal{Z}=1-e^{-\frac{E_{\vec{k}}}{k_BT}}$. Therefore, each point on the Poincaré disk can be assigned with a temperature. In particular, the boundary circle corresponds to an infinite temperature.

Next, we evaluate the fidelity between TFDs, $F_{z,z'}=|\langle z'|z\rangle|^2$, we obtain,

$$|\langle z|z'\rangle|^2=\frac{(1-|z|^2)(1-|z'|^2)}{|1-z^*z'|^2}. \tag{4.19}$$

Consider two TFDs close to each other on the Poincaré disk, i.e., $z'=z+dz$, from the above expression, we immediately obtain

$$ds^2=4(1-F_{z,z+dz}). \tag{4.20}$$

We conclude that the fidelity between TFDs corresponds to the metric of a Poincaré disk. The mapping to a Poincaré disk is now established and it unfolds the intrinsic geometric

nature of the quantum dynamics as shown in the following sections.

4.3 Quantum Quench Dynamics on the Poincaré Disk

As the first example, we consider the quench dynamics, where the scattering length a_s is quenched from 0 to a finite negative value at $t = 0$. This means the Hamiltonian is quenched from $H_{\vec{k}} = 2E_{\vec{k}}K_0$ to

$$H_{\vec{k}} = 2(E_{\vec{k}} - |U|)K_0 - 2|U|K_1. \tag{4.21}$$

Thus the system is initially located at the center of the Poincaré disk and then starts to move. Depending on the parameters E_k and U in Eq. (4.2), there are 3 types of dynamical evolution.

- When $E_{\vec{k}} > 2|U|$ or equivalently, $\xi^2 > 0$, the growth of particle number $N_{\vec{k}}$ is bounded from above and is referred as to a stable mode, which is the result from Bogoliubov theory. On the Poincaré disk, the trajectory of the evolution is described by a closed loop, as shown in Fig. 4.2(b).

- When $E_{\vec{k}} = 2|U|$, ξ vanishes at this critical point and the topology of the trajectory begins to change. On the Poincaré disk, the trajectory becomes tangent to the boundary of the Poincaré disk in the limit of $t \to \infty$ (Appendix 4.7.3), as shown by the brown curve in Fig. 4.2(b).

- When $E_{\vec{k}} < 2|U|$, i.e., $\xi^2 < 0$, the well-known dynamical instability occurs and $N_{\vec{k}}$ grows exponentially as a function of t, mimicking the inflation in the early universe [132]. On the Poincaré disk, these unstable mode corresponds to an open trajectory, starting from the origin and extending to the infinity, i.e., the circular boundary. However, it takes infinite time to reach the boundary circle, providing a transparent interpretation of a basic phenomenon in hyperbolic geometry that the boundary circle of the Poincaré disk corresponds to infinity.

The most interesting result becomes clear if we consider the resonant mode, $E_{\vec{k}} = |U|$. Starting from the center of the Poincaré disk that represents the vacuum, the trajectory follows the diameter, which is precisely a geodesic. In fact, in a quench dynamics, the

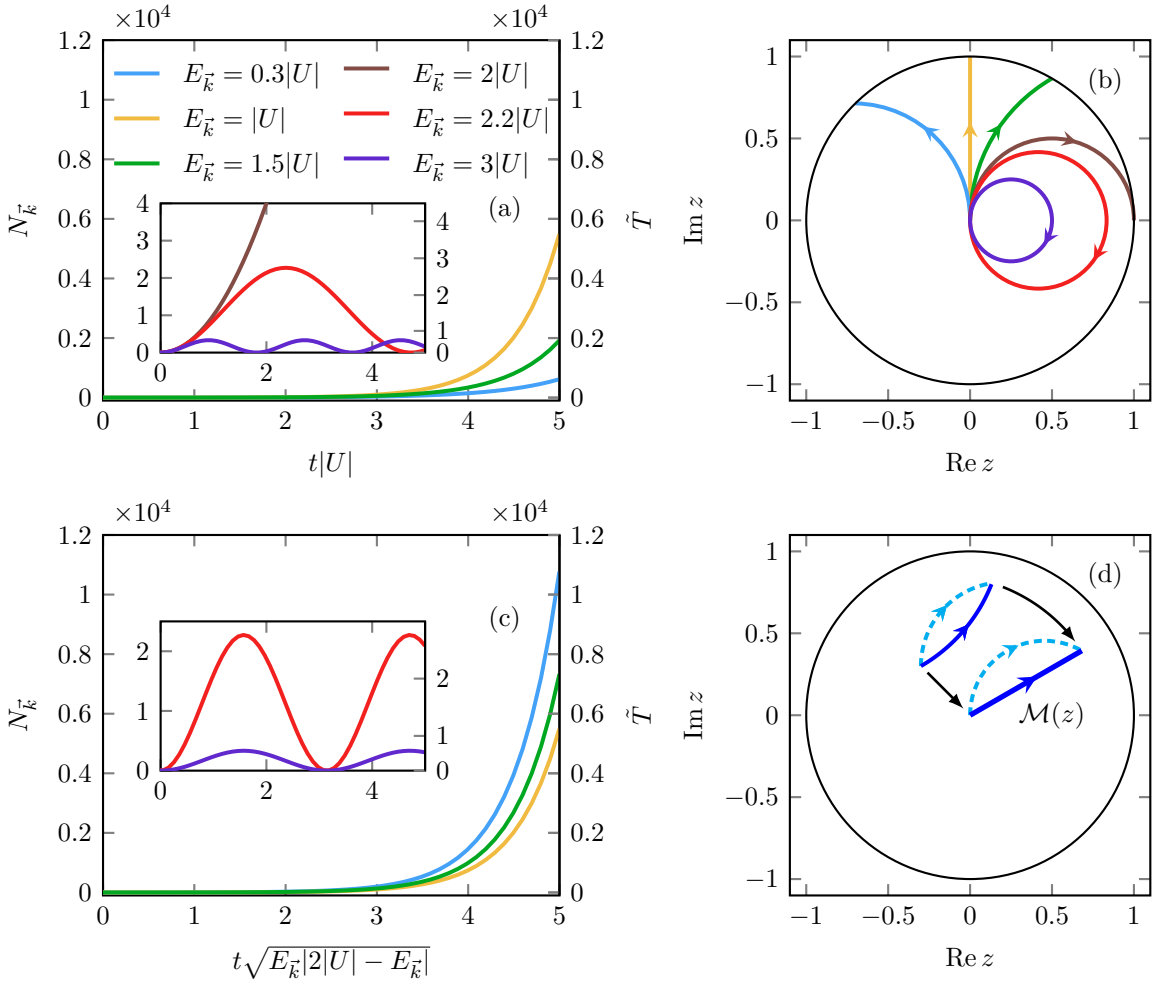

Figure 4.2: The growth of the particle number and the temperature in quench dynamics. (a) The dependence of $N_{\vec{k}}$ (left vertical axis) and the rescaled temperature $\tilde{T}$ (right vertical axis) as a function of time. $\tilde{E}_{\vec{k}} = E_{\vec{k}}/|U|$. The initial state is chosen as a vacuum. $N_{\vec{k}}$ and $\tilde{T}$ of stable modes oscillate periodically. Unstable modes have exponential increases of $N_{\vec{k}}$ and $\tilde{T}$. When U is fixed and $E_{\vec{k}}$ changes, the resonant mode has the fastest growth. (b) The stable(unstable) modes are mapped to closed(open) trajectories on the Poincaré disk. The resonant mode moves along the geodesic. (c) When $|\xi|$ or equivalently, $\sqrt{E_{\vec{k}}(2|U| - E_{\vec{k}})}$, is fixed, the resonant mode has the slowest growth. (d) A Möbius transformation maps an arbitrary initial state to the vacuum at the center of the Poincaré disk. The geodesic becomes a straight line and retains its length.

Euclidean distance to the center of the disk is written as

$$|z(t)| = \begin{cases} \left(1 - \frac{\xi^2}{\xi_1^2+\xi_2^2}\frac{1}{\sinh^2(\frac{|\xi|t}{2})}\right)^{-\frac{1}{2}}, & \xi^2 < 0 \\ \left(1 + \frac{\xi^2}{\xi_1^2+\xi_2^2}\frac{1}{\sin^2(\frac{|\xi|t}{2})}\right)^{-\frac{1}{2}}, & \xi^2 > 0. \end{cases} \tag{4.22}$$

From Eq. (4.22), we see that on the unstable side, $\xi^2 < 0$, if we fix $\xi_1^2 + \xi_2^2$, $|z(t)|$ does grow fastest when $\xi_0 = 0$, i.e., when the system moves along the geodesic. Under this situation,

$$|z(t)|_g = \tanh\left(\frac{|\xi|}{2}t\right). \tag{4.23}$$

On the Poincaré disk, the length should be evaluated based on the metric shown in Eq. (4.14), which leads to the length along the geodesic

$$\tilde{L} = \int_0^{|z(t)|_g} \frac{2dx}{1-x^2} = |\xi|t. \tag{4.24}$$

Using Eq. (4.18), Eq. (4.23) and Eq. (4.24), we can also get

$$\tilde{T} = -\frac{1}{2}\ln^{-1}\tanh\left(\frac{\tilde{L}}{2}\right). \tag{4.25}$$

Thus the three fundamental quantities, including the time, the length in the hyperbolic space, and the temperature are all correlated together.

It is worth pointing out that, once $|\xi|$ is fixed, Eq. (4.22) shows that the geodesic actually corresponds to the slowest growth among all unstable modes. In Fig. 4.2(c), we plot the occupation as a function of rescaled time, $|\xi|t$, we do see that the resonant mode grows slower than other unstable modes.

If the initial scattering length is finite, the ground state is no longer a vacuum and the quantum dynamics starts from a point away from the center of the Poincaré disk. Nevertheless, we can always find an appropriate unitary transformation such that in the new basis, the initial state is a vacuum. Mathematically, this corresponds to a Möbius transformation of the Poincaré disk,

$$z' = \mathcal{M}(z) = \frac{\alpha z + \beta}{\beta^* z + \alpha^*}, \ |\alpha|^2 - |\beta|^2 = 1 \tag{4.26}$$

which preserves the metric Eq. (4.14). Thus all phenomena remain the same compared with starting from a vacuum. In fact, if we pick up $|z_1\rangle$ and $|z_2\rangle$ as the initial and the final state, respectively, we could always allow the quantum dynamics to follow the geodesic, which in

general is not a straight line (Fig. 4.2(d)), using a Hamiltonian (see Appendix 4.7.2),

$$\begin{aligned}\frac{H}{|\xi|} =& \frac{-\operatorname{Im} z_1 z_2^*}{|z_1 - z_2||z_1 z_2^* - 1|}(c_{\vec{k}}^\dagger c_{\vec{k}} + c_{-\vec{k}}^\dagger c_{-\vec{k}}) \\ &+ \frac{i(z_2 - z_1 + |z_1|^2 z_2 - |z_2|^2 z_1)}{2|z_1 - z_2||z_1 z_2^* - 1|} c_{\vec{k}}^\dagger c_{-\vec{k}}^\dagger + \text{h.c.}.\end{aligned} \tag{4.27}$$

To realize the Hamiltonian in Eq. (4.27), it is required that one could tune θ in Eq. (4.2). This can be achieved using a variety of techniques as shown in Sec. 4.5.

4.4 Periodic Drivings and SU(1,1) Spin Echo

We could also use this geometric approach to study periodic drivings. Consider an example that is directly relevant to current experiments [132],

$$H_1 = 2(E_{\vec{k}} + U)K_0 + 2UK_1, \qquad 0 < t < t_1, \tag{4.28}$$

$$H_2 = 2E_{\vec{k}}K_0, \qquad t_1 < t < T_d, \tag{4.29}$$

where the period $T_d = t_1 + t_2$. It corresponds to periodically modifying the interaction strength in Eq. (4.1). We note that when $a_s = 0$, the propagator from $t = t_1$ to $t = T_d$ is given by Eq. (4.12), i.e., a rotation about the center of the Poincaré disk. Though during this time interval, $N_{\vec{k}}$ and $\tilde{T}$ remain unchanged, starting from $t = T_d$, the dynamics becomes drastically different when the interaction is turned on again. Depending on where the trajectory ends at $t = T_d$, the growth of $N_{\vec{k}}$ and $\tilde{T}$ in the second period can be faster or slower than the first period for both the stable and unstable modes. For instance, for a stable mode, in a single quench dynamics, $N_{\vec{k}}$ is always bounded from above. In contrast, a periodic driving can systematically move the system to circles further and further away from the center, and even the stable mode could reach any desired $N_{\vec{k}}$, mimicking a classical object, like a satellite changing its orbitals around the earth step by step. We have verified this phenomenon from numerical calculations as shown in Fig. 4.3(c, d). The growth of $N_{\vec{k}}$ and $\tilde{T}$ can also be slowed down, provided that the trajectory in the second period moves towards the center of the Poincaré disk. For instance, the inflation in an unstable mode can be significantly slowed down, as shown in Fig. 4.3(a, b).

A particularly interesting case is a quantum revival of the initial state at the end of the second period. We emphasize that such a revival is accessible for any initial state, and any H_1 in Eq. (4.28), not requiring a vacuum as the initial state nor a Hamiltonian satisfying the

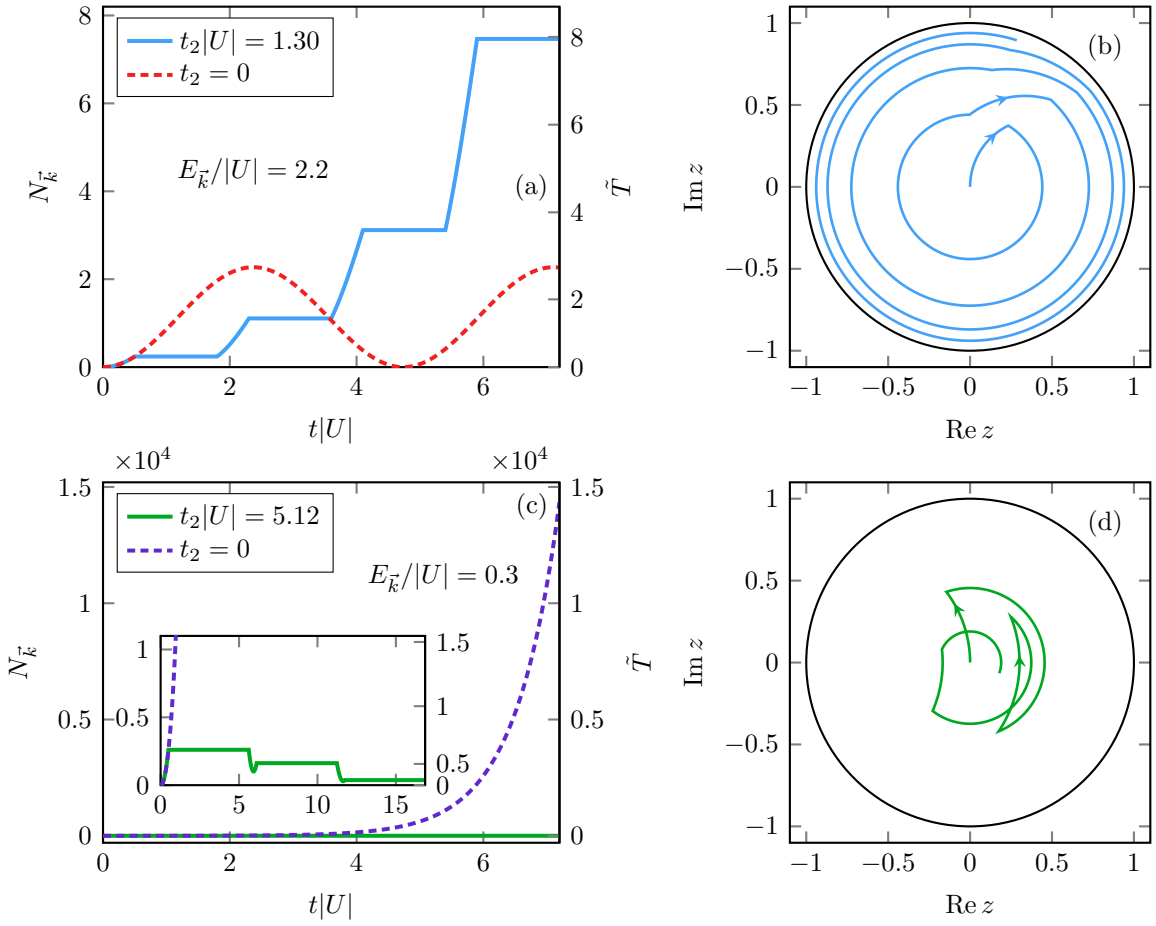

Figure 4.3: Controllable dynamics using periodic drivings. $t_1|U| = 0.5$. (a, b) and (c, d) show results of a stable mode, $E_{\vec{k}}/|U| = 2.2$, and an unstable mode, $E_{\vec{k}}/|U| = 0.3$, respectively. Dashed curves in (a, c) show results of a single quench for comparison, i.e., $t_2 = 0$. Choosing an appropriate t_2, the periodic driving could significantly slow down the dynamics for an unstable mode or speed up the dynamics for a stable mode.

resonant condition [132, 145], provided that appropriate H_2 and t_2 are chosen. We consider an arbitrary $H_1 = w_0K_0 + w_1K_1 + w_2K_2$ with a field strength $w = \sqrt{w_0^2 - w_1^2 - w_2^2}$. The propagator $\mathcal{U}_1 = e^{-iH_1t_1}$ can be decomposed (see derivations in Appendix 4.7.1) as

$$\mathcal{U}_1 = e^{-i\zeta_1 K_0} e^{-i\eta_1 (K_1 \cos\phi_1 + K_2 \sin\phi_1)} e^{-i\zeta_1 K_0}, \tag{4.30}$$

where

$$\zeta_1 = \arctan\left(\frac{w_0}{w} \tan\frac{wt_1}{2}\right) \tag{4.31}$$

$$\phi_1 = \arccos\left(\frac{w_1}{\sqrt{w_1^2 + w_2^2}}\right) \tag{4.32}$$

$$\eta_1 = 2\,\mathrm{arsinh}\left(\frac{\sqrt{w_1^2 + w_2^2}}{w} \sin\left(\frac{wt_1}{2}\right)\right) \tag{4.33}$$

A quantum revival requires that $(\mathcal{U}_2\mathcal{U}_1)^2 = e^{i\gamma}$, where $e^{i\gamma}$ is a global phase factor. Using the identity

$$B(\eta\cos\phi, \eta\sin\phi) R(\pi) B(\eta\cos\phi, \eta\sin\phi) = R(\pi), \tag{4.34}$$

where ϕ and η are two arbitrary real numbers, we conclude that the propagator of H_2, $\mathcal{U}_2 = e^{-iH_2t_2}$, should satisfy

$$\mathcal{U}_2 = R(\pi) B(\eta\cos\phi, \eta\sin\phi) \mathcal{U}_1^{-1} = e^{-i\pi K_0} e^{-i\eta(K_1\cos\phi + K_2\sin\phi)} \mathcal{U}_1^{-1}, \tag{4.35}$$

such that $(\mathcal{U}_2\mathcal{U}_1)^2 = R(\pi)R(\pi) = R(2\pi)$. For the system we considered in this section, $R(2\pi)$ corresponds to a phase factor -1. We thus get an echo which is analogous to the standard spin echo using SU(2) [51], and is applicable in a variety of bosonic systems. Though spin echoes have laid the foundation for many modern quantum techniques, they only apply to systems whose constituents are governed by the $\mathfrak{su}(2)$ algebra. Echoes have never been implemented in bosonic systems where the $\mathfrak{su}(2)$ algebra is no longer relevant. Here, the SU(1,1) echo is applicable in a variety of bosonic systems. $\mathcal{U}_2\mathcal{U}_1$ corresponds to an arbitrary boost followed by a π-rotation, $\mathcal{U}_2\mathcal{U}_1 = R(\pi)B(\eta\cos\phi, \eta\sin\phi)$. Eq. (4.35) readily determines H_2 and t_2. Since ϕ and η are arbitrary, for any H_1, there is a family of H_2, not just a single Hamiltonian, that could lead to the revival.

As an example, if we take $\eta = \eta_1$, $\phi = \phi_1 - \zeta_1$, from Eq. (4.35) and (4.30),

$$\begin{aligned}
\mathcal{U}_2 &= e^{-i\pi K_0} e^{-i\eta(K_1\cos\phi + K_2\sin\phi)} e^{i\zeta_1 K_0} e^{i\eta_1(K_1\cos\phi_1 + K_2\sin\phi_1)} e^{i\zeta_1 K_0} \\
&= e^{-i(\pi-\zeta_1)K_0} e^{-i\zeta_1 K_0} e^{-i\eta(K_1\cos\phi + K_2\sin\phi)} e^{i\zeta_1 K_0} e^{i\eta_1(K_1\cos\phi_1 + K_2\sin\phi_1)} e^{i\zeta_1 K_0} \\
&= e^{-i(\pi-\zeta_1)K_0} e^{-i\eta(K_1\cos(\phi+\zeta_1) + K_2\sin(\phi+\zeta_1))} e^{i\eta_1(K_1\cos\phi_1 + K_2\sin\phi_1)} e^{i\zeta_1 K_0}, \\
&= e^{-i(\pi-2\zeta_1)K_0},
\end{aligned} \tag{4.36}$$

where the corresponding Hamiltonian and evolution time are

$$H_2 = u_0 K_0, \quad t_2 = \frac{\pi - 2\zeta_1}{u_0}, \tag{4.37}$$

and u_0 is an arbitrary number characterizing the energy scale. This means that quenching the scattering length back to zero in Eq. (4.2) during the time interval from t_1 to $t_1 + t_2$ will reverse the quantum dynamics at the end of the second period $t = 2T_d = 2(t_1 + t_2)$, which is precisely what we have seen from the numerical results shown in Fig. 4.4. Alternatively, if we choose different η and ϕ, which correspond to quenching the scattering length to a different value, the trajectory from $t = t_1$ to $t = t_1 + t_2$ is no longer a concentric circle on the Poincaré disk. However, an appropriate t_2 still leads to a quantum revival, as shown in Fig. 4.4(c,d).

If we define $B(\eta\cos\phi, \eta\sin\phi)|z_0\rangle = |z_1'\rangle$, $B(\eta\cos\phi, \eta\sin\phi)|z_1\rangle = |z_0'\rangle$, we see that $z_0 = -z_0'$ and $z_1 = -z_1'$ are satisfied by both cases, providing us with a geometric interpretation of the quantum revival (Fig. 4.4(b,d)). We thus conclude, for any H_1 and t_1, there is a family of H_2 to deliver $e^{-iH_2t_2}e^{-iH_1t_1}e^{-iH_2t_2} = e^{iH_1t_1}$ (up to a global phase faster). The SU(1,1) echo thus effectively creates a reversed evolution based on $-H_1$, an essential ingredient in studying OTOC [42, 43, 46, 47].

4.5 Experimental Realizations

There are multiple means to realize the model in Eq. (4.1).

Shaken lattices In shaken lattices, the single-particle energy can be tuned by hybridizing different bands. In particular, one could create a double-well structure in the momentum space [137]. Therefore, starting from a conventional band structure where a condensate occupies the zero momentum state, suddenly changing the band structure to a double-well one, a pair of particles can be scattered from a condensate to states with opposite momenta.

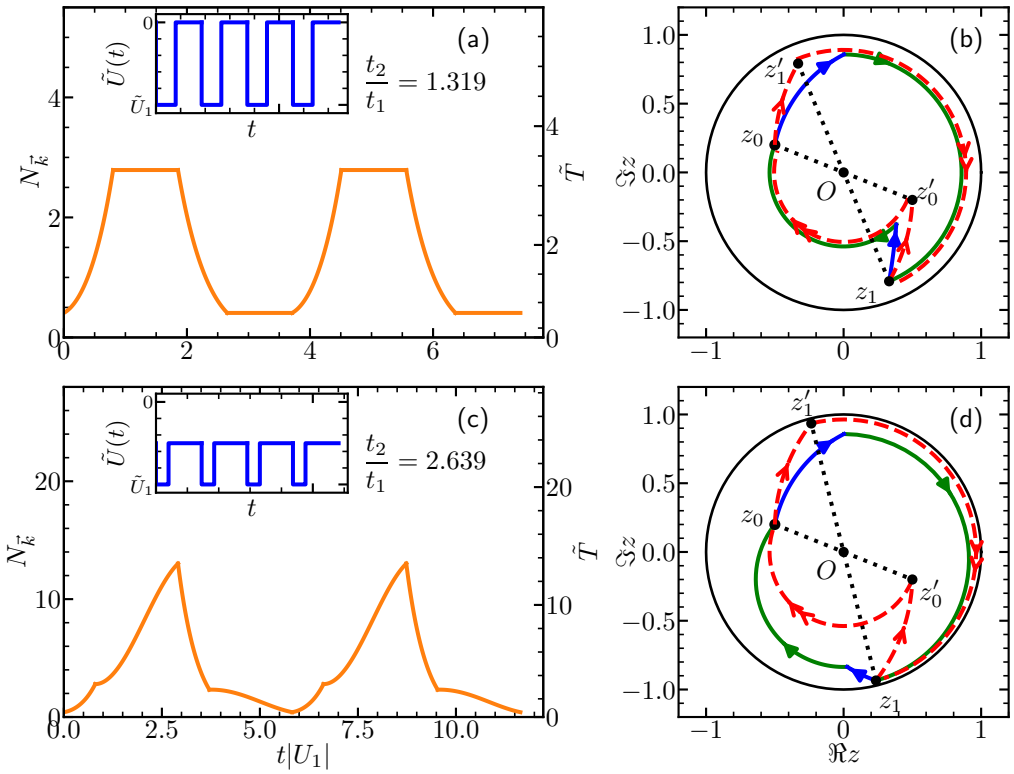

Figure 4.4: Reversing the quantum dynamics. (a,b) and (c,d) show the results of quenching the interaction from U_1 to 0 and $\frac{U_1}{2}e^{-i\pi/2}$ respectively, in the time interval from $t = t_1$ to t_2. $t_1|U_1| = 0.8$, $E_k/|U_1| = 1.3$. Insets show the modulation of interaction strength. In both cases, starting from any initial state z_0, an appropriate t_2 guarantees that the system returns to the initial state after two periods of driving. Blue and green arrowed curves represent $\mathcal{U}_1$ and $\mathcal{U}_2$, respectively. Red dashed curves with single and double arrows denote the boost, $B(\eta\cos\phi, \eta\sin\phi)$, and the rotation, $R(\pi)$, respectively, of $\mathcal{U}_1\mathcal{U}_2$.

The resultant dynamics become similar to the ones discussed in the previous sections.

Spin-orbit coupling A double-well structure in the momentum space can also be created using spin-orbit coupling, as the single-particle dispersions of spin-up and spin-down atoms move towards opposite directions in the k-space [146]. Moreover, the interaction strength also becomes momentum dependent, as the eigenstate is a momentum-dependent superposition of spin-up and spin-down [147]. This provides experimentalists with a new degree of freedom to tune parameters in the model in Eq. (4.1).

Periodic driving Periodically modifying the scattering length could resonantly couple the condensate at zero momentum to a pair of states with opposite momenta. In the rotating wave approximation, the model is the same as the one discussed in the previous section. This scheme was implemented in an experiment done at Chicago [132]. A theoretical work [145] has also studied corrections beyond the rotating wave approximation and used the $\mathfrak{su}(1,1)$ algebra in the calculations to discuss a revival scheme similar to ours. However, the geometrization to hyperbolic surface was not discussed. Another theoretical work [142] discussed the parameterization to the hyperbolic surface but the metric was not explored. Geodesics and their physical meanings, as well as schemes of coherently controlling the dynamics, eluded this work.

Spinor condensates In spinor condensate, there is a well-known spin-mixing term in the Hamiltonian, $a_0^{\dagger 2} a_1 a_{-1} + h.c$, where $a_{m=0,\pm 1}$ are the creation operators at $m_F = 0, \pm 1$ states in the $F = 1$ manifold [14, 148]. This term precisely corresponds to K_1 and K_2 in Eq. (4.3). Using a combination of the magnetic field and the couplings to $F = 2$ manifold, the energy of the three hyperfine spin states are also tunable such that we have $(\epsilon_1+\epsilon_{-1})(a_1^\dagger a_1+a_{-1}^\dagger a_{-1})/2$ in the Hamiltonian [149]. Prepare the initial state as a condensate occupying $m_F = 0$, density-density interactions can be ignored in the timescale where the population at $m_F = \pm 1$ is much smaller than that at $m_F = 0$. The model becomes identical to ours. We point out that, the linear Zeeman splitting, $(\epsilon_1 - \epsilon_{-1})(a_1^\dagger a_1 - a_{-1}^\dagger a_{-1})/2$, commutes with our Hamiltonian and has no effect on the dynamics.

Two-mode squeezing in optics In non-linear medium inside a resonant cavity, the pump beam undergoes spontaneous parametric down-conversion (SPDC) and generates entangled

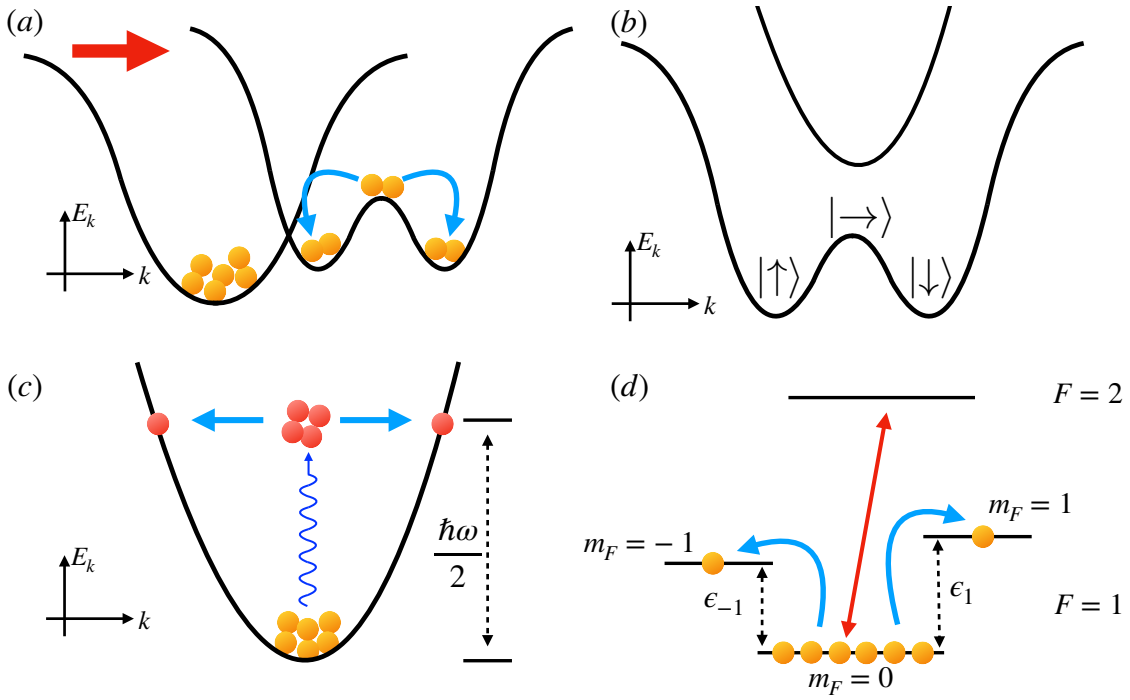

Figure 4.5: (a) Shaking an optical lattice quenches the band structure to a double-well potential in the momentum space. (b) Spin-orbital coupling could also create two minima in the kinetic energy. (c) Periodical driving the interaction strength couples the condensate to a pair of states with opposite momenta. (d) Spin mixing interaction couples the condensate initially occupying $m_F = 0$ to $m_F = \pm 1$. Coupling $|F = 1, m_F = 0\rangle$ and $|F = 2, m_F = 0\rangle$ allows one to control the phase of U.

photon pairs, which couples resonant modes and causes two-mode squeezing. The coupling term is controlled by the external pump field [150]. Starting from the two-modes vacuum and turning on the pump field, the dynamics is captured by Eq. (4.1).

4.5.1 Changing the phase of U

As for the realization discussed in Sec. 4.1, since $U = \frac{4\pi\hbar a_s}{m}\Psi_0^2$, adding a phase to Ψ_0 could change the phase of U. This can be achieved using a pulse of Bragg scattering, as shown in Fig. 4.6. The Bragg beams couple a momentum state $|\vec{k}\rangle$ to another one $|\vec{k} + \vec{Q}\rangle$. When the transition is off-resonance, the Bragg coupling leads to a shift of the energy of $|\vec{k}\rangle$,

$$\delta E_{\vec{k}} = -\frac{\Omega^2}{\Delta_{\vec{k}}} = -\frac{\Omega^2}{E_{\vec{k}+\vec{Q}} - E_{\vec{k}} - \hbar\omega}, \tag{4.38}$$

where Ω is the coupling strength of Bragg scattering, ω and $\vec{Q}$ are the differences in the frequency and momentum of these two beams. Therefore, such a pulse provides $|\vec{k}\rangle$ a phase

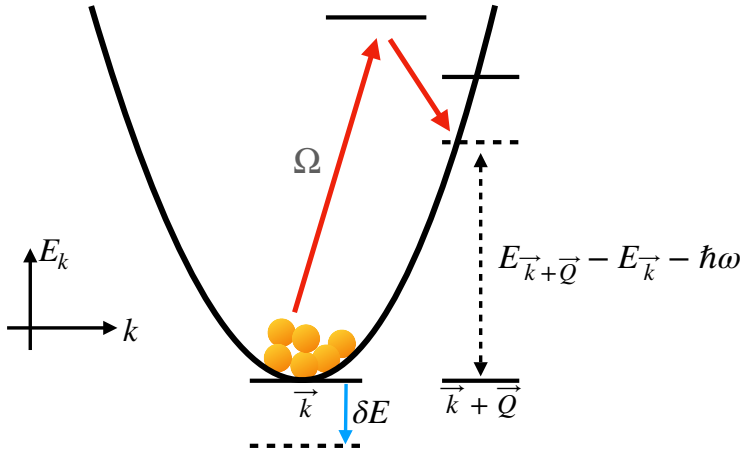

Figure 4.6: A Bragg scattering couples $|\vec{k}\rangle$ and $|\vec{k}+\vec{Q}\rangle$. An off-resonance coupling shifts the energy of $|\vec{k}\rangle$ by $\delta E_{\vec{k}}$ and a pulse with duration τ adds a phase to the Hamiltonian in Eq. (4.1).

shift $e^{-i\delta\varphi_{\vec{k}}} = e^{-i\delta E_{\vec{k}}\tau}$, where τ is the duration of the pulse. For fixed $\vec{Q}$ and ω, $\delta E_{\vec{k}}$ is a linear function of $\vec{k}$. Therefore, the condensate at zero momentum acquires a different phase compared to state at a finite momentum $\vec{k}$ that we are interested in. Effectively, we have added an phase $\phi = 2\delta\varphi_0 - \delta\varphi_{\vec{k}} - \delta\varphi_{-\vec{k}}$ to the Hamiltonian in Eq. (4.1). This method is also applicable to the first three realizations discussed in the previous section.

As for spinor condensate, this scheme can be even simpler as we have discrete hyperfine spin states other than the continuum in the momentum space. We could selectively couple $|1,0\rangle$ to a state in the $F = 2$ manifold, such as $|2,0\rangle$, as shown in Fig. 4.5(d). The other two hyperfine spin states are not affected or weakly coupled. Then the phase of U is also controllable. As for two-mode squeezing, U corresponds to an external field and its phase can be easily controlled.

4.5.2 Modulating the scattering length

The magnetic Feshbach resonance is a standard technique to deliver a time-dependent scattering length, $a_s(t)$. For instance, the experiment done at Chicago used BEC of ^{133}Cs atoms in the hyperfine state $|F = 3, m_F = 3\rangle$ [132]. An external magnetic field was modulated around 17.22G such that the scattering length oscillates in a fashion of $a_{dc} + a_{ac}\sin\omega t$, where ω is the modulation frequency of the magnetic field, a_{dc} is the stationary part of a_s and a_{ac} denotes the amplitude of the oscillation.

In reality, it takes a a finite time to change the magnetic field unlike the optical Feshbach

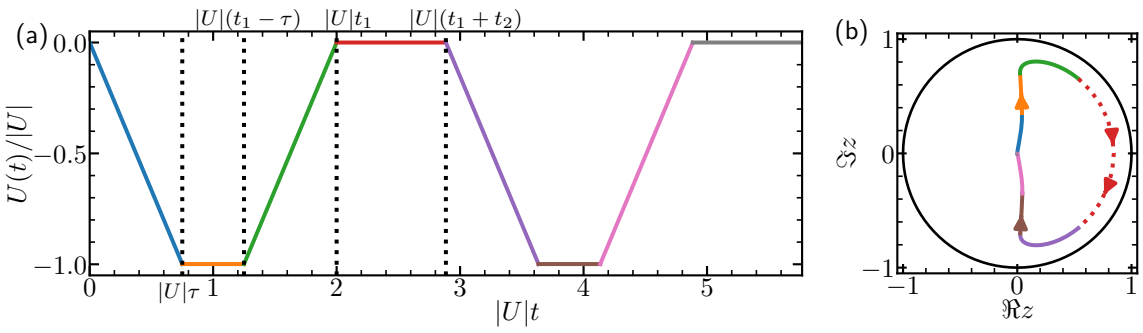

Figure 4.7: (a) $U(t)$ is linearly turned on and off within a time τ. $|U|\tau = 0.75$, and $|U|t_1 = 2.0$. $|U|t_2$ is obtained from numerics such that the mode with $E_{\vec{k}}/|U| = 1$ is recovered by the echo. (b) The corresponding trajectory on the Poincaré disk. The initial state is chosen as the vacuum. Solid and dotted curves represent $\mathcal{U}_1$ and $\mathcal{U}_2$, respectively.

resonance that could easily give rise to an abrupt change in a_s. It is, therefore, desired to consider a generic time-dependence of a_s in addition to the quench dynamics. For any time-dependent Hamiltonian, $H(t) = 2(E_{\vec{k}} + U(t))K_0 + 2U(t)K_1$, where $U(t) = 4\pi\hbar^2 \frac{a_s(t)}{M}\Psi_0^2$. For an arbitrary $U(t)$, the propagator $\mathrm{T}e^{\int_0^{t_1} -iH(t')dt'}$, where T is the time-ordering operator, is still an element in the SU(1,1) group. It thus can be rewritten as $\exp(-iH_{\text{eff}}t_1)$, where $H_{\text{eff}} = w_0K_0 + w_1K_1 + w_2K_2$ is time-independent. Whereas the exact expressions of $w_{0,1,2}$ depend on the explicit form of $U(t)$, $\exp(-iH_{\text{eff}}t_1)$ can always be decomposed to a boost and a rotation, as discussed in Sec. 4.4. Therefore the SU(1,1) echoes still apply.

To demonstrate the SU(1,1) echoes for a generic $U(t)$, we consider linearly turning on and off the scattering length a_s. The time dependent $U(t)$ is shown in Fig. 4.7. The H_{eff} and the corresponding t_2 required for the SU(1,1) echo is obtained numerically. The trajectory on the Poincaré disk is also shown.

Alternatively, the optical Feshbach resonance could be implemented so as to change the scattering length fast enough compared to other time scales relevant to many-body physics such as the interaction strength [151, 152]. A quench dynamics can then be realized.

4.6 Conclusions and Outlook

In this chapter, we have geometrized quantum dynamics of weakly interacting BECs. From the theoretical side, this approach unfolds the intrinsic geometry behind the dynamical instability and a wide range of other quantum dynamical phenomena. It also allows us to correlate fundamental quantities, including the time, the temperature, the length, and the

fidelity, on a Poincaré disk. In practice, this geometric scheme allows us to design SU(1,1) echoes to coherently control many-body dynamics of bosonic systems. Since constituents of these systems do not satisfy the $\mathfrak{su}(2)$ algebra, the celebrated spin echoes no longer apply. Our SU(1,1) echoes serve as a new tool to manipulate quantum dynamics of such bosonic systems. For instance, starting from any initial state, the Poincaré disk allows us to design a family of Hamiltonians that could reverse the dynamical evolution, providing experimentalists a powerful scheme to recover the initial state without changing the sign of the original Hamiltonian.

To concretize the discussions, we have been focusing on a class of systems corresponding to one representation of the SU(1,1) group. We need to emphasize that our results are very generic and this geometric approach applies to systems corresponding to other representations of the SU(1,1) group. In ultracold atoms, three-dimensional unitary fermions and two-dimensional bosons and fermions with contact interactions are well-known systems that also exhibit the SU(1,1) (or SO(2,1)) symmetry [153, 154]. Our results can be straightforwardly generalized to those systems. For instance, the underlying symmetry of two-dimensional BECs was recently studied in an elegant experiment [155]. The Poincaré disk and our SU(1,1) echoes could be directly implemented to control quantum dynamics of these BECs and understand the distinct behaviors of breathers of different shapes.

Whereas we have discussed propagators generated by $\mathfrak{su}(1,1)$, our geometric approach can be generalized to a broad class of models that are captured by other algebras. We hope that our work will stimulate more theoretical and experimental efforts to unfold the intrinsic entanglement between dynamics, algebras, and geometries.

4.7 Appendix

4.7.1 Calculations in the Heisenberg picture

In this section, we show how to calculate the dynamical evolution in the Heisenberg picture as a supplement to Sec. 4.3 and 4.4. We consider the Hamiltonian of the following form,

$$H = 2\epsilon_0 K_0 + 2\epsilon_1 K_1 \cos\theta + 2\epsilon_1 K_2 \sin\theta \tag{4.39}$$

$$= \epsilon_0 (c^\dagger_{\vec{k}} c_{\vec{k}} + c_{-\vec{k}} c^\dagger_{-\vec{k}}) + e^{-i\theta}\epsilon_1 c^\dagger_{\vec{k}} c^\dagger_{-\vec{k}} + h.c. \tag{4.40}$$

where we assume that $\epsilon_0, \epsilon_1, \theta \in \mathbb{R}$. We focus on how the creation and annihilation operators, $c^\dagger_{\vec{k}}(t)$ and $c_{\vec{k}}(t)$, evolve in the Heisenberg picture,

$$\frac{\mathrm{d}c_{\vec{k}}(t)}{\mathrm{d}t} = i[H, c_{\vec{k}}(t)] = -i\epsilon_0 c_{\vec{k}}(t) - ie^{-i\theta}\epsilon_1 c^\dagger_{-\vec{k}}(t), \tag{4.41}$$

$$\frac{\mathrm{d}c^\dagger_{-\vec{k}}(t)}{\mathrm{d}t} = i[H, c^\dagger_{-\vec{k}}(t)] = i\epsilon_0 c^\dagger_{-\vec{k}}(t) + ie^{i\theta}\epsilon_1 c_{\vec{k}}(t). \tag{4.42}$$

The solution for $\epsilon_0^2 \neq \epsilon_1^2$ is

$$\begin{bmatrix} c_{\vec{k}}(t) \\ c^\dagger_{-\vec{k}}(t) \end{bmatrix} = \begin{bmatrix} \cos\epsilon t - i\frac{\epsilon_0}{\epsilon}\sin\epsilon t & -ie^{-i\theta}\frac{\epsilon_1}{\epsilon}\sin\epsilon t \\ ie^{i\theta}\frac{\epsilon_1}{\epsilon}\sin\epsilon t & \cos\epsilon t + i\frac{\epsilon_0}{\epsilon}\sin\epsilon t \end{bmatrix} \begin{bmatrix} c_{\vec{k}} \\ c^\dagger_{-\vec{k}} \end{bmatrix}, \tag{4.43}$$

where $\epsilon = \sqrt{\epsilon_0^2 - \epsilon_1^2}$. For $\epsilon_0^2 = \epsilon_1^2$,

$$\begin{bmatrix} c_{\vec{k}}(t) \\ c^\dagger_{-\vec{k}}(t) \end{bmatrix} = \begin{bmatrix} 1 - i\epsilon_0 t & -ie^{-i\theta}\epsilon_1 t \\ ie^{i\theta}\epsilon_1 t & 1 + i\epsilon_0 t \end{bmatrix} \begin{bmatrix} c_{\vec{k}} \\ c^\dagger_{-\vec{k}} \end{bmatrix}. \tag{4.44}$$

We then define

$$\Gamma(\epsilon_0, \epsilon_1, \theta, t) = \begin{bmatrix} \cos\epsilon t - i\epsilon_0 t\,\mathrm{sinc}\,\epsilon t & -ie^{-i\theta}\epsilon_1 t\,\mathrm{sinc}\,\epsilon t \\ ie^{i\theta}\epsilon_1 t\,\mathrm{sinc}\,\epsilon t & \cos\epsilon t + i\epsilon_0 t\,\mathrm{sinc}\,\epsilon t \end{bmatrix}, \tag{4.45}$$

which covers both the two cases.

Decomposition of an arbitrary propagator With Eq. (4.45), to prove the decomposition of the propagator in Eq. (4.30), we just need show that

$$\Gamma(\frac{w_0}{2}, \frac{\sqrt{w_1^2 + w_2^2}}{2}, \arctan\left(\frac{w_2}{w_1}\right), t_1) = \Gamma(\frac{\zeta_1}{2}, 0, 0, 1)\Gamma(0, \frac{\eta_1}{2}, \phi_1, 1)\Gamma(\frac{\zeta_1}{2}, 0, 0, 1), \tag{4.46}$$

which can be verified by simple matrix multiplications.

Particle number growth Now we can calculate the quench dynamics in Sec. 4.3. In the Hamiltonian after quench (Eq. (4.21)),

$$\epsilon_0 = E_k - |U|,\ \epsilon_1 = -|U|,\ \theta = 0. \tag{4.47}$$

The initial state is a vacuum, so particle number at any time t is

$$N_{\vec{k}}(t) = \langle 0, 0|\, c^\dagger_{\vec{k}}(t) c_{\vec{k}}(t)\, |0, 0\rangle\,. \tag{4.48}$$

Eq. (4.45) tells us the analytical expressions of the creation and annihilation operators at any time t. Therefore it can be shown that

$$N_{\vec{k}}(t) = |U|^2 t^2 \,\mathrm{sinc}^2 \sqrt{(E_k - |U|)^2 - |U|^2}\, t, \tag{4.49}$$

which applies to both stable and unstable modes. Therefore we see when $(E_k - |U|)^2 - |U|^2 > 0$ or $E_k > 2|U|$, $N_{\vec{k}}(t)$ is bounded, while when $(E_k - |U|)^2 - |U|^2 < 0$ or $E_k < 2|U|$, sin becomes sinh and $N_{\vec{k}}(t)$ grows exponentially. Eq. (4.49) can also be derived from Eqs. (4.16) and (4.30).

SU(1,1) spin echo We first prove the identity Eq. (4.34). Using the conclusions above, we need to verify

$$\Gamma(0, \frac{\eta}{2}, \phi, 1)\Gamma(\frac{\pi}{2}, 0, 0, 1)\Gamma(0, \frac{\eta}{2}, \phi, 1) = \Gamma(\frac{\pi}{2}, 0, 0, 1), \tag{4.50}$$

that is,

$$\begin{bmatrix} \cosh\frac{\eta}{2} & -ie^{-i\phi}\sinh\frac{\eta}{2} \\ ie^{i\phi}\sinh\frac{\eta}{2} & \cosh\frac{\eta}{2} \end{bmatrix} \begin{bmatrix} -i & 0 \\ 0 & i \end{bmatrix} \begin{bmatrix} \cosh\frac{\eta}{2} & -ie^{-i\phi}\sinh\frac{\eta}{2} \\ ie^{i\phi}\sinh\frac{\eta}{2} & \cosh\frac{\eta}{2} \end{bmatrix} = \begin{bmatrix} -i & 0 \\ 0 & i \end{bmatrix}, \tag{4.51}$$

which is easy to be done.

Next, we can double-check Eq. (4.37), the Hamiltonian that is used to reverse a previous Hamiltonian and make an echo. We need to show such a Hamiltonian can satisfy Eq. (4.35):

$$\mathcal{U}_2\mathcal{U}_1 = e^{-iH_2t_2}e^{-iH_1t_1} = R(\pi)B(\eta\cos\phi, \eta\sin\phi). \tag{4.52}$$

Again, using the method above, we just need to verify

$$\Gamma(2u_0, 0, 0, \frac{\pi - 2\zeta_1}{u_0})\Gamma(E_{\vec{k}} + U, U, 0, t_1) = \Gamma(\frac{\pi}{2}, 0, 0, 1)\Gamma(0, \frac{\eta}{2}, \phi, 1), \tag{4.53}$$

where $\eta = \eta_1$, $\phi = \phi_1 - \zeta_1$. Using the definition of η_1 and ϕ_1 from Eq. (4.30), this equation can be verified.

4.7.2 Connecting two states along a geodesic

We now find out the Hamiltonian that can evolve one TFD $|z_1\rangle$ to another $|z_2\rangle$ along the geodesic of the Poincaré disk, which is the one in Eq. (4.27). Our strategy is first considering the simple case where $z_1 = 0$. Then for the general case, we do a unitary transformation such that z_1 becomes 0 and z_2 becomes z_2' and we can therefore use the result from the simple case.

Finally we transform the result back to the original basis. This implies a prerequisite, that if the system is moving along a geodesic of the Poincaré disk, after any unitary transformation of the basis, it will also move along a geodesic in the new basis. To prove this, we consider an arbitrary TFD state $|z\rangle$ and an arbitrary unitary transformation in the SU(1,1) group $\mathcal{U} = e^{-i(x_0K_0+x_1K_1+x_2K_2)}$. With the decomposition in Eq. (4.30),

$$\begin{aligned}\mathcal{U}|z\rangle =& e^{-i\zeta K_0}e^{-i\eta(K_1\cos\phi+K_2\sin\phi)}e^{-i\zeta K_0}\sqrt{1-|z|^2}\sum_n z^n|n\rangle_{\vec{k}}|n\rangle_{-\vec{k}}\\ =& e^{-i\zeta K_0}e^{-i\frac{\eta}{2}(e^{-i\phi}c^\dagger_{\vec{k}}c^\dagger_{-\vec{k}}+e^{i\phi}c_{\vec{k}}c_{-\vec{k}})}e^{-i\frac{\zeta}{2}}\sqrt{1-|z|^2}\sum_n(ze^{-i\zeta})^n|n\rangle_{\vec{k}}|n\rangle_{-\vec{k}},\end{aligned} \tag{4.54}$$

where

$$\zeta = \arctan\Big(\frac{x_0}{x}\tan\frac{x}{2}\Big), \tag{4.55}$$

$$\phi = \arccos\frac{x_1}{\sqrt{x_1^2+x_2^2}}, \tag{4.56}$$

$$\eta = 2\,\mathrm{arsinh}(\frac{\sqrt{x_1^2+x_2^2}}{x}\sin\frac{x}{2}), \tag{4.57}$$

$$x = \sqrt{x_0^2-x_1^2-x_2^2}. \tag{4.58}$$

Introducing $d^\dagger_{\vec{k}} = e^{-i\phi}c^\dagger_{\vec{k}}$ and defining $|n\rangle'_{\vec{k}} = \frac{1}{\sqrt{n!}}d^{\dagger n}_{\vec{k}}|0\rangle_{\vec{k}}$,

$$\begin{aligned}\mathcal{U}|z\rangle &= e^{-i\zeta K_0}e^{-i\frac{\eta}{2}(d^\dagger_{\vec{k}}c^\dagger_{-\vec{k}}+d_{\vec{k}}c_{-\vec{k}})}e^{-i\frac{\zeta}{2}}\sqrt{1-|z|^2}\sum_n(ze^{-i(\zeta-\phi)})^n|n\rangle'_{\vec{k}}|n\rangle_{-\vec{k}}\\ &= e^{-i\zeta K_0}e^{-i\frac{\eta}{2}(d^\dagger_{\vec{k}}c^\dagger_{-\vec{k}}+d_{\vec{k}}c_{-\vec{k}})}e^{-i\frac{\zeta}{2}}\frac{\sqrt{1-|z|^2}}{\mathrm{sech}\,\frac{\gamma}{2}}\,\mathrm{sech}\,\frac{\gamma}{2}\sum_n(-i\tanh\frac{\gamma}{2})^n|n\rangle'_{\vec{k}}|n\rangle_{-\vec{k}},\end{aligned} \tag{4.59}$$

where $\gamma = 2\,\mathrm{artanh}\,ize^{-i(\zeta-\phi)}$. To proceed the derivation, we will use the identity

$$e^{-i\frac{y}{2}(a^\dagger b^\dagger+ab)}|0\rangle_a|0\rangle_b = \mathrm{sech}\,\frac{y}{2}\sum_n(-i\tanh\frac{y}{2})^n|n\rangle_a|n\rangle_b, y\in\mathbb{R}, \tag{4.60}$$

and analytically extend y from $\mathbb{R}$ to $\mathbb{C}$. Then

$$\begin{aligned}
\mathcal{U}\left|z\right\rangle &= e^{-i\frac{\zeta}{2}}\frac{\sqrt{1-|z|^2}}{\operatorname{sech}\frac{\gamma}{2}}e^{-i\zeta K_0}e^{-i\frac{\eta+\gamma}{2}(d^\dagger_{\vec{k}}c^\dagger_{-\vec{k}}+d_{\vec{k}}c_{-\vec{k}})}\left|0\right\rangle_{\vec{k}}\left|0\right\rangle_{-\vec{k}} \\
&= e^{-i\frac{\zeta}{2}}\frac{\sqrt{1-|z|^2}}{\operatorname{sech}\frac{\gamma}{2}}e^{-i\zeta K_0}\operatorname{sech}\frac{\eta+\gamma}{2}\sum_n(-i\tanh\frac{\eta+\gamma}{2})^n\left|n\right\rangle'_{\vec{k}}\left|n\right\rangle_{-\vec{k}} \\
&= e^{-i\zeta}\frac{\sqrt{1-|z|^2}}{\operatorname{sech}\frac{\gamma}{2}}\operatorname{sech}\frac{\eta+\gamma}{2}\sum_n(-ie^{-i\zeta}\tanh\frac{\eta+\gamma}{2})^n\left|n\right\rangle'_{\vec{k}}\left|n\right\rangle_{-\vec{k}} \\
&= e^{-i\zeta}\frac{\sqrt{1-|z|^2}}{\operatorname{sech}\frac{\gamma}{2}}\operatorname{sech}\frac{\eta+\gamma}{2}\sum_n(-ie^{-i(\zeta+\phi)}\tanh\frac{\eta+\gamma}{2})^n\left|n\right\rangle_{\vec{k}}\left|n\right\rangle_{-\vec{k}}.
\end{aligned} \tag{4.61}$$

Now we know that the final state $\left|z'\right\rangle$ is located at

$$z' = -ie^{-i(\zeta+\phi)}\tanh\frac{\eta+\gamma}{2} \tag{4.62}$$

$$= -ie^{-i(\zeta+\phi)}\tanh\left(\frac{\eta}{2}+\operatorname{artanh}ize^{-i(\zeta-\phi)}\right) \tag{4.63}$$

$$= -ie^{-i(\zeta+\phi)}\frac{e^{-i(\zeta-\phi)}(e^\eta+1)z+i(1-e^\eta)}{e^{-i(\zeta-\phi)}(e^\eta-1)z-i(e^\eta+1)} \tag{4.64}$$

$$= \frac{ze^{-i\zeta}\cosh\frac{\eta}{2}-ie^{-i\phi}\sinh\frac{\eta}{2}}{zie^{i\phi}\sinh\frac{\eta}{2}+e^{i\zeta}\cosh\frac{\eta}{2}} \tag{4.65}$$

This is actually a Möbius transformation defined in Eq. (4.26) where

$$\alpha = e^{-i\zeta}\cosh\frac{\eta}{2},\ \beta = -ie^{-i\phi}\sinh\frac{\eta}{2}. \tag{4.66}$$

Mathematicians already tell us that such a Möbius transformation preserves the metric, so an original geodesic is still a geodesic in the new basis. Therefore we have proved the prerequisite.

Now as planed, first, we notice that starting from the center of the Poincaré disk, $z = 0$, which is a vacuum, a pure boost along a fixed direction ϕ will move the system along a radius of the disk,

$$B(\eta\cos\phi,\eta\sin\phi)\left|0\right\rangle = e^{-i\frac{\eta}{2}(c^\dagger_{\vec{k}}c^\dagger_{-\vec{k}}e^{-i\phi}+c_{\vec{k}}c_{-\vec{k}}e^{i\phi})}\left|0\right\rangle = \left|z=-ie^{-i\phi}\tanh\frac{\eta}{2}\right\rangle. \tag{4.67}$$

As η grows, the final point z moves along the direction ϕ until $\tanh\eta$ approaches 1, which is the boundary of the Poincaré disk. On the other hand, we know any straight line passing through the center of the Poincaré disk is one of its geodesics. Therefore, if $z_1 = 0$, to connect z_1 with z_2 along a geodesic, we just need a Hamiltonian corresponding to a pure

boost. To be specific, the Hamiltonian should be of the following form

$$\frac{H}{|\xi|} = \frac{iz_2}{2|z_2|} c^\dagger_{\vec{k}} c^\dagger_{-\vec{k}} + h.c. \tag{4.68}$$

Next, if z_1 is not zero, we first introduce a transformation $\mathcal{U}$ that transforms z_1 to 0. From Eq. (4.15), by definition, such a transformation is

$$\mathcal{U} = R(-\varphi_0)^\dagger B(-\varphi_1) R(-\varphi_0), \tag{4.69}$$

$$\varphi_0 = i \ln \frac{iz_1}{|z_1|}, \ \varphi_1 = 2 \operatorname{artanh} |z_1|. \tag{4.70}$$

At the same time, z_2 is transformed to z_2',

$$\mathcal{U} |z_2\rangle = e^{-i\varphi_0 K_0} e^{i\varphi_1 K_1} e^{i\varphi_0 K_0} |z_2\rangle \tag{4.71}$$

$$= e^{-2i\varphi_0 K_0} e^{i\varphi_0 K_0} e^{i\varphi_1 K_1} e^{i\varphi_0 K_0} |z_2\rangle \tag{4.72}$$

From Eq. (4.65), After the first 3 operators, z_2 is transformed to z_2''

$$z_2 \to z_2'' = \frac{z_2 e^{i\varphi_0} \cosh \frac{\varphi_1}{2} + i \sinh \frac{\varphi_1}{2}}{-iz_2 \sinh \frac{\varphi_1}{2} + e^{-i\varphi_0} \cosh \frac{\varphi_1}{2}} = \frac{z_1^*}{z_1} \cdot \frac{z_2 - z_1}{z_2 z_1^* - 1}, \tag{4.73}$$

and the final $e^{-2i\varphi_0 K_0}$ transforms z_2'' to z_2',

$$z_2' = e^{-2i\varphi_0} \cdot \frac{z_1^*}{z_1} \cdot \frac{z_2 - z_1}{z_2 z_1^* - 1} = \frac{z_1 - z_2}{z_1^* z_2 - 1}. \tag{4.74}$$

Using the previous result Eq. (4.68), the Hamiltonian that connects z_2' and 0 along the geodesic is

$$\frac{H}{|\xi|} = \frac{iz_2'}{2|z_2'|} c'^\dagger_{\vec{k}} c'^\dagger_{-\vec{k}} + h.c., \tag{4.75}$$

where $c'^\dagger_{\vec{k}}$ and $c'_{\vec{k}}$ are the creation and annihilation operators transformed from $c^\dagger_{\vec{k}}$ and $c_{\vec{k}}$ by $\mathcal{U}$. Using the results from Appendix 4.7.1,

$$\begin{bmatrix} c'_{\vec{k}} \\ c'^\dagger_{-\vec{k}} \end{bmatrix} = \Gamma(\frac{\varphi_0}{2}, 0, 0, 1)\Gamma(0, -\frac{\varphi_1}{2}, 0, 1)\Gamma(-\frac{\varphi_0}{2}, 0, 0, 1) \begin{bmatrix} c_{\vec{k}} \\ c^\dagger_{-\vec{k}} \end{bmatrix} \tag{4.76}$$

After we do the substitution, we will get Eq. (4.27).

4.7.3 Trajectory of the quench dynamics at the critical point

In this section we discuss the critical point $E_k = 2|U|$ in Sec. 4.3, where the field strength ξ^2 vanishes. Assuming the initial state is vacuum, from Eq. (4.30), we get the position of

the system on the Poincaré disk at any time t,

$$z = -i \tanh \operatorname{arsinh}(\frac{\xi_0}{\xi} \sin\left(\frac{\xi}{2}t\right)) e^{-i \arctan\left(\frac{\xi_0}{\xi} \tan\left(\frac{\xi}{2}t\right)\right)}. \tag{4.77}$$

The polar coordinates (r, θ) are

$$r = \tanh \operatorname{arsinh}(\frac{\xi_0}{\xi} \sin\left(\frac{\xi}{2}t\right)), \tag{4.78}$$

$$\theta = -\arctan\left(\frac{\xi_0}{\xi} \tan\left(\frac{\xi}{2}t\right)\right) - \frac{\pi}{2}. \tag{4.79}$$

We also evaluate the velocity,

$$v_r = \dot{r} = \frac{\xi_0 \cos\frac{\xi t}{2}}{2(1 + \frac{\xi_0^2}{\xi^2}\sin^2\frac{\xi t}{2})^{3/2}}, \tag{4.80}$$

$$v_\theta = r\dot{\theta} = -\frac{\frac{\xi_0}{\xi}\sin\left(\frac{\xi}{2}t\right)}{\sqrt{1 + \frac{\xi_0^2}{\xi^2}\sin^2\frac{\xi t}{2}}} \frac{\xi_0 \sec^2\frac{\xi t}{2}}{2 + 2\frac{\xi_0^2}{\xi^2}\tan^2\frac{\xi t}{2}} \tag{4.81}$$

The ratio is

$$\frac{v_r}{v_\theta} = -\frac{1 + \frac{\xi_0^2}{\xi^2}\tan^2\frac{\xi t}{2}}{1 + \frac{\xi_0^2}{\xi^2}\sin^2\frac{\xi t}{2}} \frac{\cos^3\frac{\xi t}{2}}{\frac{\xi_0}{\xi}\sin\frac{\xi t}{2}} \tag{4.82}$$

For the unstable modes, ξ is imaginary. In the limit of $t \to \infty$,

$$\lim_{t\to\infty} \frac{v_r}{v_\theta} = -\frac{1 + \frac{\xi_0^2}{|\xi|^2}}{\frac{\xi_0^3}{|\xi|^3}}. \tag{4.83}$$

This means the trajectory will eventually intersect with the boundary of the Poincaré disk. Now we take the limit $\xi \to 0$,

$$\lim_{\xi\to 0}\lim_{t\to\infty} \frac{v_r}{v_\theta} = 0. \tag{4.84}$$

So for the critical point $\xi = 0$, the velocity is perpendicular to the radial direction and the trajectory becomes tangent to the boundary of the Poincaré disk.

5. DETECTING QUANTUM MANY-BODY PHASES FROM THE DECOHERENCE OF A SINGLE IMPURITY

One of the goals of quantum simulation is to explore the rich properties of quantum many-body physics and one long-term aim is to gain a better understanding of the thermalization process of a local subsystem interacting with the remaining part. Ultracold atom experiments studying impurities immersed in a Bose-Einstein condensate [156–160] or a Fermi gas [161–164] have provided a fascinating platform, because of the ability to engineer the quantum states of both the subsystem and remaining environment and fine tune the in-between interaction. With the proceedings in single particle control [5, 6], experimentalists have been able to embed an individual charged or neutral particle into a condensate and track the position or spin degree of freedom in the single particle level. By studying the dynamics of the impurity, the information about the external condensate, such as the density distribution [156, 159, 165, 166], the phononic excitations [167], and temperature fluctuations [160], can be extracted. The technique of tuning and tracking the interaction also opens new perspectives for engineering quantum states [168, 169] and cooling qubits [170], which have potential applications in quantum computing.

Motivated by the recent experiments by Schmidt, et al. [159], instead of considering a spin-3 impurity, in this chapter, we study the dynamics of a single spin-1/2 impurity interacting with a spin-1 BEC of various initial states. We provide a concrete example of determining the phase of the environment BEC by looking at the dynamics of the impurity. We find that, depending on the initial state of the environment, the coherence of the spin impurity has different behaviors. If the environment is a spin singlet, the spin impurity keeps in a pure state. If the environment is a ferromagnetic state, the coherence of the impurity shows simple oscillations. Thus in these two cases no decoherence occurs. However if the environment is a polar state, at the time inversely proportional to the impurity-BEC interaction strength, the coherence of the impurity quickly decreases to a finite value and revives after a longer time scale. The residual coherence is also affected by external magnetic fields. Thus by measuring the coherence of the single impurity embedded in the condensate, we can detect the phase of a spinor condensate. Our work is in well reach of current ultracold atom experimental platforms.

5.1 Spin Impurity Interacting with a Spinor BEC

We consider a single spin-1/2 impurity immersed in a spin-1 condensate containing N bosons. The impurity has Heisenberg interactions with all the bosons. Therefore the BEC is the environment seen by the impurity. The total Hamiltonian is

$$H = B_s S_z + c_2 \left(\sum_{i=1}^{N} \vec{I}_i \right)^2 + B_e \sum_{i=1}^{N} I_{iz} + \Omega \vec{S} \cdot \sum_{i=1}^{N} \vec{I}_i, \tag{5.1}$$

where $\vec{S}$ and $\vec{I}_i$ are the spin operators of the impurity and the i-th condensate boson respectively. Ω is the impurity-boson interaction strength and c_2 is the boson-boson interaction strength. The impurity-boson interaction includes both spin-exchange and density-density interactions. B_e and B_s describe the magnetic fields seen by the impurity and bosons respectively. In the following texts, we study the reduced density matrix ρ of the impurity interacting with different initial states of the environment, which are polar states, ferromagnetic states, and spin singlet states. Before proceeding, we notice that the boson-boson interaction operator $c_2(\sum \vec{I}_i)^2$ commutes with all other terms in the Hamiltonian, therefore the boson-boson interaction will not affect the results and we will neglect it in the following discussions.

5.2 Decoherence of the Spin Impurity

5.2.1 Spin singlet and ferromagnetic state BEC

A condensate of a spin singlet can be described by $|I = 0, m_I = 0\rangle$. It is the ground state of a spin-1 BEC in the zero magnetic field [148, 171]. Since the total spin and the spin z-component are both zero, the interaction term in the Hamiltonian Eq. (5.1) can not exchange spin angular momenta among the environment and the impurity. Thus the impurity keeps in a pure state.

On the other hand, in a spin-1 condensate of ferromagnetic state, the state of a single boson is [14]

$$e^{i\tau} \left(e^{-i\varphi} \cos^2 \frac{\theta}{2} |m = 1\rangle + \sqrt{2} \cos \frac{\theta}{2} \sin \frac{\theta}{2} |m = 0\rangle + e^{i\varphi} \sin^2 \frac{\theta}{2} |m = -1\rangle \right). \tag{5.2}$$

We choose the quantization axis such that every boson is in the state $|m = 1\rangle$ and the condensate can be described by a Fock state $|N_1 = N, N_0 = 0, N_{-1} = 0\rangle$. For any initial

state of the impurity, $\alpha|\uparrow\rangle + \beta|\downarrow\rangle$, only $\beta|\downarrow\rangle$ is able to interact with the condensate through spin exchanges. Thus the total system is equivalent to a two-level system and the reduced density matrix of the impurity can be calculated analytically,

$$\rho_{\uparrow\uparrow} = |\alpha|^2 + 2|\beta|^2 \frac{2N}{(2N-\gamma-1)^2+8N}\left(1-\cos\frac{\sqrt{(2N-1-\gamma)^2+8N}\Omega t}{2}\right) \tag{5.3}$$

$$\begin{aligned}\rho_{\uparrow\downarrow} = \alpha\beta^* e^{-it\left(\frac{B_e+B_s}{2}+\frac{\Omega}{4}(1+2N)\right)}\Bigg(&\cos\frac{\sqrt{(2N-1-\gamma)^2+8N}\Omega t}{4} \\ &- i\,\frac{2N-1-\gamma}{\sqrt{(2N-1-\gamma)^2+8N}}\sin\frac{\sqrt{(2N-1-\gamma)^2+8N}\Omega t}{4}\Bigg)\end{aligned} \tag{5.4}$$

$$\gamma = \frac{2(B_e-B_s)}{\Omega} \tag{5.5}$$

Since the dynamics only involve two energy levels, the reduced density matrix simply shows sinusoidal oscillations. External magnetic fields only change the frequency and the amplitude. Thus in this case decoherence does not happen either.

5.2.2 Polar state BEC

A polar state of a spin-1 boson has the following form [14]

$$e^{i\tau}\left(-\frac{1}{\sqrt{2}}e^{-i\varphi}\sin\theta\,|m=1\rangle + \cos\theta\,|m=0\rangle + \frac{1}{\sqrt{2}}e^{i\varphi}\sin\theta\,|m=-1\rangle\right). \tag{5.6}$$

We first consider the case without magnetic fields, $B_e = B_s = 0$. Again we can choose an appropriate quantization axis such that every boson is in the state $|m=0\rangle$ and the condensate can be simply described by a Fock state $|N_1=0, N_0=N, N_{-1}=0\rangle$. The total initial state is

$$|\psi_0\rangle = (\alpha|\uparrow\rangle + \beta|\downarrow\rangle)\otimes|0,N,0\rangle\,. \tag{5.7}$$

Fig. 5.1(a) illustrates the numerical results of the spin's reduced density matrix ρ as a function of time. Both the diagonal and off-diagonal terms quickly decrease to constant values. The two diagonal terms $\rho_{\uparrow\uparrow}$ and $\rho_{\downarrow\downarrow}$ are stabilized to 1/2 while the the off-diagonal term $\rho_{\uparrow\downarrow}$ is stabilized to one half of its initial value, indicating that there is still residual coherence between $|\uparrow\rangle$ and $|\downarrow\rangle$ when the impurity reaches equilibrium. After a relatively long time scale, both the diagonal and off-diagonal elements oscillate for a short time. And then this pattern repeats.

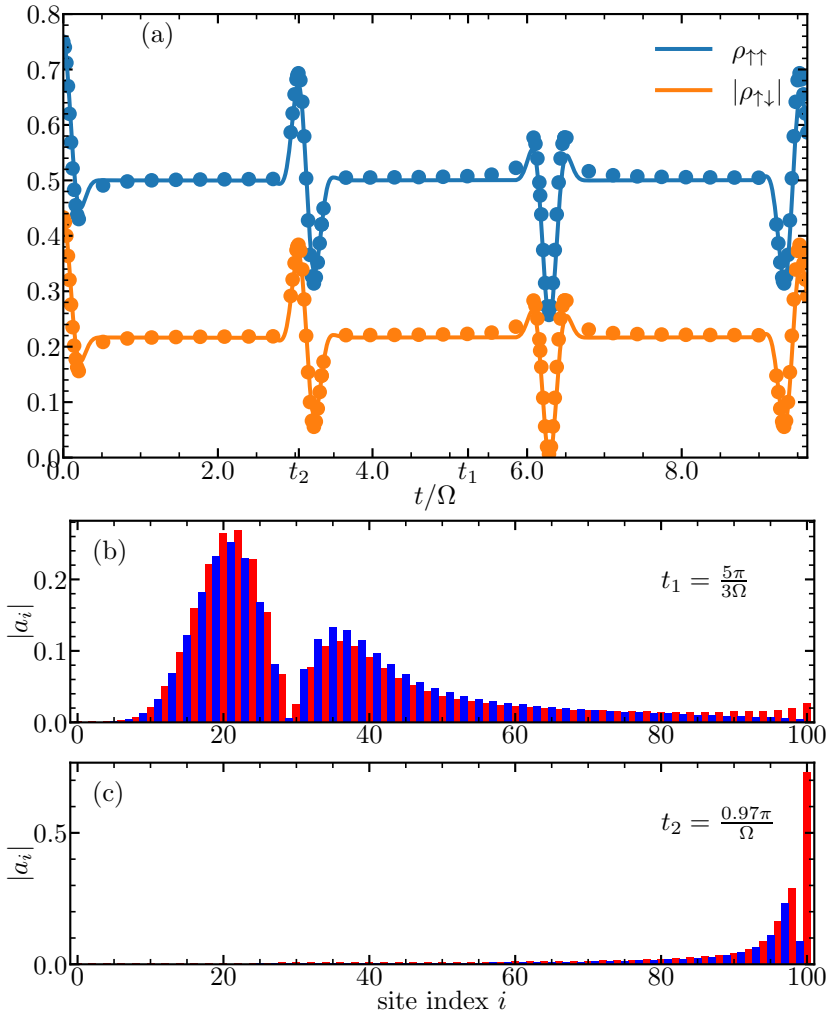

Figure 5.1: Numerical simulation results of a spin impurity embedded in a polar state BEC. The initial state of the impurity is $\frac{\sqrt{3}}{2}|\uparrow\rangle+\frac{1}{2}|\downarrow\rangle$. $B_s = B_e = 0$. The BEC has $N = 100$ bosons. (a) The impurity's reduced density matrix elements. Dots are numerical results from exact diagonalization. Curves are analytical solutions Eqs. (5.24) (5.25). $\chi = 0.706$ is used. (b-c) The wave function $|a_i|$ on the up-chain at $t_1 = 5\pi/3\Omega$ and $t_2 = 0.97\pi/\Omega$. Red and blue bars correspond to red diamonds and blue squares in Fig. (5.2) respectively.

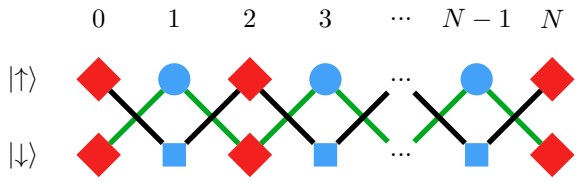

Figure 5.2: When the initial environment is a polar state, the total Hilbert space can be viewed as two twisted but decoupled chains: up-chain (black) and down-chain (green). Red diamonds at even site $2k$ represent Fock states $|k, N-2k, 2k\rangle$ of the environment. At odd site $2k+1$, blue circles represent $|k, N-(2k+1), k+1\rangle$ and blue squares represent $|k+1, N-(2k+1), k\rangle$. Black and green stripes represent the spin exchange interactions.

To understand the numerical results, we first inspect the evolution in the Fock space. Without loss of generality, we consider even number of bosons in the BEC. It is easy to see that for the term $\alpha\,|\uparrow\rangle \otimes |0, N, 0\rangle$ in the initial state, as time goes on, the wave function moves on a one-dimensional chain as illustrated in Fig. 5.2,

$$|\uparrow\rangle\,|0, N, 0\rangle\,, |\downarrow\rangle\,|1, N-1, 0\rangle\,, |\uparrow\rangle\,|1, N-2, 1\rangle\,, ..., |\uparrow\rangle\left|\frac{N}{2}, 0, \frac{N}{2}\right\rangle \tag{5.8}$$

We call it up-chain. Similarly, the term $|\downarrow\rangle \otimes |0, N, 0\rangle$ moves on the down-chain,

$$|\downarrow\rangle\,|0, N, 0\rangle\,, |\uparrow\rangle\,|0, N-1, 1\rangle\,, |\downarrow\rangle\,|1, N-2, 1\rangle\,, ..., |\downarrow\rangle\left|\frac{N}{2}, 0, \frac{N}{2}\right\rangle \tag{5.9}$$

These two chains do not overlap. Further we notice that once we reverse the direction of the quantization axis, one chain turns into the other one. Such an inversion symmetry guarantees that these two chains have the same energy spectrum. At any time, the total wave function is expanded as

$$\begin{aligned}|\Psi(t)\rangle = &\sum_{i=0,\text{even}}^{N} a_i(t)\,|\uparrow\rangle\left|\frac{i}{2}, N-i, \frac{i}{2}\right\rangle + \sum_{i=1,\text{odd}}^{N} a_i(t)\,|\downarrow\rangle\left|\frac{i+1}{2}, N-i, \frac{i-1}{2}\right\rangle \\ &+ \sum_{i=0,\text{even}}^{N} b_i(t)\,|\downarrow\rangle\left|\frac{i}{2}, N-i, \frac{i}{2}\right\rangle + \sum_{i=1,\text{odd}}^{N} b_i(t)\,|\uparrow\rangle\left|\frac{i-1}{2}, N-i, \frac{i+1}{2}\right\rangle,\end{aligned} \tag{5.10}$$

where a_i and b_i represent the probability amplitudes on the two chains respectively. Since the initial state Eq. (5.7) only occupies the leftmost site of the two chains, as a result of the inversion symmetry, at any time, the probability amplitudes on the two chains are only

differed by an overall factor,

$$\forall i,\ \frac{a_i(t)}{b_i(t)} = \frac{\alpha}{\beta}. \tag{5.11}$$

Initially $\rho_{\uparrow\uparrow} = |\alpha|^2$, $\rho_{\downarrow\downarrow} = |\beta|^2$, $\rho_{\uparrow\downarrow} = \alpha\beta^*$. Later the wave function evolves and extends over many vertices. Focusing on one chain, if the number of vertices is large enough and the wave function is a slowly varying function of the site index i, the summation of the probabilities on even-i sites (red vertices in Fig. 5.2) should be approximately equal to the sum on odd-i sites (blue vertices). In other words, if we plot out the probability distribution $|a_i|^2$ and $|b_i|^2$, as displayed in Fig. 5.1(b), the area of red bars should be equal to blue bars, given the width of a single bar is much smaller than the width of the wave function. Such an intuition allows us to calculate $\rho_{\uparrow\uparrow}$ and $\rho_{\downarrow\downarrow}$,

$$\rho_{\uparrow\uparrow} = \sum_{i=0,\text{even}}^{N} |a_i|^2 + \sum_{i=1,\text{odd}}^{N} |b_i|^2 \approx \frac{1}{2}\left(\sum_{i=0}^{N} |a_i|^2 + \sum_{i=0}^{N} |b_i|^2\right) = \frac{1}{2}, \tag{5.12}$$

$$\rho_{\downarrow\downarrow} = \sum_{i=1,\text{odd}}^{N} |a_i|^2 + \sum_{i=0,\text{even}}^{N} |b_i|^2 \approx \frac{1}{2}\left(\sum_{i=0}^{N} |a_i|^2 + \sum_{i=0}^{N} |b_i|^2\right) = \frac{1}{2}. \tag{5.13}$$

Similarly, to calculate the off-diagonal term $\rho_{\uparrow\downarrow}$, we notice in the total wave function, only the terms where the impurity is coupled with environment Fock states $|m, N-2m, m\rangle$ have non-zero contributions to $\rho_{\uparrow\downarrow}$. To put it another way, we only need to take into consideration the red vertices in Fig. 5.2,

$$\rho_{\uparrow\downarrow} = \sum_{i=0,even}^{N} a_i b_i^* = \sum_{i=0,even}^{N} \frac{\alpha b_i}{\beta} b_i^* \approx \frac{\alpha}{\beta}\frac{1}{2}\sum_{i=0}^{N} b_i b_i^* = \frac{\alpha}{2\beta}|\beta|^2 = \frac{1}{2}\alpha\beta^*. \tag{5.14}$$

When the wave packet spreads to the end of a chain, which is the case shown in Fig. 5.1(c), it is no longer a spatially slowly-varying function. This corresponds to the short oscillations of the reduced density matrix elements in Fig. 5.1(a).

With the simple picture above, now we calculate the reduced density matrix analytically. Consider the Hilbert subspace associated with up-chain Eq. (5.8). The initial polar state is a superposition of different eigenstates $|I, 0\rangle$ of the total spin operator $\vec{I}^2$ and its z-component I_z, where the quantum number I can take even values $0, 2, 4, ..., N$. The spin exchange interaction couples $|\uparrow\rangle \otimes |I, 0\rangle$ to $|\downarrow\rangle \otimes |I, 1\rangle$. The Hamiltonian is then 2×2 block-diagonalized in this representation, except $|\uparrow\rangle \otimes |0, 0\rangle$. We can work out all the eigenstates and eigenvalues

in this subspace:

$$E_{u1,I} = \frac{I}{2}\Omega, \qquad |E_{u1,I}\rangle = \sqrt{\frac{1+I}{1+2I}}\,|\uparrow\rangle\,|I,0\rangle + \sqrt{\frac{I}{1+2I}}\,|\downarrow\rangle\,|I,1\rangle\,, \tag{5.15}$$

$$E_{u2,I} = -\frac{1+I}{2}\Omega, \qquad |E_{u2,I}\rangle = \sqrt{\frac{I}{1+2I}}\,|\uparrow\rangle\,|I,0\rangle - \sqrt{\frac{1+I}{1+2I}}\,|\downarrow\rangle\,|I,1\rangle\,. \tag{5.16}$$

The subscript u denotes that they are associated with the up-chain. Similarly for the down-chain,

$$E_{d1,I} = \frac{I}{2}\Omega, \qquad |E_{d1,I}\rangle = \sqrt{\frac{1+I}{1+2I}}\,|\downarrow\rangle\,|I,0\rangle + \sqrt{\frac{I}{1+2I}}\,|\uparrow\rangle\,|I,-1\rangle\,, \tag{5.17}$$

$$E_{d2,I} = -\frac{1+I}{2}\Omega, \qquad |E_{d2,I}\rangle = \sqrt{\frac{I}{1+2I}}\,|\downarrow\rangle\,|I,0\rangle - \sqrt{\frac{1+I}{1+2I}}\,|\uparrow\rangle\,|I,-1\rangle\,. \tag{5.18}$$

Thus we are able to write down the the wavefunction at any time,

$$\begin{aligned} |\Psi(t)\rangle = \sum_{I=0}^{N} \alpha \left(c_I e^{-itE_{u1,I}}\,|E_{u1,I}\rangle + d_I e^{-itE_{u2,I}}\,|E_{u2,I}\rangle\right) \\ +\beta \left(c_I e^{-itE_{d1,I}}\,|E_{d1,I}\rangle + d_I e^{-itE_{d2,I}}\,|E_{d2,I}\rangle\right), \end{aligned} \tag{5.19}$$

where $c_I = \sqrt{\frac{1+I}{1+2I}}p_I$, $d_I = \sqrt{\frac{I}{1+2I}}p_I$, $p_I = \langle I,0|0,N,0\rangle$. The elements of the reduced density matrix are

$$\begin{aligned} \rho_{\uparrow\downarrow} = \alpha\beta^* \sum_{I=0}^{N} |p_I|^2 \left(\frac{1+I}{2I+1}e^{-itE_{u1,I}} + \frac{I}{2I+1}e^{-itE_{u2,I}}\right) \\ \cdot \left(\frac{1+I}{2I+1}e^{itE_{d1,I}} + \frac{I}{2I+1}e^{itE_{d2,I}}\right), \end{aligned} \tag{5.20}$$

$$\begin{aligned} \rho_{\uparrow\uparrow} = \sum_{I=0}^{N} |p_I|^2 \left(|\alpha|^2 \left|\frac{1+I}{2I+1}e^{-itE_{u1,I}} + \frac{I}{2I+1}e^{-itE_{u2,I}}\right|^2 \right. \\ \left. +|\beta|^2 \left|e^{-itE_{d1,I}} - e^{-itE_{d2,I}}\right|^2 \frac{I(I+1)}{(2I+1)^2}\right). \end{aligned} \tag{5.21}$$

We now exploit the following approximation [172],

$$\frac{1+I}{2I+1} \approx \frac{I}{2I+1} \approx \frac{1}{2}, \tag{5.22}$$

$$\langle I,0|0,N,0\rangle \approx \sqrt[4]{\frac{4}{N\pi}}e^{-\frac{2}{N}(\frac{I}{2}-\chi\sqrt{\frac{N}{2}})^2}, I \in 2\mathbb{Z}. \tag{5.23}$$

where χ is a fitting parameter,

$$\rho_{\uparrow\downarrow} \approx \frac{\alpha\beta^*}{2} + \frac{\alpha\beta^*}{2}\cos\left(\left(\frac{1}{2}+\chi\sqrt{2N}\right)\Omega t\right)\sum_{n=0}^{\infty} e^{-\frac{N\Omega^2}{4}(t-\frac{n\pi}{\Omega})^2}, \tag{5.24}$$

$$\rho_{\uparrow\uparrow} \approx \frac{1}{2} + \frac{|\alpha|^2-|\beta|^2}{2}\cos\left(\left(\frac{1}{2}+\chi\sqrt{2N}\right)\Omega t\right)\sum_{n=0}^{\infty} e^{-\frac{N\Omega^2}{4}(t-\frac{n\pi}{\Omega})^2}. \tag{5.25}$$

Eq. (5.24) tells that $\rho_{\uparrow\downarrow}$ is a series of gaussian peeks with separation $T_r = \frac{\pi}{\Omega}$ and width $\tau = \frac{2}{\Omega\sqrt{N}}$, plus a constant term $\alpha\beta^*/2$, corresponding to the residual coherence. The actual shapes of the gaussian peaks are also determined by the cosine factor, therefore in Fig. 5.1(a) some peaks go up while some go down. Similar conclusions apply to the diagonal terms.

In a time window of the scale T_r, the reduced density matrix of the impurity keeps constant,

$$\rho = \begin{bmatrix} \frac{1}{2} & \frac{1}{2}\alpha\beta^* \\ \frac{1}{2}\alpha^*\beta & \frac{1}{2} \end{bmatrix}. \tag{5.26}$$

The impurity thus reaches a thermalized equilibrium state. We can work out the eigenvalues of ρ, $\lambda = \frac{1}{2}(1 \pm |\alpha\beta|)$. If we view the impurity as a two level system with energy splitting ΔE, we can define a temperature T for the impurity,

$$\frac{k_B T}{\Delta E} = \frac{1+|\alpha\beta|}{1-|\alpha\beta|}. \tag{5.27}$$

The temperature T is only a function of the initial coherence of the impurity $|\alpha\beta|$. A larger initial coherence leads to a higher equilibrium temperature.

5.2.3 Polar state BEC with external fields

Now we consider an external magnetic field along the z axis such that B_s and B_e are finite. The numerical results in Fig. 5.3(a) indicate that, for a weak magnetic field $\gamma = 2(B_e - B_s)/\Omega \ll 1$, while the diagonal terms do not change too much, the original constant term of $\rho_{\uparrow\downarrow}$ gradually decreases. From Eq. (5.20), we know that the constant term $\alpha\beta^*/2$ in Eq. (5.24) comes from the fact that the energy spectra of the two subspaces are identical. For instance, $\alpha c_I e^{-itE_{u1,I}}|E_{u1,I}\rangle$ and $\beta c_I e^{-itE_{d1,I}}|E_{d1,I}\rangle$ contribute $\alpha\beta^*|c_I|^2 e^{it(E_{u1,I}-E_{d1,I})}\frac{1+I}{1+2I}$ to $\rho_{\uparrow\downarrow}$. Since without the magnetic filed, $E_{u1,I} = E_{d1,I}$, this contribution is a constant. In other words, the inversion symmetry is crucial for the finite residual coherence when the impurity reaches equilibrium. However, an external filed breaks the inversion symmetry. As

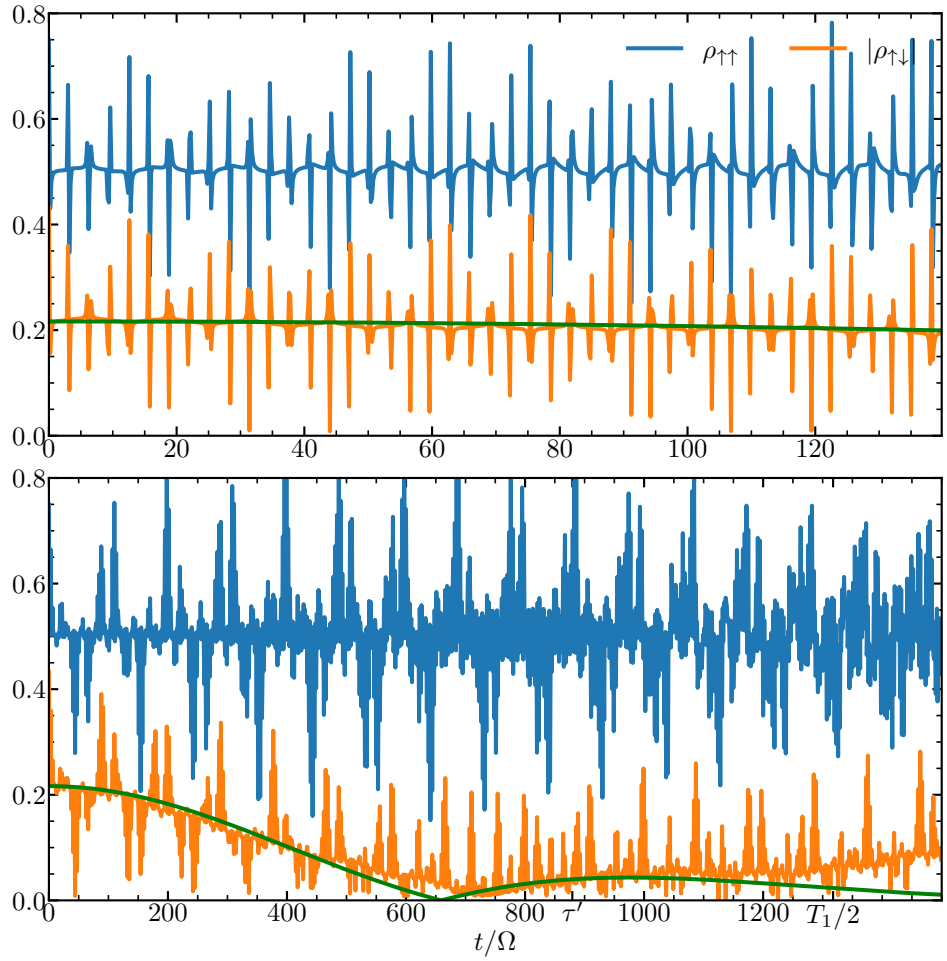

Figure 5.3: With the presence of magnetic fields along the quantization axis, the constant term in $\rho_{\uparrow\downarrow}$ gradually decreases in a time scale $\propto \sqrt{N}/\gamma$. The two panels exhibit results in short and long time scales respectively. Here the numerical parameters are the same as Fig. 5.1 except $\gamma = 0.1$. The green curve is the first term in Eq. (5.32). The lower panel indicates that the analytical expression is not valid for very long time scales $\propto T_1$ because of the approximations we have used.

a result, the two chains are no longer mirrors of each other. As shown in Appendix 5.4, the magnetic filed only adds diagonal terms to the total Hamiltonian, therefore the two chains are still decoupled, but the energy spectra are changed. A special case is $B_e = B_s$, where the magnetic filed simply adds $B_s/2$ to every vertex of the up-chain and $-B_s/2$ to every vertex of the down-chain. The two subspaces are essentially still the same, only a phase factor is added to the constant term of $\rho_{\uparrow\downarrow}$. For a small γ, as an approximation, we consider the eigenstates to the zero-th order and eigenenergies to the first order of γ,

$$E_{u1,I} \approx \frac{\Omega}{2}(I + \frac{1}{2}(1 - \frac{1}{1+2I})\gamma) + \frac{B_s}{2}, \tag{5.28}$$

$$E_{u2,I} \approx \frac{\Omega}{2}(-I - 1 + \frac{1}{2}(1 + \frac{1}{1+2I})\gamma) + \frac{B_s}{2}, \tag{5.29}$$

$$E_{d1,I} \approx \frac{\Omega}{2}(I - \frac{1}{2}(1 - \frac{1}{1+2I})\gamma) - \frac{B_s}{2}, \tag{5.30}$$

$$E_{d2,I} \approx \frac{\Omega}{2}(-I - 1 - \frac{1}{2}(1 + \frac{1}{1+2I})\gamma) - \frac{B_s}{2}, \tag{5.31}$$

which gives

$$\begin{aligned}\rho_{\uparrow\downarrow} \approx \frac{\alpha\beta^*}{2} e^{-iB_e t} \cos\frac{\gamma\Omega t}{2(1+2\chi\sqrt{2N})} \sum_{n=0}^{\infty} e^{-\frac{N\gamma^2\Omega^2}{4(1+2\chi\sqrt{2N})^4}\left(t - \frac{n\pi(1+2\chi\sqrt{2N})^2}{\gamma\Omega}\right)^2} \\ + \frac{\alpha\beta^*}{2} e^{-iB_e t} \cos\frac{(1+2\chi\sqrt{2N})\Omega t}{2} \sum_{n=0}^{\infty} e^{-\frac{N\Omega^2}{4}(t - \frac{n\pi}{\Omega})^2}.\end{aligned} \tag{5.32}$$

Comparing Eq. (5.24) and Eq. (5.32), we see that the original constant term $\alpha\beta^*/2$ becomes a series of gaussian peaks. There are three time scales, the period T_1 of the cosine function, the width τ' of the gaussian, and the distance T_2 between two neighboring peaks,

$$T_1 = \frac{4\pi(1+2\chi\sqrt{2N})}{\gamma\Omega},\ \tau' = \frac{2(1+2\chi\sqrt{2N})^2}{\sqrt{N}\gamma\Omega},\ T_2 = \frac{\pi(1+2\chi\sqrt{2N})^2}{\gamma\Omega} \tag{5.33}$$

Fig. 5.3 demonstrates the numerical results compared with the first term of Eq. (5.32). Although in the time scale larger than $T_1/2$, a large deviation manifests because of the approximations we have used, the analytical expression well captures the numerical results within τ'. In the thermodynamic limit $N \to \infty$, both T_1 and τ' are proportional to $\sqrt{N}/\gamma$ and T_2 is proportional to N/γ. This means once γ is fixed, the life time of the residual coherence is longer if there are more bosons in the environment, which is contradictory to our experience that the coherence time of a system becomes shorter if there are more particles interacting with it in the environment [52]. This result can be understood from the dependence of the

energy splittings on the quantum number I. Consider the term $\sum |p_I|^2 \frac{1+I}{2I+1} e^{-it(E_{u1,I}-E_{d1,I})}$ in Eq. (5.20). The time dependence of $\rho_{\uparrow\downarrow}$ comes from the energy splitting,

$$\Delta E_{1I} = E_{u1,I} - E_{d1,I} \approx \frac{\Omega}{2}\gamma\left(1 - \frac{1}{1+2I}\right) + B_s. \tag{5.34}$$

If ΔE_{1I} were independent of I, the time dependence is only in an overall factor and the constant term will not decrease. On the other hand, ΔE_{1I} is a smoother function in the region of larger I's. Moreover, Eq. (5.23) tells that, p_I is a gaussian and as N increases, the center of the gaussian also moves to the region of larger I's. Combining these observations together, we can conclude that as the number of bosons in the environment increases, the effect brought by a fixed γ is smaller and therefore, the residual coherence lives for a longer time scale.

The diagonal terms of the impurity's reduced density matrix can also be computed,

$$\begin{aligned}\rho_{\uparrow\uparrow} \approx \frac{1}{2} + \frac{|\alpha|^2}{2}\cos\frac{(1+2\chi\sqrt{2N})\Omega_1 t}{2}\sum_{n=0}^{\infty} e^{-\frac{N\Omega_2^2}{4}(t-\frac{n\pi}{\Omega_2})^2} \\ -\frac{|\beta|^2}{2}\cos\frac{(1+2\chi\sqrt{2N})\Omega_2 t}{2}\sum_{n=0}^{\infty} e^{-\frac{N\Omega_1^2}{4}(t-\frac{n\pi}{\Omega_1})^2},\end{aligned} \tag{5.35}$$

$$\Omega_1 = \Omega\left(1 - \frac{\gamma}{(1+2\chi\sqrt{2N})^2}\right),\ \Omega_2 = \Omega\left(1 + \frac{\gamma}{(1+2\chi\sqrt{2N})^2}\right). \tag{5.36}$$

Comparing Eq. (5.35) and Eq. (5.25), $\rho_{\uparrow\uparrow}$ remains 1/2 when the impurity is thermalized, which is verified by the numerical result in Fig. 5.3. Our previous arguments still apply since we only require that the wave function on the two chains is a slowly-varying function of the site index, which still holds with the presence of magnetic fields.

5.3 Summary

Table 5.1: The dependence of the spin impurity's reduced density matrix on the initial state of the environment BEC.

spin singlet	pure state
ferromagnetic state	sinusoidal oscillations, frequency and amplitude changed by γ
polar state	decoherence occurs. coherence time $\propto \frac{1}{\Omega\sqrt{N}}$, revival time $\propto \frac{1}{\Omega}$, lifetime of residual coherence $\propto \frac{\sqrt{N}}{\gamma}$.

In conclusion, we have studied the dynamics of a single spin-1/2 impurity interacting with

a spin-1 BEC of different phases. The coherence of the impurity shows different behaviors depending on the initial state of the BEC, as summarized by Table 5.1. Analytical and numerical results are presented. These conclusions can be used by experimentalists to detect the state of a spinor BEC.

5.4 Appendix

The eigenenergies and eigenstates of the Hamiltonian with the presence of a magnetic field along the z direction,

$$E_{u1,I} = \frac{\Omega}{4}(P + \sqrt{P^2 + R}) + \frac{B_s}{2}, \tag{5.37}$$

$$|E_{u1,I}\rangle = \sqrt{\frac{\sqrt{P^2+R} - P}{2\sqrt{P^2+R}}}\,|\uparrow\rangle\,|I,0\rangle + \sqrt{\frac{\sqrt{P^2+R} + P}{2\sqrt{P^2+R}}}\,|\downarrow\rangle\,|I,1\rangle\,, \tag{5.38}$$

$$E_{u2,I} = \frac{\Omega}{4}(P - \sqrt{P^2 + R}) + \frac{B_s}{2}, \tag{5.39}$$

$$|E_{u1,I}\rangle = \sqrt{\frac{\sqrt{P^2+R} + P}{2\sqrt{P^2+R}}}\,|\uparrow\rangle\,|I,0\rangle - \sqrt{\frac{\sqrt{P^2+R} - P}{2\sqrt{P^2+R}}}\,|\downarrow\rangle\,|I,1\rangle\,, \tag{5.40}$$

$$E_{d1,I} = \frac{\Omega}{4}(Q + \sqrt{Q^2 + R}) - \frac{B_s}{2}, \tag{5.41}$$

$$|E_{d1,I}\rangle = \sqrt{\frac{\sqrt{Q^2+R} - Q}{2\sqrt{Q^2+R}}}\,|\uparrow\rangle\,|I,0\rangle + \sqrt{\frac{\sqrt{Q^2+R} + Q}{2\sqrt{Q^2+R}}}\,|\downarrow\rangle\,|I,-1\rangle\,, \tag{5.42}$$

$$E_{d2,I} = \frac{\Omega}{4}(Q - \sqrt{Q^2 + R}) - \frac{B_s}{2}, \tag{5.43}$$

$$|E_{d1,I}\rangle = \sqrt{\frac{\sqrt{Q^2+R} + Q}{2\sqrt{Q^2+R}}}\,|\uparrow\rangle\,|I,0\rangle - \sqrt{\frac{\sqrt{Q^2+R} - Q}{2\sqrt{Q^2+R}}}\,|\downarrow\rangle\,|I,-1\rangle\,, \tag{5.44}$$

$$P = \gamma - 1,\ Q = -\gamma - 1,\ R = 4I(I+1),\ \gamma = \frac{2(B_e - B_s)}{\Omega}. \tag{5.45}$$

6. SUMMARY

This dissertation focuses on the the dynamical evolution of several models consisting of ultracold atoms. We have used theoretical tools such as Loschmidt echo, SU(1,1) group, and reduced density matrices. Our theoretical calculations revealed the hidden properties of the evolution and discovered emergent highly entangled states.

In Chapter 2, we studied a generic two-mode bosonic model with weak on-site interactions. By extending the real time to the complex domain and working out the zeros of the Loschmidt echo, we found that near a time scale inversely proportional to the interaction strength, those zeros with finite real parts gradually approach the real time axes as the particle number grows, which leads to dynamical quantum phase transitions. We also discovered that right located at these transition points, the system evolves into one type of highly entangled state, pair condensate. Between two pair condensates, two different types of Schrödinger's cat states exist. The correspondence of the transition points and the highly entangled states shows that DQPT is a powerful tool to study the non-equilibrium quantum dynamics.

In Chapter 3, we proposed a new design of discrete time crystals. Different from models stabilized by many-body localization in the literature, here in a clean system composed of interacting two-component bosonic particles, we utilized all-to-all interactions to deliver a perfect revival of the initial state. These revivals are stable against any imperfections in the driving filed, such as the spatial randomness, given that the interaction J and driving period T satisfy $JT = \pi$. We further demonstrated that this super-sensitivity on JT can be used in precision measurement (for example, gauging frequencies of different pulses and tunning the scattering length of interacting particles) to the precision of $1/N^{3/2}$, which beats the Heisenberg limit. On the other hand, if the interaction J is tuned to $JT = \pi/2$, we can create a DTC composed of highly entangled Schrödinger's cat states.

In Chapter 4, we studied the dynamical evolution of weakly interacting bose gases. By unfolding the SU(1,1) symmetry, we established a one-to-one correspondence between a BEC and a Poincaré disk. This geometric framework correlates fundamental quantities such as time, length, and temperature all together. More importantly, it provides recipes for experimentalists to control the dynamical evolution, such as accelerating and slowing down the particle excitation, or reversing the dynamics. Backward evolution is a critical step in measuring OTOC, our results thus provides a concrete example of reversing the dynamics

effectively.

In Chapter 5, we calculated the reduced density matrix of a spin-1/2 impurity inside a spinor BEC, which is viewed as a subsystem interacting with the environment. We discussed different environment states and particularly focused on polar states. The coherence of the impurity decreases. However a residual coherence is protected by the inversion symmetry when magnetic fields is absent. We also analyzed the effects of finite magnetic fields analytically. An counterintuitive dependence of the residual coherence on the environment particle number was addressed. Because the coherence of the impurity responds differently to difference phase of the environment spinor BEC, thus experimentalists can use it to detect the environment's state.

While this thesis only explored a small corner of the fascinating world of quantum evolution, it already demonstrated that cold atoms are suitable candidates for construct and realize theoretical models. It is expected that many topics like entanglement growth, quantum information scrambling, non-Hermitian physics, and physics in non-Euclidean spaces, can get further investigated within this platform.

BIBLIOGRAPHY

[1] C. Chin, R. Grimm, P. Julienne, and E. Tiesinga, "Feshbach resonances in ultracold gases", *Rev. Mod. Phys.* **82**, 1225–1286 (2010).

[2] M. Li and J. Arlt, "Trapping multiple particles in single optical tweezers", *Opt. Commun.* **281**, 135–140 (2008).

[3] A. M. Kaufman, B. J. Lester, and C. A. Regal, "Cooling a single atom in an optical tweezer to its quantum ground state", *Phys. Rev. X* **2**, 041014 (2012).

[4] A. M. Kaufman, B. J. Lester, C. M. Reynolds, M. L. Wall, M. Foss-Feig, K. R. A. Hazzard, A. M. Rey, and C. A. Regal, "Two-particle quantum interference in tunnel-coupled optical tweezers", *Science* **345**, 306–309 (2014).

[5] W. S. Bakr, A. Peng, M. E. Tai, R. Ma, J. Simon, J. I. Gillen, S. Folling, L. Pollet, and M. Greiner, "Probing the superfluid-to-Mott insulator transition at the single-atom level", *Science* **329**, 547–550 (2010).

[6] J. F. Sherson, C. Weitenberg, M. Endres, M. Cheneau, I. Bloch, and S. Kuhr, "Single-atom-resolved fluorescence imaging of an atomic Mott insulator", *Nature* **467**, 68–72 (2010).

[7] O. Penrose and L. Onsager, "Bose-Einstein condensation and liquid Helium", *Phys. Rev.* **104**, 576–584 (1956).

[8] E. J. Mueller, T.-L. Ho, M. Ueda, and G. Baym, "Fragmentation of Bose-Einstein condensates", *Phys. Rev. A* **74**, 033612 (2006).

[9] P. Nozières and D. Saint James, "Particle vs. pair condensation in attractive Bose liquids", *J. Phys. France* **43**, 1133–1148 (1982).

[10] U. R. Fischer and B. Xiong, "Robustness of fragmented condensate many-body states for continuous distribution amplitudes in Fock space", *Phys. Rev. A* **88**, 053602 (2013).

[11] K.-J. Chen, H. K. Lau, H. M. Chan, D. Wang, and Q. Zhou, "Unfolding multi-particle quantum correlations hidden in decoherence", *arXiv:1711.04105 [cond-mat.quant-gas]* (2017).

[12] T.-L. Ho and V. B. Shenoy, "Local spin-gauge symmetry of the Bose-Einstein condensates in atomic gases", *Phys. Rev. Lett.* **77**, 2595–2599 (1996).

[13] M. Ueda, "Spinor bose-einstein condensate", in *Fundamentals and new frontiers of bose-einstein condensation* (World Scientific, Singapore, 2010), pp. 145–170.

[14] T.-L. Ho, "Spinor Bose condensates in optical traps", *Phys. Rev. Lett.* **81**, 742–745 (1998).

[15] C. W. Helstrom, "Quantum detection and estimation theory", *J. Stat. Phys.* **1**, 231–252 (1969).

[16] C. N. Yang and T. D. Lee, "Statistical theory of equations of state and phase transitions. I. theory of condensation", *Phys. Rev.* **87**, 404–409 (1952).

[17] B.-B. Wei and R.-B. Liu, "Lee-Yang zeros and critical times in decoherence of a probe spin coupled to a bath", *Phys. Rev. Lett.* **109**, 185701 (2012).

[18] X. Peng, H. Zhou, B.-B. Wei, J. Cui, J. Du, and R.-B. Liu, "Experimental observation of Lee-Yang zeros", *Phys. Rev. Lett.* **114**, 010601 (2015).

[19] A. A. Zvyagin, "Dynamical quantum phase transitions (review article)", *Low Temp. Phys.* **42**, 971–994 (2016).

[20] M. Heyl, "Dynamical quantum phase transitions: a review", *Rep. Prog. Phys.* **81**, 054001 (2018).

[21] M. Heyl, A. Polkovnikov, and S. Kehrein, "Dynamical quantum phase transitions in the transverse-field Ising model", *Phys. Rev. Lett.* **110**, 135704 (2013).

[22] A. Shapere and F. Wilczek, "Classical time crystals", *Phys. Rev. Lett.* **109**, 160402 (2012).

[23] F. Wilczek, "Quantum time crystals", *Phys. Rev. Lett.* **109**, 160401 (2012).

[24] P. Bruno, "Comment on "Quantum time crystals"", *Phys. Rev. Lett.* **110**, 118901 (2013).

[25] F. Wilczek, "Wilczek reply:" *Phys. Rev. Lett.* **110**, 118902 (2013).

[26] T. Li, Z.-X. Gong, Z.-Q. Yin, H. T. Quan, X. Yin, P. Zhang, L.-M. Duan, and X. Zhang, "Space-time crystals of trapped ions", *Phys. Rev. Lett.* **109**, 163001 (2012).

[27] P. Bruno, "Comment on "Space-time crystals of trapped ions"", *Phys. Rev. Lett.* **111**, 029301 (2013).

[28] P. Bruno, "Impossibility of spontaneously rotating time crystals: a no-go theorem", *Phys. Rev. Lett.* **111**, 070402 (2013).

[29] H. Watanabe and M. Oshikawa, "Absence of quantum time crystals", *Phys. Rev. Lett.* **114**, 251603 (2015).

[30] K. Sacha, "Modeling spontaneous breaking of time-translation symmetry", *Phys. Rev. A* **91**, 033617 (2015).

[31] V. Khemani, A. Lazarides, R. Moessner, and S. L. Sondhi, "Phase structure of driven quantum systems", *Phys. Rev. Lett.* **116**, 250401 (2016).

[32] D. V. Else, B. Bauer, and C. Nayak, "Floquet time crystals", *Phys. Rev. Lett.* **117**, 090402 (2016).

[33] N. Y. Yao, A. C. Potter, I.-D. Potirniche, and A. Vishwanath, "Discrete time crystals: rigidity, criticality, and realizations", *Phys. Rev. Lett.* **118**, 030401 (2017).

[34] S. Choi, J. Choi, R. Landig, G. Kucsko, H. Zhou, J. Isoya, F. Jelezko, S. Onoda, H. Sumiya, V. Khemani, C. von Keyserlingk, N. Y. Yao, E. Demler, and M. D. Lukin, "Observation of discrete time-crystalline order in a disordered dipolar many-body system", *Nature* **543**, 221–225 (2017).

[35] J. Zhang, P. W. Hess, A. Kyprianidis, P. Becker, A. Lee, J. Smith, G. Pagano, I.-D. Potirniche, A. C. Potter, A. Vishwanath, N. Y. Yao, and C. Monroe, "Observation of a discrete time crystal", *Nature* **543**, 217–220 (2017).

[36] D. Abanin, W. D. Roeck, W. W. Ho, and F. Huveneers, "A rigorous theory of many-body prethermalization for periodically driven and closed quantum systems", *Commun. Math. Phys.* **354**, 809–827 (2017).

[37] A. Russomanno, F. Iemini, M. Dalmonte, and R. Fazio, "Floquet time crystal in the Lipkin-Meshkov-Glick model", *Phys. Rev. B* **95**, 214307 (2017).

[38] S. Pal, N. Nishad, T. S. Mahesh, and G. J. Sreejith, "Temporal order in periodically driven spins in star-shaped clusters", *Phys. Rev. Lett.* **120**, 180602 (2018).

[39] J. Rovny, R. L. Blum, and S. E. Barrett, "Observation of discrete-time-crystal signatures in an ordered dipolar many-body system", *Phys. Rev. Lett.* **120**, 180603 (2018).

[40] B. Huang, Y.-H. Wu, and W. V. Liu, "Clean Floquet time crystals: models and realizations in cold atoms", *Phys. Rev. Lett.* **120**, 110603 (2018).

[41] D. V. Else, C. Monroe, C. Nayak, and N. Y. Yao, "Discrete time crystals", *arXiv: 1905.13232 [cond-mat.str-el]* (2019).

[42] S. H. Shenker and D. Stanford, "Black holes and the butterfly effect", *J. High Energy Phys.* **03**, 67 (2014).

[43] J. Maldacena, S. H. Shenker, and D. Stanford, "A bound on chaos", *J. High Energy Phys.* **08**, 106 (2016).

[44] B. Swingle, G. Bentsen, M. Schleier-Smith, and P. Hayden, "Measuring the scrambling of quantum information", *Phys. Rev. A* **94**, 040302 (2016).

[45] K. Hashimoto, K. Murata, and R. Yoshii, "Out-of-time-order correlators in quantum mechanics", *J. High Energy Phys.* **09** (2017).

[46] J. Li, R. Fan, H. Wang, B. Ye, B. Zeng, H. Zhai, X. Peng, and J. Du, "Measuring out-of-time-order correlators on a nuclear magnetic resonance quantum simulator", *Phys. Rev. X* **7**, 031011 (2017).

[47] M. Gärttner, J. G. Bohnet, A. Safavi-Naini, M. L. Wall, J. J. Bollinger, and A. M. Rey, "Measuring out-of-time-order correlations and multiple quantum spectra in a trapped-ion quantum magnet", *Nat. Phys.* **13**, 781–786 (2017).

[48] H. Shen, P. Zhang, R. Fan, and H. Zhai, "Out-of-time-order correlation at a quantum phase transition", *Phys. Rev. B* **96**, 054503 (2017).

[49] B. Swingle, "Unscrambling the physics of out-of-time-order correlators", *Nat. Phys.* **14**, 988–990 (2018).

[50] E. J. Meier, J. Ang'ong'a, F. A. An, and B. Gadway, "Exploring quantum signatures of chaos on a Floquet synthetic lattice", *Phys. Rev. A* **100**, 013623 (2019).

[51] E. L. Hahn, "Spin echoes", *Phys. Rev.* **80**, 580–594 (1950).

[52] M. A. Schlosshauer, *Decoherence: and the quantum-to-classical transition* (Springer Science & Business Media, 2007).

[53] W. H. Zurek, "Environment-induced superselection rules", *Phys. Rev. D* **26**, 1862–1880 (1982).

[54] F. M. Cucchietti, J. P. Paz, and W. H. Zurek, "Decoherence from spin environments", *Phys. Rev. A* **72**, 052113 (2005).

[55] C. Lyu and Q. Zhou, "Dynamical quantum phase transitions in interacting atomic interferometers", *Phys. Rev. A* **101**, 043605 (2020).

[56] J. B. Fixler, G. T. Foster, J. M. McGuirk, and M. A. Kasevich, "Atom interferometer measurement of the Newtonian constant of gravity", *Science* **315**, 74–77 (2007).

[57] S. Fray, C. A. Diez, T. W. Hänsch, and M. Weitz, "Atomic interferometer with amplitude gratings of light and its applications to atom based tests of the equivalence principle", *Phys. Rev. Lett.* **93**, 240404 (2004).

[58] P. Cladé, E. de Mirandes, M. Cadoret, S. Guellati-Khélifa, C. Schwob, F. Nez, L. Julien, and F. Biraben, "Determination of the fine structure constant based on Bloch oscillations of ultracold atoms in a vertical optical lattice", *Phys. Rev. Lett.* **96**, 033001 (2006).

[59] P. W. Graham, J. M. Hogan, M. A. Kasevich, and S. Rajendran, "New method for gravitational wave detection with atomic sensors", *Phys. Rev. Lett.* **110**, 171102 (2013).

[60] S. Dimopoulos, P. W. Graham, J. M. Hogan, M. A. Kasevich, and S. Rajendran, "Atomic gravitational wave interferometric sensor", *Phys. Rev. D* **78**, 122002 (2008).

[61] J. Lawall and M. Prentiss, "Demonstration of a novel atomic beam splitter", *Phys. Rev. Lett.* **72**, 993–996 (1994).

[62] S. Glasgow, P. Meystre, M. Wilkens, and E. M. Wright, "Theory of an atomic beam splitter based on velocity-tuned resonances", *Phys. Rev. A* **43**, 2455–2463 (1991).

[63] T. Pfau, C. Kurtsiefer, C. S. Adams, M. Sigel, and J. Mlynek, "Magneto-optical beam splitter for atoms", *Phys. Rev. Lett.* **71**, 3427–3430 (1993).

[64] O. Houde, D. Kadio, and L. Pruvost, "Cold atom beam splitter realized with two crossing dipole guides", *Phys. Rev. Lett.* **85**, 5543–5546 (2000).

[65] R. Grimm, J. Söding, and Y. B. Ovchinnikov, "Coherent beam splitter for atoms based on a bichromatic standing light wave", *Opt. Lett.* **19**, 658–660 (1994).

[66] C. K. Hong, Z. Y. Ou, and L. Mandel, "Measurement of subpicosecond time intervals between two photons by interference", *Phys. Rev. Lett.* **59**, 2044–2046 (1987).

[67] R. Lopes, A. Imanaliev, A. Aspect, M. Cheneau, D. Boiron, and C. I. Westbrook, "Atomic Hong-Ou-Mandel experiment", *Nature* **520**, 66–68 (2015).

[68] A. Buchleitner and A. R. Kolovsky, "Interaction-induced decoherence of atomic Bloch oscillations", *Phys. Rev. Lett.* **91**, 253002 (2003).

[69] J. T. Chalker, Y. Gefen, and M. Y. Veillette, "Decoherence and interactions in an electronic Mach-Zehnder interferometer", *Phys. Rev. B* **76**, 085320 (2007).

[70] A. O. Jamison, J. N. Kutz, and S. Gupta, "Atomic interactions in precision interferometry using Bose-Einstein condensates", *Phys. Rev. A* **84**, 043643 (2011).

[71] B. Juliá-Díaz, T. Zibold, M. K. Oberthaler, M. Melé-Messeguer, J. Martorell, and A. Polls, "Dynamic generation of spin-squeezed states in bosonic Josephson junctions", *Phys. Rev. A* **86**, 023615 (2012).

[72] M. Heyl, "Dynamical quantum phase transitions in systems with broken-symmetry phases", *Phys. Rev. Lett.* **113**, 205701 (2014).

[73] M. Heyl, "Scaling and universality at dynamical quantum phase transitions", *Phys. Rev. Lett.* **115**, 140602 (2015).

[74] P. Jurcevic, H. Shen, P. Hauke, C. Maier, T. Brydges, C. Hempel, B. P. Lanyon, M. Heyl, R. Blatt, and C. F. Roos, "Direct observation of dynamical quantum phase transitions in an interacting many-body system", *Phys. Rev. Lett.* **119**, 080501 (2017).

[75] M. Heyl and J. C. Budich, "Dynamical topological quantum phase transitions for mixed states", *Phys. Rev. B* **96**, 180304 (2017).

[76] S. Sharma, U. Divakaran, A. Polkovnikov, and A. Dutta, "Slow quenches in a quantum Ising chain: dynamical phase transitions and topology", *Phys. Rev. B* **93**, 144306 (2016).

[77] U. Bhattacharya, S. Bandyopadhyay, and A. Dutta, "Mixed state dynamical quantum phase transitions", *Phys. Rev. B* **96**, 180303 (2017).

[78] C. Karrasch and D. Schuricht, "Dynamical quantum phase transitions in the quantum Potts chain", *Phys. Rev. B* **95**, 075143 (2017).

[79] L. Piroli, B. Pozsgay, and E. Vernier, "Non-analytic behavior of the Loschmidt echo in XXZ spin chains: exact results", *Nucl. Phys. B* **933**, 454–481 (2018).

[80] M. E. Fisher, "Yang-Lee edge singularity and ϕ^3 field theory", *Phys. Rev. Lett.* **40**, 1610–1613 (1978).

[81] V. Giovannetti, S. Lloyd, and L. Maccone, "Quantum-enhanced measurements: beating the standard quantum limit", *Science* **306**, 1330–1336 (2004).

[82] D. Leibfried, M. D. Barrett, T. Schaetz, J. Britton, J. Chiaverini, W. M. Itano, J. D. Jost, C. Langer, and D. J. Wineland, "Toward Heisenberg-limited spectroscopy with multiparticle entangled states", *Science* **304**, 1476–1478 (2004).

[83] V. Giovannetti, S. Lloyd, and L. Maccone, "Quantum metrology", *Phys. Rev. Lett.* **96**, 010401 (2006).

[84] V. Giovannetti, S. Lloyd, and L. Maccone, "Advances in quantum metrology", *Nat. Photonics* **5**, 222–229 (2011).

[85] S. Will, T. Best, U. Schneider, L. Hackermüller, D.-S. Lühmann, and I. Bloch, "Time-resolved observation of coherent multi-body interactions in quantum phase revivals", *Nature* **465**, 197–201 (2010).

[86] G. J. Milburn, J. Corney, E. M. Wright, and D. F. Walls, "Quantum dynamics of an atomic Bose-Einstein condensate in a double-well potential", *Phys. Rev. A* **55**, 4318–4324 (1997).

[87] T.-L. Ho and C. V. Ciobanu, "The Schrödinger cat family in attractive Bose gases", *J. Low Temp. Phys.* **135**, 257–266 (2004).

[88] M. Albiez, R. Gati, J. Fölling, S. Hunsmann, M. Cristiani, and M. K. Oberthaler, "Direct observation of tunneling and nonlinear self-trapping in a single bosonic Josephson junction", *Phys. Rev. Lett.* **95**, 010402 (2005).

[89] A. N. Salgueiro, A. de Toledo Piza, G. B. Lemos, R. Drumond, M. C. Nemes, and M. Weidemüller, "Quantum dynamics of bosons in a double-well potential: Josephson oscillations, self-trapping and ultralong tunneling times", *Eur. Phys. J. D* **44**, 537–540 (2007).

[90] T. Zibold, E. Nicklas, C. Gross, and M. K. Oberthaler, "Classical bifurcation at the transition from Rabi to Josephson dynamics", *Phys. Rev. Lett.* **105**, 204101 (2010).

[91] Q.-L. Jie, S.-J. Wang, and L.-F. Wei, "Partial revivals of wave packets: an action-angle phase-space description", *Phys. Rev. A* **57**, 3262–3267 (1998).

[92] R. A. Bartels, T. C. Weinacht, N. Wagner, M. Baertschy, C. H. Greene, M. M. Murnane, and H. C. Kapteyn, "Phase modulation of ultrashort light pulses using molecular rotational wave packets", *Phys. Rev. Lett.* **88**, 013903 (2001).

[93] A. Micheli, D. Jaksch, J. I. Cirac, and P. Zoller, "Many-particle entanglement in two-component Bose-Einstein condensates", *Phys. Rev. A* **67**, 013607 (2003).

[94] C. A. Regal, private communication.

[95] J. Sebby-Strabley, M. Anderlini, P. S. Jessen, and J. V. Porto, "Lattice of double wells for manipulating pairs of cold atoms", *Phys. Rev. A* **73**, 033605 (2006).

[96] Y. Shin, M. Saba, T. A. Pasquini, W. Ketterle, D. E. Pritchard, and A. E. Leanhardt, "Atom interferometry with Bose-Einstein condensates in a double-well potential", *Phys. Rev. Lett.* **92**, 050405 (2004).

[97] T. Schumm, S. Hofferberth, L. M. Andersson, S. Wildermuth, S. Groth, I. Bar-Joseph, J. Schmiedmayer, and P. Krüger, "Matter-wave interferometry in a double well on an atom chip", *Nat. Phys.* **1**, 57–62 (2005).

[98] R. Islam, R. Ma, P. M. Preiss, M. Eric Tai, A. Lukin, M. Rispoli, and M. Greiner, "Measuring entanglement entropy in a quantum many-body system", *Nature* **528**, 77–83 (2015).

[99] C. Lyu, S. Choudhury, C. Lv, Y. Yan, and Q. Zhou, "Eternal discrete time crystal beating the Heisenberg limit", *Phys. Rev. Research* **2**, 033070 (2020).

[100] A. Lazarides, A. Das, and R. Moessner, "Equilibrium states of generic quantum systems subject to periodic driving", *Phys. Rev. E* **90**, 012110 (2014).

[101] L. D'Alessio and M. Rigol, "Long-time behavior of isolated periodically driven interacting lattice systems", *Phys. Rev. X* **4**, 041048 (2014).

[102] P. Ponte, A. Chandran, Z. Papić, and D. A. Abanin, "Periodically driven ergodic and many-body localized quantum systems", *Ann. Phys. (N. Y.)* **353**, 196–204 (2015).

[103] A. Pal and D. A. Huse, "Many-body localization phase transition", *Phys. Rev. B* **82**, 174411 (2010).

[104] C. W. von Keyserlingk, V. Khemani, and S. L. Sondhi, "Absolute stability and spatiotemporal long-range order in Floquet systems", *Phys. Rev. B* **94**, 085112 (2016).

[105] H. Lipkin, N. Meshkov, and A. Glick, "Validity of many-body approximation methods for a solvable model", *Nucl. Phys.* **62**, 188–198 (1965).

[106] C.-L. Hung, A. González-Tudela, J. I. Cirac, and H. J. Kimble, "Quantum spin dynamics with pairwise-tunable, long-range interactions", *Proc. Natl. Acad. Sci. U.S.A.* **113**, E4946–E4955 (2016).

[107] H. Ritsch, P. Domokos, F. Brennecke, and T. Esslinger, "Cold atoms in cavity-generated dynamical optical potentials", *Rev. Mod. Phys.* **85**, 553–601 (2013).

[108] B. Yan, S. A. Moses, B. Gadway, J. P. Covey, K. R. A. Hazzard, A. M. Rey, D. S. Jin, and J. Ye, "Observation of dipolar spin-exchange interactions with lattice-confined polar molecules", *Nature* **501**, 521–525 (2013).

[109] L. D'Alessio and A. Polkovnikov, "Many-body energy localization transition in periodically driven systems", *Ann. Phys. (N. Y.)* **333**, 19–33 (2013).

[110] F. Haake, M. Kuś, and R. Scharf, "Classical and quantum chaos for a kicked top", *Z. Phys. B* **65**, 381–395 (1987).

[111] D. Braun, G. Adesso, F. Benatti, R. Floreanini, U. Marzolino, M. W. Mitchell, and S. Pirandola, "Quantum-enhanced measurements without entanglement", *Rev. Mod. Phys.* **90**, 035006 (2018).

[112] G. E. Marti, R. B. Hutson, A. Goban, S. L. Campbell, N. Poli, and J. Ye, "Imaging optical frequencies with 100 μHz precision and 1.1 μm resolution", *Phys. Rev. Lett.* **120**, 103201 (2018).

[113] A. M. Rey, L. Jiang, and M. D. Lukin, "Quantum-limited measurements of atomic scattering properties", *Phys. Rev. A* **76**, 053617 (2007).

[114] S. Choi and B. Sundaram, "Bose-Einstein condensate as a nonlinear Ramsey interferometer operating beyond the Heisenberg limit", *Phys. Rev. A* **77**, 053613 (2008).

[115] M. Napolitano, M. Koschorreck, B. Dubost, N. Behbood, R. J. Sewell, and M. W. Mitchell, "Interaction-based quantum metrology showing scaling beyond the Heisenberg limit", *Nature* **471**, 486–489 (2011).

[116] D. Leibfried, E. Knill, S. Seidelin, J. Britton, R. B. Blakestad, J. Chiaverini, D. B. Hume, W. M. Itano, J. D. Jost, C. Langer, R. Ozeri, R. Reichle, and D. J. Wineland, "Creation of a six-atom 'Schrödinger cat' state", *Nature* **438**, 639–642 (2005).

[117] Z. Gong, R. Hamazaki, and M. Ueda, "Discrete time-crystalline order in cavity and circuit QED systems", *Phys. Rev. Lett.* **120**, 040404 (2018).

[118] C. Lyu, C. Lv, and Q. Zhou, "Geometrizing quantum dynamics of a Bose-Einstein condensate", *Phys. Rev. Lett.* **125**, 253401 (2020).

[119] J. Maldacena, "The large-N limit of superconformal field theories and supergravity", *Int. J. Theor. Phys.* **38**, 1113–1133 (1999).

[120] S. Sachdev, *From gravity to thermal gauge theories: the AdS/CFT correspondence* (Springer Berlin Heidelberg, 2011), pp. 273–311.

[121] S. Chapman, J. Eisert, L. Hackl, M. P. Heller, R. Jefferson, H. Marrochio, and R. C. Myers, "Complexity and entanglement for thermofield double states", *SciPost Phys.* **6** (2019).

[122] R. A. Jefferson and R. C. Myers, "Circuit complexity in quantum field theory", *J. High Energy Phys.* **10**, 107 (2017).

[123] J. Maldacena and L. Susskind, "Cool horizons for entangled black holes", *Fortschritte der Phys.* **61**, 781–811 (2013).

[124] J. Maldacena, "Eternal black holes in anti-de Sitter", *J. High Energy Phys.* **04**, 021–021 (2003).

[125] F. Pastawski, B. Yoshida, D. Harlow, and J. Preskill, "Holographic quantum error-correcting codes: toy models for the bulk/boundary correspondence", *J. High Energy Phys.* **06**, 149 (2015).

[126] M. Nozaki, S. Ryu, and T. Takayanagi, "Holographic geometry of entanglement renormalization in quantum field theories", *J. High Energy Phys.* **10**, 193 (2012).

[127] B. Swingle, "Entanglement renormalization and holography", *Phys. Rev. D* **86**, 065007 (2012).

[128] M. Miyaji, T. Numasawa, N. Shiba, T. Takayanagi, and K. Watanabe, "Continuous multiscale entanglement renormalization ansatz as holographic surface-state correspondence", *Phys. Rev. Lett.* **115**, 171602 (2015).

[129] E. A. Donley, N. R. Claussen, S. L. Cornish, J. L. Roberts, E. A. Cornell, and C. E. Wieman, "Dynamics of collapsing and exploding Bose-Einstein condensates", *Nature* **412**, 295–299 (2001).

[130] B. Wu and Q. Niu, "Landau and dynamical instabilities of the superflow of Bose-Einstein condensates in optical lattices", *Phys. Rev. A* **64**, 061603 (2001).

[131] J. H. V. Nguyen, D. Luo, and R. G. Hulet, "Formation of matter-wave soliton trains by modulational instability", *Science* **356**, 422–426 (2017).

[132] J. Hu, L. Feng, Z. Zhang, and C. Chin, "Quantum simulation of Unruh radiation", *Nat. Phys.* **15**, 785–789 (2019).

[133] C. C. Bradley, C. A. Sackett, J. J. Tollett, and R. G. Hulet, "Evidence of Bose-Einstein condensation in an atomic gas with attractive interactions", *Phys. Rev. Lett.* **75**, 1687–1690 (1995).

[134] J. Mun, P. Medley, G. K. Campbell, L. G. Marcassa, D. E. Pritchard, and W. Ketterle, "Phase diagram for a Bose-Einstein condensate moving in an optical lattice", *Phys. Rev. Lett.* **99**, 150604 (2007).

[135] K. Wintersperger, M. Bukov, J. Näger, S. Lellouch, E. Demler, U. Schneider, I. Bloch, N. Goldman, and M. Aidelsburger, "Parametric instabilities of interacting bosons in periodically driven 1D optical lattices", *Phys. Rev. X* **10**, 011030 (2020).

[136] T. Boulier, J. Maslek, M. Bukov, C. Bracamontes, E. Magnan, S. Lellouch, E. Demler, N. Goldman, and J. V. Porto, "Parametric heating in a 2D periodically driven bosonic system: beyond the weakly interacting regime", *Phys. Rev. X* **9**, 011047 (2019).

[137] C. V. Parker, L.-C. Ha, and C. Chin, "Direct observation of effective ferromagnetic domains of cold atoms in a shaken optical lattice", *Nat. Phys.* **9**, 769–774 (2013).

[138] J. M. Gerton, D. Strekalov, I. Prodan, and R. G. Hulet, "Direct observation of growth and collapse of a Bose-Einstein condensate with attractive interactions", *Nature* **408**, 692–695 (2000).

[139] C.-A. Chen and C.-L. Hung, "Observation of universal quench dynamics and Townes soliton formation from modulational instability in two-dimensional Bose gases", *Phys. Rev. Lett.* **125**, 250401 (2020).

[140] M. Novaes, "Some basics of $\mathfrak{su}(1,1)$", *Rev. Bras. Ensino Fís.* **26**, 351–357 (2004).

[141] R. Gilmore, *Lie groups, physics, and geometry: an introduction for physicists, engineers and chemists* (Cambridge University Press, 2008).

[142] Y. Cheng and Z.-Y. Shi, "Many-body dynamics with time-dependent interaction", *arXiv:2004.12754 [cond-mat.quant-gas]* (2020).

[143] S. W. Hawking, "Black hole explosions?", *Nature* **248**, 30–31 (1974).

[144] W. G. Unruh, "Notes on black-hole evaporation", *Phys. Rev. D* **14**, 870–892 (1976).

[145] Y.-Y. Chen, P. Zhang, W. Zheng, Z. Wu, and H. Zhai, "Many-body echo", *Phys. Rev. A* **102**, 011301 (2020).

[146] V. Galitski and I. B. Spielman, "Spin–orbit coupling in quantum gases", *Nature* **494**, 49–54 (2013).

[147] C.-H. Li, C. Qu, R. J. Niffenegger, S.-J. Wang, M. He, D. B. Blasing, A. J. Olson, C. H. Greene, Y. Lyanda-Geller, Q. Zhou, C. Zhang, and Y. P. Chen, "Spin current generation and relaxation in a quenched spin-orbit-coupled Bose-Einstein condensate", *Nat. Commun.* **10** (2019).

[148] C. K. Law, H. Pu, and N. P. Bigelow, "Quantum spins mixing in spinor Bose-Einstein condensates", *Phys. Rev. Lett.* **81**, 5257–5261 (1998).

[149] X.-Y. Luo, Y.-Q. Zou, L.-N. Wu, Q. Liu, M.-F. Han, M. K. Tey, and L. You, "Deterministic entanglement generation from driving through quantum phase transitions", *Science* **355**, 620–623 (2017).

[150] M. O. Scully and M. S. Zubairy, *Quantum optics* (Cambridge University Press, 1997).

[151] R. Yamazaki, S. Taie, S. Sugawa, and Y. Takahashi, "Submicron spatial modulation of an interatomic interaction in a Bose-Einstein condensate", *Phys. Rev. Lett.* **105**, 050405 (2010).

[152] T. L. Nicholson, S. Blatt, B. J. Bloom, J. R. Williams, J. W. Thomsen, J. Ye, and P. S. Julienne, "Optical Feshbach resonances: field-dressed theory and comparison with experiments", *Phys. Rev. A* **92**, 022709 (2015).

[153] Y. Castin and F. Werner, "The unitary gas and its symmetry properties", in *The BCS-BEC crossover and the unitary Fermi gas* (Springer Berlin Heidelberg, Berlin, Heidelberg, 2012), pp. 127–191.

[154] L. P. Pitaevskii and A. Rosch, "Breathing modes and hidden symmetry of trapped atoms in two dimensions", *Phys. Rev. A* **55**, R853–R856 (1997).

[155] R. Saint-Jalm, P. C. M. Castilho, É. Le Cerf, B. Bakkali-Hassani, J.-L. Ville, S. Nascimbene, J. Beugnon, and J. Dalibard, "Dynamical symmetry and breathers in a two-dimensional Bose gas", *Phys. Rev. X* **9**, 021035 (2019).

[156] S. Schmid, A. Härter, and J. H. Denschlag, "Dynamics of a cold trapped ion in a Bose-Einstein condensate", *Phys. Rev. Lett.* **105**, 133202 (2010).

[157] L. Ratschbacher, C. Sias, L. Carcagni, J. M. Silver, C. Zipkes, and M. Köhl, "Decoherence of a single-ion qubit immersed in a spin-polarized atomic bath", *Phys. Rev. Lett.* **110**, 160402 (2013).

[158] T. Fukuhara, A. Kantian, M. Endres, M. Cheneau, P. Schauß, S. Hild, D. Bellem, U. Schollwöck, T. Giamarchi, C. Gross, I. Bloch, and S. Kuhr, "Quantum dynamics of a mobile spin impurity", *Nat. Phys.* **9**, 235–241 (2013).

[159] F. Schmidt, D. Mayer, Q. Bouton, D. Adam, T. Lausch, N. Spethmann, and A. Widera, "Quantum spin dynamics of individual neutral impurities coupled to a Bose-Einstein Condensate", *Phys. Rev. Lett.* **121**, 130403 (2018).

[160] M. Mehboudi, A. Lampo, C. Charalambous, L. A. Correa, M. Á. García-March, and M. Lewenstein, "Using polarons for sub-nK quantum nondemolition thermometry in a Bose-Einstein condensate", *Phys. Rev. Lett.* **122**, 030403 (2019).

[161] F. M. Spiegelhalder, A. Trenkwalder, D. Naik, G. Hendl, F. Schreck, and R. Grimm, "Collisional stability of ^{40}K immersed in a strongly interacting Fermi gas of ^{6}Li", *Phys. Rev. Lett.* **103**, 223203 (2009).

[162] M. Koschorreck, D. Pertot, E. Vogt, B. Fröhlich, M. Feld, and M. Köhl, "Attractive and repulsive Fermi polarons in two dimensions", *Nature* **485**, 619–622 (2012).

[163] P. Massignan, M. Zaccanti, and G. M. Bruun, "Polarons, dressed molecules and itinerant ferromagnetism in ultracold Fermi gases", *Rep. Prog. Phys.* **77**, 034401 (2014).

[164] M. Cetina, M. Jag, R. S. Lous, I. Fritsche, J. T. M. Walraven, R. Grimm, J. Levinsen, M. M. Parish, R. Schmidt, M. Knap, and E. Demler, "Ultrafast many-body interferometry of impurities coupled to a Fermi sea", *Science* **354**, 96–99 (2016).

[165] M. Streif, A. Buchleitner, D. Jaksch, and J. Mur-Petit, "Measuring correlations of cold-atom systems using multiple quantum probes", *Phys. Rev. A* **94**, 053634 (2016).

[166] T. J. Elliott and T. H. Johnson, "Nondestructive probing of means, variances, and correlations of ultracold-atomic-system densities via qubit impurities", *Phys. Rev. A* **93**, 043612 (2016).

[167] D. Hangleiter, M. T. Mitchison, T. H. Johnson, M. Bruderer, M. B. Plenio, and D. Jaksch, "Nondestructive selective probing of phononic excitations in a cold Bose gas using impurities", *Phys. Rev. A* **91**, 013611 (2015).

[168] A. Klein and M. Fleischhauer, "Interaction of impurity atoms in Bose-Einstein condensates", *Phys. Rev. A* **71**, 033605 (2005).

[169] K. Keiler and P. Schmelcher, "State engineering of impurities in a lattice by coupling to a Bose gas", *New J. Phys.* **20**, 103042 (2018).

[170] A. J. Daley, P. O. Fedichev, and P. Zoller, "Single-atom cooling by superfluid immersion: a nondestructive method for qubits", *Phys. Rev. A* **69**, 022306 (2004).

[171] T.-L. Ho and S. K. Yip, "Fragmented and single condensate ground states of spin-1 Bose gas", *Phys. Rev. Lett.* **84**, 4031–4034 (2000).

[172] R. B. Diener and T.-L. Ho, "Quantum spin dynamics of spin-1 Bose gas", *arXiv:cond-mat/0608732* (2016).

VITA

Education

- Aug. 2016 - May 2021, Doctor of Philosophy, Physics
  Department of Physics and Astronomy, Purdue University
  West Lafayette, Indiana, USA
  Advisor: Professor Qi Zhou

- Sept. 2012 - June 2016, Bachelor of Science, Physics
  Kuang Yaming Honors School, Nanjing University
  Nanjing, Jiangsu, China

Awards

- Travel Grant, Department of Physics and Astronomy, Purdue University, Apr. 2019.
- Frederick N. Andrews Fellowship, Graduate School of Purdue University, Aug. 2016.
- Meritorious Winner of Mathematical Contest in Modeling, Consortium for Mathematics and Its Applications, Apr. 2014.
- People's Scholarship, Nanjing University, Nov. 2013.

Publications

- *Geometrizing quantum dynamics of a Bose-Einstein condensate*
  Changyuan Lyu[†], Chenwei Lv[†], and Qi Zhou, Phys. Rev. Lett. **125**, 253401 (2020).
  (†equal contributions)

- *Eternal discrete time crystal beating the Heisenberg limit*
  Changyuan Lyu, Sayan Choudhury, Chenwei Lv, Yangqian Yan, and Qi Zhou, Phys. Rev. Research **2**, 033070 (2020).

- *Dynamical quantum phase transitions in interacting atomic interferometers*
  Changyuan Lyu and Qi Zhou, Phys. Rev. A **101**, 043605 (2020).

- *Localization in quantum walks on a honeycomb network*
  Changyuan Lyu, Luyan Yu, and Shengjun Wu, Phys. Rev. A **92**, 052305 (2015).